INAUGURAL-DISSERTATION

zur
Erlangung der Doktorwürde
der
Naturwissenschaftlich-Mathematischen
Gesamtfakultät
der
Ruprecht-Karls-Universität
Heidelberg

vorgelegt von
Dipl.-Phys. Wolfgang G. Kirsch
aus Hanau

Tag der mündlichen Prüfung: 27.10.2000

Biophysikalische Analyse der räumlichen und zeitlichen Verteilung freier Ca^{2+}-ionen in Mikro- und Nanodomänen von Muskelzellen

Gutachter: Prof. Dr. Rainer H.A. Fink

Prof. Dr. Josef F. Bille

Dissertation
submitted to the
Combined Faculties for the Natural Sciences and for Mathematics
of the Rupertus Carola University of
Heidelberg, Germany
for the degree of
Doctor of Natural Sciences

Biophysical analysis of the spatial and temporal distribution of free Ca^{2+} ions within micro- and nanodomains of muscle cells

presented by

Diplom-Physicist:	Wolfgang G. Kirsch
born in:	Hanau

Heidelberg, 27.10.2000

Referees:	Prof. Dr. Rainer H.A. Fink
	Prof. Dr. Josef F. Bille

Biophysikalische Analyse der räumlichen und zeitlichen Verteilung freier Ca^{2+}-ionen in Mikro- und Nanodomänen von Muskelzellen

Im Verlauf dieser Doktorarbeit wurden Methoden zur Messung und Quantifizierung der räumlichen und zeitlichen Änderungen der freien Ca^{2+}-Ionenkonzentration ($[Ca^{2+}]$) innerhalb von Skelettmuskelzellen entwickelt und die damit verbundene Rate der aus dem sarkoplasmatischen Retikulum (SR) freigesetzten Ca^{2+}-Ionen berechnet, die auf der Öffnung von in der SR-Membran lokalisierten Ionenkanälen (RyR) beruht. Die Messung von Ca^{2+}-Signalen innerhalb von Mikrodomänen einer Muskelzelle (Durchschnittliche transiente Erhöhungen von $[Ca^{2+}]$ innerhalb der gesamten Zelle) erfolgte mittels Epi-Illuminations-Mikroskopie durch Ausnutzung von Absorptionsänderungen des Ca^{2+}-Indikators Antipyrylazo III. Ca^{2+}-Signale innerhalb von Nanodomänen einer Muskelzelle (sehr kurze und hochlokalisierte Änderungen von $[Ca^{2+}]$ induziert durch elementare Ca^{2+}-Freisetzungsereignisse) wurden mit Sub-Mikrometer-Präzision und einer zeitlichen Auflösung von 2 ms mittels konfokaler Laser- Scanning-Fluoreszenz-Mikroskopie gemessen. Die Ca^{2+}-Freisetzungsrate aus dem SR wurde berechnet, indem die derzeit bekannten Informationen über Reaktions- und Diffusionseigenschaften von Ca^{2+}-Puffern und Ca^{2+}-Pumpen in Muskelzellen zu Grunde gelegt wurden. Die Anwendung dieser quantitativen Methoden führte zu der Schlussfolgerung, dass elementare Ca^{2+}-Freisetzungs-ereignisse durch die Öffnung von mehr als einem RyR ausgelöst werden. Bedeutende morphologische Unterschiede zwischen elementaren Ca^{2+}-Freisetzungsereignissen unter unterschiedlichen Versuchsbedingungen wurden aufgedeckt, die sich durch die molekulare Zusammensetzung der Triade erklären lassen. Mit dieser Arbeit gelang zum ersten Mal die Messung von häufigen elementaren Ca^{2+}-Freisetzungsereignissen innerhalb einer Muskelzelle von adulten Säugetieren, was von zentraler Bedeutung für Muskelkrankheiten mit pathophysiologischen Änderungen der Ca^{2+}-Regulation ist.

Biophysical analysis of the spatial and temporal distribution of free Ca^{2+} ions within micro- and nanodomains of muscle cells

This work establishes methods to measure and quantify the spatial and temporal changes of the free Ca^{2+} ion concentration ($[Ca^{2+}]$) inside skeletal muscle fibers and to calculate the underlying Ca^{2+} release from the sarcoplasmic reticulum (SR) caused by the opening of Ca^{2+} permeable ion channels (RyRs). The recording of microdomain Ca^{2+} signals (spatially averaged measurements of transient increases in myoplasmic $[Ca^{2+}]$), was achieved by epi-illumination microscopy utilizing changes in the absorption of the Ca^{2+} indicator Antipyrylazo III. Nanodomain Ca^{2+} signals, the brief and highly localized spatio-temporal changes in $[Ca^{2+}]$ caused by elementary Ca^{2+} release events, were measured with submicron precision and a time resolution of 2 ms using confocal laser scanning fluorescence microscopy. The underlying release rate of Ca^{2+} ions from the SR was calculated using the most detailed information about intracellular Ca^{2+} buffers and Ca^{2+} pumps currently available. With these quantitative tools this work lead to the conclusion that the elementary events of Ca^{2+} release are generated by the opening of more than one RyR. Striking morphological differences between elementary Ca^{2+} release events measured under different experimental conditions are revealed, which can be explained by the molecular structure of the Ca^{2+} release source. For the first time this work presents measurements of Ca^{2+} sparks in adult mammalian muscle with high abundance which is of significant importance for medical diseases involving pathophysiological changes in Ca^{2+} regulation.

Abbreviations

ApIII	Antipyrylazo III
AOM	acusto-optical mirror
ATP	adenosine-triphosphate
$[Ca^{2+}]$	free Ca^{2+} ion concentration
CICR	calcium induced calcium release
CP	creatine phosphate
DHPR	dihydropyridine receptor
DIC	differential interference contrast
ec-coupling	excitation-contraction coupling
EDL	extensor digitorum longus (muscle)
EGTA	ethylene glycol-bis(β-aminoethyl ether)-N,N,N´,N´-tetraacetic acid
ER	endoplasmic reticulum
FDHM	full duration at half maximum
FFT	fast Fourier transform
FWHM	full width at half maximum
HEPES	N-[2-hydroxyethyl]piperazine-N´-[2-ethanesulfonic acid]
IA	instrumentational amplifier
IDL	Interactive Data Language (software)
IF	interference filter
IS	ionic strength
$[Mg^{2+}]$	free Mg^{2+} ion concentration
NA	numerical aperture
ND	neutral density filter
NMR	nuclear magnetic resonance
PM	photomultiplier
PSF	point spread function
RISC	repolarization induced stop of caffeine induced release
RyR	ryanodine receptor
s.l.	sarcomere length
SR	sarcoplasmic reticulum
TA	transmembrane assembly
TPLSM	two photon excitation laser scanning microscopy
TEA	tetraethylammonium
TTS	transverse tubular system
TTX	tetrodotoxin

1 Introduction

One of the most important ways through which living organisms interact with the environment is movement. Movement within all cell types is based on three major classes of molecular motor proteins: myosin, kinesin and dynein. Their ability to undergo a defined conformational change in their protein structure is dependent on the hydrolysis of ATP. This energy consuming process can be transformed into movement along an attached actin filament, which is usually fixed to the cytoskeleton of the cell, therefore enabling a translation within the entire cell matrix.

In muscle tissue the most abundant motor protein is myosin, which together with actin is compressed into a filament structure that constrains the combined action of these filaments to initiate cell contraction or force production to a defined direction.

It is vital for any cell to have a regulatory mechanism for the motor proteins, allowing movement only when necessary. In muscle the interaction of myosin and actin is controlled by the intracellular calcium concentration.

Ca^{2+} ions are important messengers in all cells as changes in the intracellular Ca^{2+} concentration are involved in the regulation of numerous processes, for instance also in the release of neurotransmitters, cell division or cell death. In resting cells the intracellular free Ca^{2+} concentration is kept in the range of 10^{-7}-10^{-8} M. This free concentration is achieved by proteins that pump all Ca^{2+} ions out of the cell or into the internal Ca^{2+} stores, like the endoplasmic reticulum (ER). Ca^{2+} signals then arise through the opening of Ca^{2+} selective ion channels that temporarily connect the cytoplasm with the extracellular medium or with an internal Ca^{2+} store, which can contain a free Ca^{2+} concentration as much as four orders of magnitude higher than the cytoplasm, resulting in an influx of Ca^{2+} ions driven by the concentration gradient. The time frame of these transient elevations of intracellular calcium depends on the purpose of the signal and the cell type and ranges from milliseconds to hours.

In general, it is not only the duration of Ca^{2+} signals that is important in triggering the desired response, but also the spatial relationship between the source and target binding site of Ca^{2+} ions. The Ca^{2+} ions delivered by any Ca^{2+} source inside a cell will readily diffuse in all possible directions. Therefore, to create a local concentration near the acceptor that suits its Ca^{2+} affinity, the amount of Ca^{2+} ions needed from a source increases extensively with the distance between source and acceptor. Signal transmission is made even more difficult by Ca^{2+} buffers that are present in every cell.

Within the last ten years the use of x-ray diffraction has enabled scientists to determine the 3-dimensional structure of actin [Holmes et al., 1990] and myosin [Rayment et al., 1993]. Furthermore, with cryo-electron microscopy it was possible to resolve the structure of the ryanodine receptor (RyR), one of the largest ion-channels known in biology [Radermacher et al., 1994]. Being exclusively located in the membrane of internal organelles, the RyR is one of the Ca^{2+} selective channels through which Ca^{2+} ions are released from internal Ca^{2+} stores. Interestingly, the RyR can be opened by binding of Ca^{2+} ions to an activation site on the RyR. Hence it is possible that the release from a RyR can trigger the opening of a neighboring RyR. This mechanism is called calcium induced calcium release (CICR).

For the measurement of the release of Ca^{2+} ions new fluorescence indicators with high sensitivity for Ca^{2+} ions have been synthesized within the past decade. Their application in conjunction with more advanced microscopy and imaging techniques allows nowadays a non-invasive study of the structure-function relationship of Ca^{2+} signals on a more molecular basis.

The content of this thesis focuses on the Ca^{2+} release from internal stores in skeletal muscle. In these cells it is well known from experiments utilizing epi-fluorescence microscopy that the activation of the motor proteins is triggered by Ca^{2+} ions released through RyRs from the sarcoplasmic reticulum (SR), a specialized form of ER and the main store of Ca^{2+} ions. A standard release of Ca^{2+} ions causes a 10 to 100 fold transient increase in the free Ca^{2+} concentration across the whole cylindrical cell. It has been shown that whole cell Ca^{2+} release can be measured in physiological preparations with diffusional access to the interior of the muscle fiber. This was achieved using voltage-clamped cut muscle fibers of amphibians [Pizarro et al., 1997] and mammalians [Shirokova et al., 1996b], where only the ends of the muscle fibers are permeabilized, leaving the center fiber segment intact and allowing voltage control. The total Ca^{2+} turnover has also been quantified in chemically skinned mammalian muscle fibers [Uttenweiler et al., 1998], where the whole external membrane is permeabilized, but the SR is still intact. Measurements of Ca^{2+} release with whole cell methods average Ca^{2+} signals over several micrometers and these signals will further on be referred to as microdomain Ca^{2+} release.

Recently, pulsed laser excitation in combination with confocal spot detection revealed steep gradients of Ca^{2+} ions during Ca^{2+} release within skeletal muscle fibers and showed that the primary release sites are located at the terminal cisternae of the SR [Escobar et al., 1994]. Furthermore, laser confocal scanning microscopy has allowed to measure spatially and temporarily discrete Ca^{2+} signals, termed Ca^{2+} sparks, the elementary Ca^{2+} release events of excitation contraction coupling [Tsugorka et al., 1995; Klein et al., 1996].

Since their detection scientists have speculated whether Ca^{2+} sparks are produced by the opening of a single RyR [Klein et al., 1997; Lacampagne et al., 1999] or by channel cluster activation through CICR [Stern et al. 1997]. Another interesting fact is that local Ca^{2+} release in adult amphibians contains high numbers of Ca^{2+} sparks, but that no Ca^{2+} spark could be found in adult mammalian preparations thus far [Shirokova et al., 1997]. Because the size of

Ca^{2+} sources ranges between about 10 to 200 nanometers and the resolution of the experimental techniques is below 1 µm, the local Ca^{2+} signals measured with confocal microscopy are referred to as nanodomain Ca^{2+} release.

This work derives a technique to measure both, changes in the intracellular Ca^{2+} concentration and the absolute free Mg^{2+} concentration, in the microdomains of voltage-clamped cut skeletal muscle fibers by the Ca^{2+}/ Mg^{2+} chelator Antipyrylazo III with epi-illumination absorption. It establishes fluorescence imaging of nanodomain Ca^{2+} release containing Ca^{2+} sparks, using confocal laser scanning microscopy in voltage-clamped cut fibers and chemically skinned fibers loaded with Fluo-3 or Fluo-4. It provides a quantitative analysis of micro- and nanodomain Ca^{2+} release based on the laws of mass action and diffusion, taking into account Ca^{2+} buffers present in the muscle fiber. With these tools it specifically addresses the single channel hypothesis and thus the possible role of CICR in the underlying Ca^{2+} signals of nanodomain Ca^{2+} release by introducing two conditions that interfere with Ca^{2+} activation of RyRs: firstly, a high intracellular free Mg^{2+} ion concentration as an antagonistic and secondly, a low dose of caffeine as an agonistic condition for CICR. In addition, for the first time elementary events of Ca^{2+} release could be measured in abundance in mammalian muscle using chemically skinned fiber preparations.

2 Biophysics of Ca^{2+} release

2.1 Ca^{2+} regulation in skeletal muscle

A skeletal muscle fiber contains several myofibrils that have a cylindrical shape with a diameter of about 1 µm. The Z-disks divide the whole fiber and the myofibrils into sarcomeres of 2-4 µm length along the fiber axis and every sarcomere exhibits the same molecular layout. Connected to the Z-disk are the actin filaments (5 nm diameter), which from both sides span into the sarcomere center. The myosin filaments (10 nm diameter) are arranged parallely in between the actin filaments. A skeletal myosin molecule is made up of a long tail and two heads on one side (see Fig. 2.1). The myosin filament contains some hundred single myosin molecules, formed by attaching the tails so that the heads are located at the ends of the filament, while its center is just an overlap of tail regions. Shortening of the muscle cell is achieved by the sliding of the filaments against each other. This is accomplished by the attachment of myosin heads to the actin filament, the formation of the ´cross-bridges´. The myosin heads then change their conformation under hydrolysis of ATP while being attached, therefore displacing the filaments relative to each other. The so-called cross-bridge cycle of attached and non-attached states is then cyclically repeated.

Myosin can only bind to actin when the to actin attached troponin-tropomyosin complex has undergone a structural shift. This structural shift is induced by a series of protein-protein interactions upon binding of Ca^{2+} ions to troponin-C. Hence, the activation of the motor proteins is regulated by the intracellular free Ca^{2+} concentration.

Ca^{2+} ions are stored in the sarcoplasmic reticulum (SR), a cell compartment surrounding every myofibril. The SR contains ryanodine receptors (RyRs), ion-channels that are permeable for Ca^{2+} ions. The highest density of RyR is at the terminal cisternaes, the primary sites for Ca^{2+} release from the SR [Escobar et al., 1994]. Here the SR is in close proximity (below 20 nm) to the transverse tubular system (TTS), a network of membrane tubes that extend the external membrane into the cell body. Structurally defined protein assemblies exist within the TTS and SR membrane at these triadic junctions (see next paragraph). They enable the transmission of changes in electrical potential across the TTS membrane into the opening and closing of RyRs in the SR membrane.

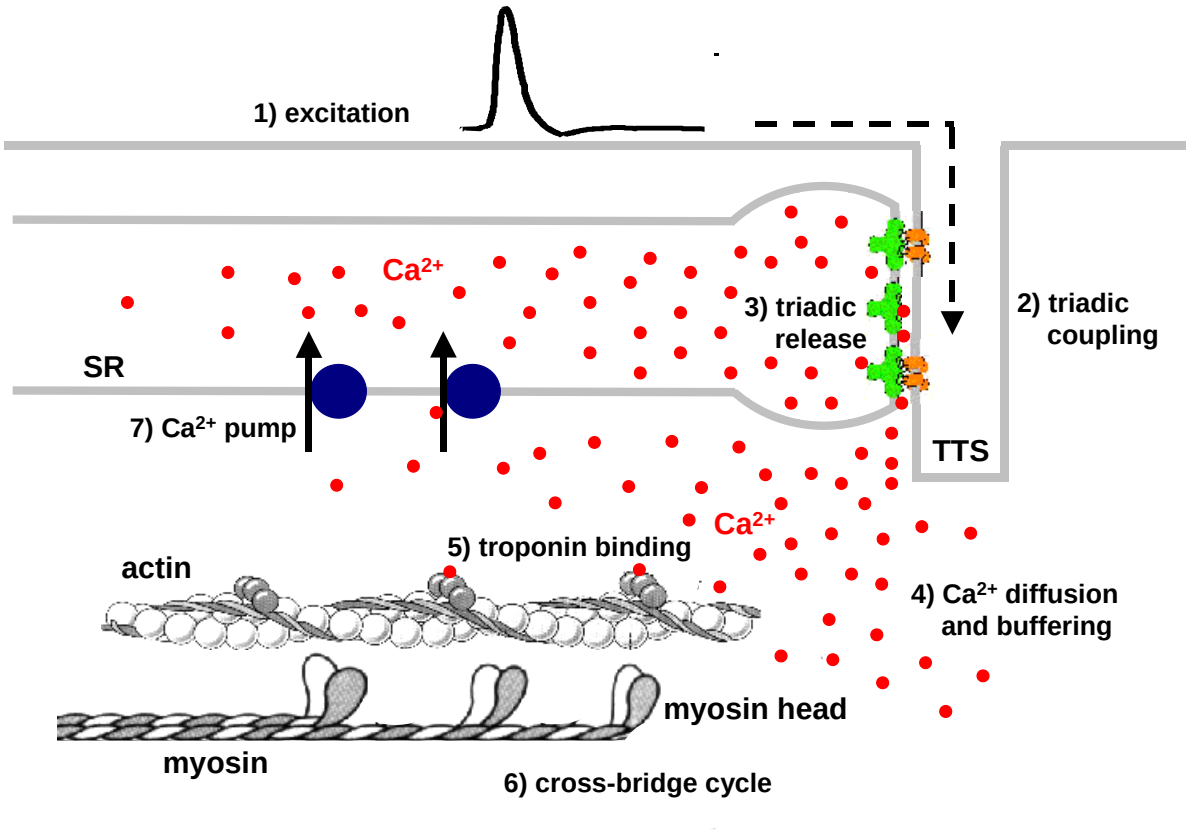

Fig. 2.1 Schematic drawing of the role of Ca^{2+} ions in muscle function. Action potentials trigger Ca^{2+} release from the SR. Ca^{2+} ions bind to buffers and are pumped back into the SR. Binding of Ca^{2+} ions to troponin activates the motor proteins, actin and myosin, leading to cross-bridge cycles. Modified from Uttenweiler D. [1997] and Deetjen et al. [1994].

The function of the skeletal muscle cell and the role of Ca^{2+} ions can thus be summarized as shown in Fig. 2.1. An excitation of the muscle fiber by an action potential [Hodgkin et al., 1952a-d] spreads along the external membrane and into the TTS. At triadic junctions the depolarization is translated into the opening of RyRs, thereby triggering release of Ca^{2+} ions from the SR into the junctional cleft. Then Ca^{2+} ions diffuse into the myoplasm and will simultaneously bind to any present Ca^{2+} buffers inside the muscle fiber. Ca^{2+} ions will also bind to troponin-C and thus activate the motor proteins to consecutively perform cross-bridge cycles. Meanwhile Ca^{2+} pumps located in the SR will translocate Ca^{2+} ions back into the SR. Force production and movement will continue until the Ca^{2+} concentration can be lowered below activation levels by pumps and intracellular Ca^{2+} buffers. Normally this is achieved about 500 ms after the repolarization of the fiber, because this results in the closing of RyRs. Continued force activation is generated by trains of action potentials, although it cannot be sustained for too long, as it causes muscle fatigue.

2.2 Molecular basis of Ca^{2+} release

2.2.1 Ryanodine receptors

The ion channels through which Ca^{2+} ions are released from the SR are known as ryanodine receptors (RyRs) because they can bind the plant alkaloid ryanodine with high affinity and specificity [Meissner G., 1994]. Three isoforms of RyRs exist, where RyR1 [Takeshima et al., 1989] and RyR3 [Giannini et al., 1992] are abundant in skeletal muscle and RyR2 [Nakai et al., 1990] is most frequent in cardiac muscle. RyR1 and RyR2 have been purified as 30S protein complexes composed of four large (~560 kDa) [Coronado et al., 1994] and four small subunits (FK-506-binding protein, ~12 kDa) [Timerman et al., 1996]. Three-dimensional reconstructions, obtained by cryo-electron microscopy reveal

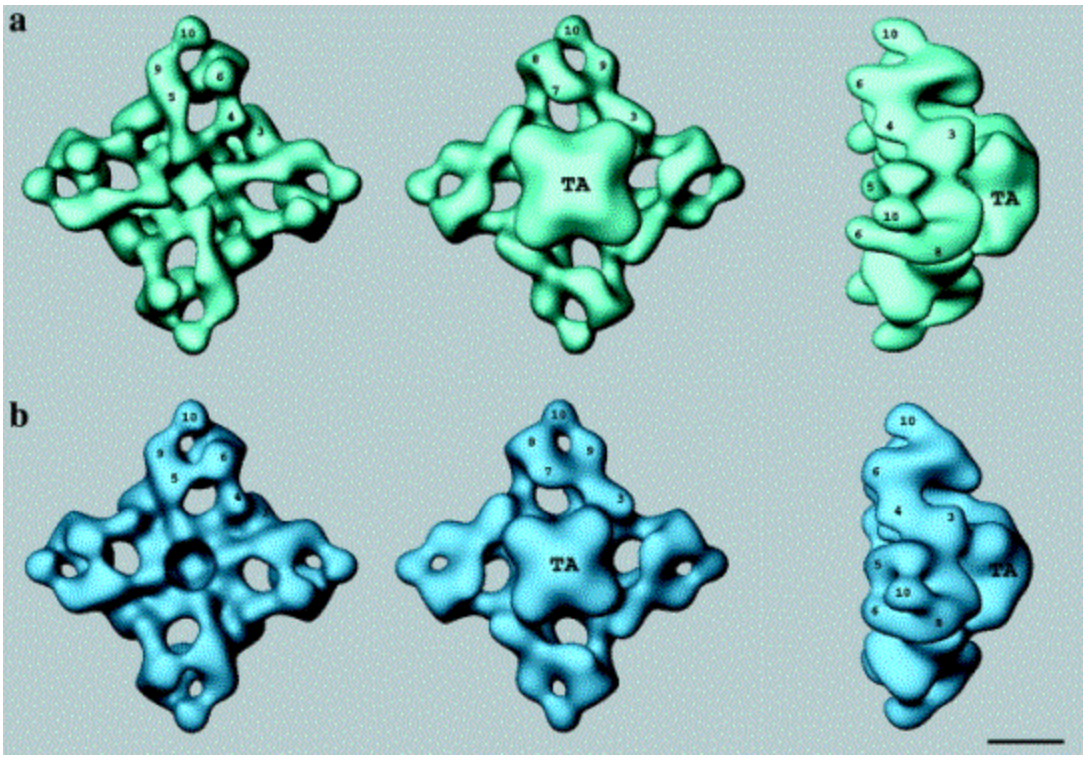

Fig. 2.2 3D-representation of the ryanodine receptor type 3 (RyR3) in the closed (green) and the open state (blue). The three different views show the surface that faces the TTS (left), the surface that faces the SR (middle) and a side view showing the interaction of the transmembrane assembly (TA) with the cytoplasmic assembly (right). Scale bar: 10 nm. From Sharma et al. [2000].

that around 80% of the protein mass forms a cytoplasmic assembly (see Fig. 2.2), that can also be seen as foot-structure in fiber slice preparations, spanning the gap between TTS and SR membrane (Franzini-Armstrong et al., 1998). Structural differences exist between the open and the closed state of RyRs, an example is given for RyR3 in Fig. 2.2. The most

apparent change occurs in the transmembrane assembly, which, in the open state, appears to be larger and to rotated by ~4° relative to its position in the closed state [Sharma et al., 2000].

Physiological and biochemical evidence suggests that RyRs are ligand-gated channels with Ca^{2+} as a major regulator. In [^{3}H]ryanodine binding assays, where 1 out of 1000 ryanodine molecules is radioactively labeled, the dissociation constants for Ca^{2+} activation or inactivation reactions can be measured in a strictly controlled ionic environment, as ryanodine only binds to the open state of the channel (see Fig. 2.3). In such experiments the activation by micromolar and inhibition by millimolar Ca^{2+} concentrations suggest at least two classes of Ca^{2+} binding sites: high-affinity activation and low-affinity inactivation sites [Liu et al., 1997].

Various other endogenous and exogenous effectors have been identified, including Mg^{2+}, ATP and caffeine. Mg^{2+} ions bind competitively to both activation and inactivation sites with dissociation constants in the millimolar range, but they never induce an opening of the RyR. The free Mg^{2+} concentration of 0.5-1 mM inside the cytoplasm has an important inhibitory effect, as cells would otherwise continuously exhibit spontaneous Ca^{2+} release. In addition, if the ATP concentration falls below 100 μM, it can decreases the open probability of RyRs [Xu et al., 1996]. Caffeine increases the affinity of the Ca^{2+} activation site of RyRs, for instance a high dose of caffeine can trigger a strong release from the SR in permeabilized muscle fibers [Uttenweiler et al., 1998].

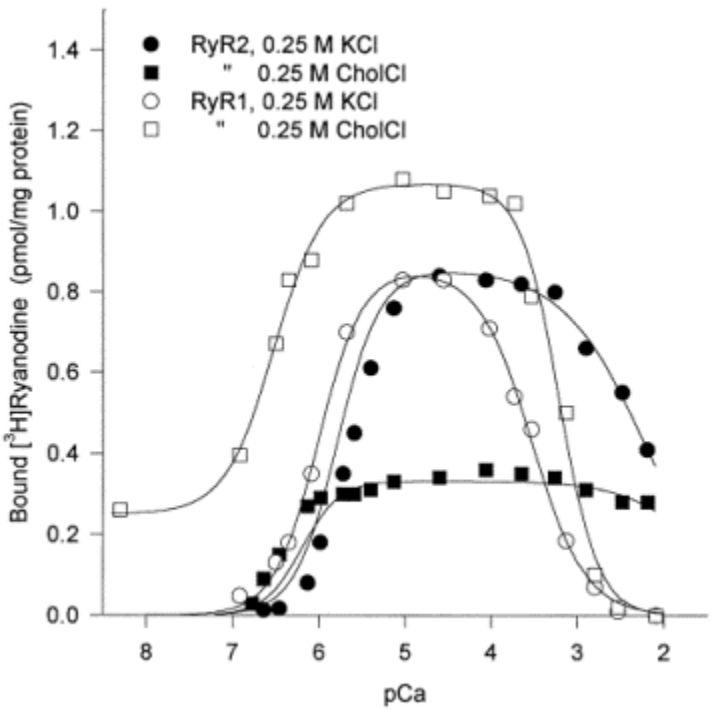

Fig. 2.3 Ca^{2+} dependence of [^{3}H]ryanodine binding to skeletal (RyR1) and cardiac (RyR2) muscle ryanodine receptors in KCl and choline chloride (CholCl) media. Activation by micromolar and inhibition by millimolar Ca^{2+} concentrations suggest at least two classes of Ca^{2+} binding sites, high-affinity activation sites and low-affinity inactivation sites. From Liu et al. [1997].

2.2.2 Dihydropyridine receptors

The dihydropyridine receptors (DHPRs) are voltage-gated L-type Ca^{2+} channels. There exist three isoforms of the L-type channel. The skeletal DHPR [Tanabe et al., 1987] is only abundant in skeletal muscle and mainly located in the membrane of the TTS [Almers et al., 1980]. The cardiac DHPR [Mikami et al., 1989] is mainly expressed in heart and brain. The third isoform, class D [Williams et al., 1992], can be found in neural and endocrine tissues.

The skeletal and cardiac DHPR are important in excitation-contraction coupling (ec-coupling) of muscle. In heart muscle the influx of Ca^{2+} ions through the cardiac DHPRs triggers additional Ca^{2+} release from the SR. The opening of the RyR2s is thus triggered by Ca^{2+} ions only and this process is referred to as calcium induced calcium release (CICR) [Endo M., 1977]. However, in skeletal muscle direct protein-protein interactions between RyR1 and skeletal DHPR, which do not require entry of extracellular Ca^{2+} ions, initiate Ca^{2+} release from the SR [Ríos et al., 1987]. It has been shown that the type of ec-coupling is directly linked to the underlying isoforms of RyRs and DHPRs. The cardiac DHPR does not interact directly with RyR1 [Tanabe et al., 1990], nor does the skeletal DHPR induce skeletal ec-coupling with RyR2 [Nakai et al., 1997].

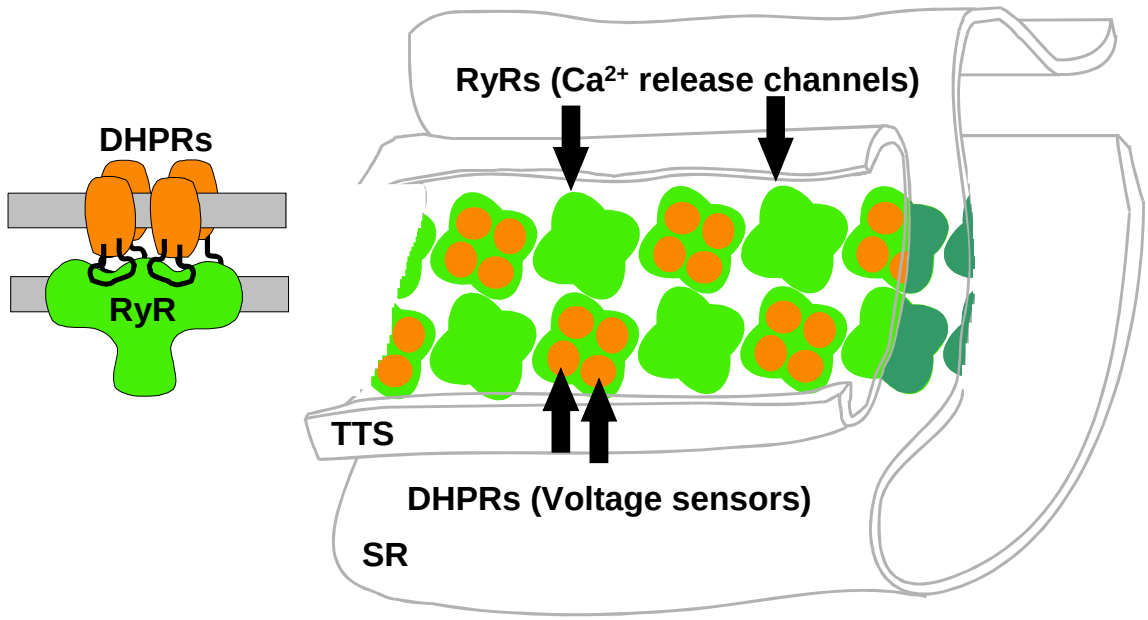

Fig. 2.4 Schematic drawing of the structure of a skeletal muscle triadic junction, the primary release site for Ca^{2+} release from the SR. Tetrads of skeletal DHPRs are co-localized with RyR1s to form a skip pattern. Figure courtesy of Dr. Ríos.

From studies with the lipid bi-layer technique, where single purified RyRs are brought into an artificial lipid membrane, two main peptide regions of the amino acid chain that constitutes the skeletal DHPR could be identified. They are both located in the II-II loop between the second and the third transmembrane segment of the protein. The first, peptide A (Thr671-Leu690), increases the open probability for the RyR, the second, peptide C (Glu724-Pro760), has an inhibitory effect on the RyR [El-Hayek et al., 1995].

All DHPRs exhibit voltage-dependent inactivation [Shirokov et al., 1992] with rate constants in the range of seconds. In addition, DHPRs require Ca^{2+} ions in the extracellular space to avoid inactivation which could cause them to not support Ca^{2+} influx [Almers et al., 1984] or skeletal type ec-coupling [Brum et al., 1988a].

The ability of DHPRs to alter their conformation upon changes in membrane potentials is due to charged amino acid groups within the protein. In skeletal ec-coupling this sensitivity to membrane potential has led to the use of the term voltage-sensor. When all ionic currents through ion channels across the membrane are inhibited, the small displacement of these charged groups during the structural change of the DHPRs can be monitored as a brief nonlinear current in voltage-clamp experiments [Schneider et al., 1973]. These gating currents or charge movements have a characteristic voltage dependence and the amount of charge movement for a certain depolarization is then closely linked to the release rate of Ca^{2+} from the SR [Brum et al.,1988b].

2.3 Structure and function of the skeletal triadic junction

Triadic junctions in skeletal muscle can contain between 20 and 80 RyRs. The RyRs together with other proteins in the SR, including triadin and junctin, are embedded in a protein matrix that enables the arrangement of RyRs in a double row as shown in Fig. 2.4. The TTS membrane contains the DHPRs, which form tetrads that are co-localized with a RyR. But only every other RyR is facing such a tetrad, thus forming a so-called skip pattern [Block et al., 1988].

This structure of the release site has consequences on the process of Ca^{2+} release from the SR. As shown in Fig. 2.5 the RyRs that are in contact with a DHPR tetrad and those not facing any voltage-sensors underlie different control mechanisms. It has been shown in voltage-clamp experiments that Ca^{2+} release from the SR can be terminated at any time by repolarization [Melzer et al., 1987]. Therefore, the DHPR determines the opening and closing of the facing RyRs. Still, it is not fully understood whether these release channels remain under complete voltage control through DHPRs when the voltage sensor is inactivated. However, during a normal release, for instance initiated by an action potential, the opening of the voltage-gated RyRs lasts tens of milliseconds. As the transition to the inactivated state needs seconds, the inactivation plays only a major role in the determination of the number of voltage-gated RyRs that can be opened by a change in TTS membrane potential.

The free RyRs are influenced by Ca^{2+} dependent activation [Pizarro et al., 1992] and inactivation [Simon et al., 1991] because of their Ca^{2+} binding sites (see 2.2.1). Therefore there exist two pathways to open and close a RyR: by voltage and by Ca^{2+} ions.

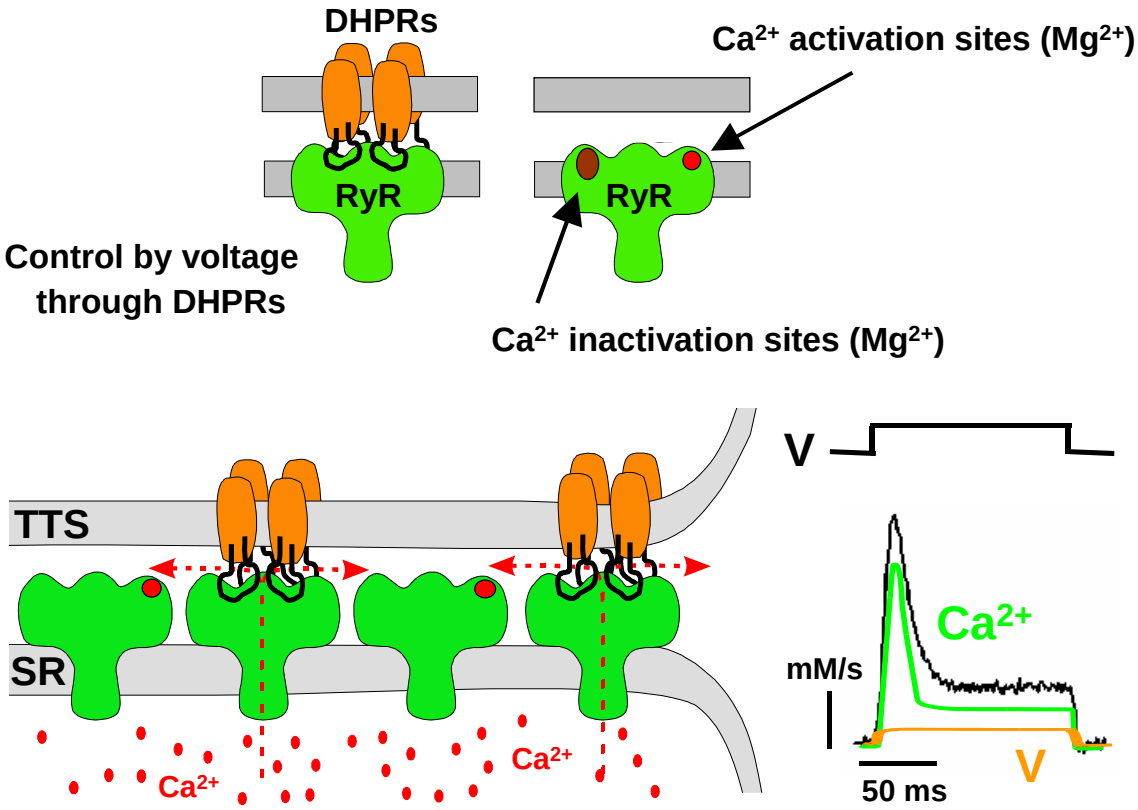

Fig. 2.5 Ca^{2+} release occurs through voltage-gated and ligand-gated RyRs. First, the voltage-operated release channels open by membrane depolarization and release Ca^{2+} ions that subsequently activate the neighboring RyRs. Bottom right: Example release record obtained by a step depolarization under voltage-clamp. Ca^{2+} release under these conditions has a characteristic time course. This has led to the proposal of the dual-control model, where the peak of release can be attributed to transient Ca^{2+} dependent signals from the ligand-gated RyRs. The voltage-gated RyRs contribute a steady release of Ca^{2+} ions. Part of the figure courtesy from Dr. Ríos.

Based on experiments with light sensitive Ca^{2+} indicators that measured whole cell Ca^{2+} release from the SR under voltage-clamp, a dual control model of Ca^{2+} release in skeletal muscle has been proposed by Ríos et al. [1988].

In voltage-clamp experiments the time course of microdomain Ca^{2+} release elicited by a step depolarization shows two different kinetical components as shown in Fig 2.5 on the bottom right (For a description on how to calculate microdomain Ca^{2+} release see 4.3.6 and 4.3.7). First Ca^{2+} release rises to a peak and thereafter declines to a more steady level, where less Ca^{2+} ions leave the SR per unit of time but overall Ca^{2+} release remains approximately constant. The dual-control model attributes the peak component directly to the purely Ca^{2+} operated RyRs. The voltage-operated RyRs contribute only to the steady component of

Ca^{2+} release, because the release can be started and terminated by voltage and the steady level appears basically in the same form for different durations of the step depolarization.

In the model the voltage-gated RyRs open as a result of the step depolarization. Then the Ca^{2+} ions released by these openings diffuse to the neighboring free RyRs and open them subsequently by binding to the Ca^{2+} activation sites. Therefore, even more Ca^{2+} is released up to a level where Ca^{2+} binds to the inactivation sites of the free RyRs and cause their closing. Hence, the opening of the free RyRs is transient and only based on the mechanism of calcium induced calcium release (CICR), while the directly voltage-operated RyRs remain open until the cell is repolarized.

Mg^{2+} ions are a very important modulator of Ca^{2+} release as stated in section 2.2, as a great part of it relies on CICR. Lamb G.D. [2000] stressed the inhibitory effect of Mg^{2+} and proposed a different model. In this model, RyRs co-localized with a DHPRs are susceptible to CICR as well, but only when the voltage sensors have been gated by a depolarization and thus have induced a preopen state of the RyRs. In this preopen state the RyRs lower their affinity for Mg^{2+} ions in such a dramatic way that Mg^{2+} ions instantly dissociate from the inactivation site, which leads to the opening of some RyRs that will trigger the opening of their neighbors.

2.4 Ca^{2+} sparks

The use of confocal laser scanning microscopy has led to the detection of localized Ca^{2+} release events in heart muscle [Cheng et al., 1993] and later in skeletal [Tsugorka et al., 1995; Klein et al., 1996] and smooth muscle [Nelson et al., 1995]. Due to their brief nature they have been termed Ca^{2+} sparks. Ca^{2+} sparks can occur spontaneously or can be triggered by voltage. An example of both is given in Fig. 2.6. At left is an xy-image of fluorescence that shows a voltage-clamped cut skeletal muscle fiber loaded with the indicator Fluo-3. To observe Ca^{2+} sparks with conventional scanning microscopes with time resolution per line of 1-2 ms, Ca^{2+} sparks are usually studied in line scanning mode along the fiber axis. The right side of the figure shows a fluorescence image of a line scan (time axis from left to right). During the acquisition a step depolarization from -90 mV, the resting membrane potential, to -65 mV was applied for 400 ms. A great number of discrete and localized Ca^{2+} signals was recorded during the depolarization (voltage triggered events), but also at a lower frequency before and after the pulse (spontaneous events). Below the line scan image are two time courses of fluorescence from the locations marked by arrows.

The occurrence of spontaneous events shows already that a direct gating of a RyR through a DHPR is not required to induce a Ca^{2+} spark. In addition, the elimination of Ca^{2+} sparks by tetracaine, a known inhibitor of CICR, suggests that CICR is involved in spark generation and that a Ca^{2+} spark is generated by more than one RyR. Furthermore, a more continuous release form lasting as long as the voltage pulse has been measured at lowest depolarization levels and was attributed to directly voltage-operated Ca^{2+} release [Shirokova et al., 1997].

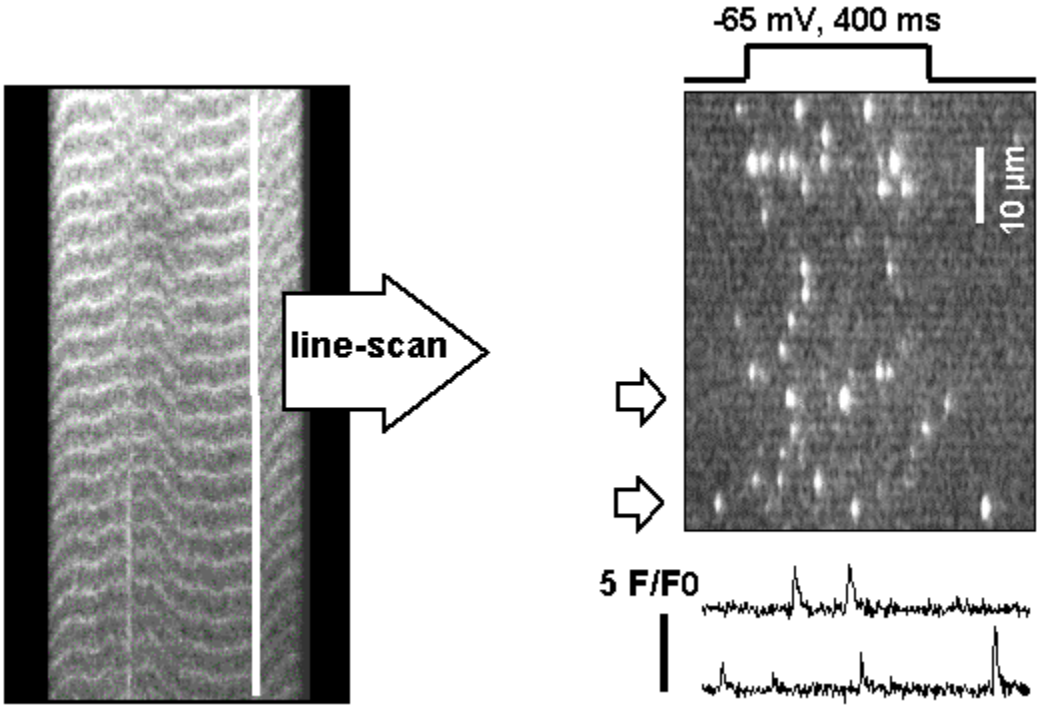

Fig. 2.6 Ca^{2+} sparks in skeletal muscle are measured with confocal laser scanning microscopy. Left: xy-image of a muscle fiber loaded with Fluo-3. The white line depicts the line scan orientation along the fiber axis. Right: Line scan image from the fiber on the left (time axis from left to right). Ca^{2+} sparks occur at all times, although with much higher frequency during an applied step depolarization from -90 mV to -65 mV for 400 ms under voltage-clamp. Below the image are two time courses of fluorescence from the locations marked by arrows. F Fluorescence, F_0 baseline fluorescence before the pulse. Figure courtesy from Dr. Shirokova.

The frequency of Ca^{2+} sparks within a line scan increases with the level of depolarization and sparks overlap at high activation voltages so that they constitute a smooth global Ca^{2+} release, as it can be measured with microdomain techniques. Thus Ca^{2+} sparks are elementary events of Ca^{2+} release. The peak of release under voltage-clamp depolarization is thought to arise from synchronized triggering of Ca^{2+} sparks at the beginning of the pulse, when all RyRs, that are not co-localized with DHPRs are not yet inactivated. The reoccurrence of Ca^{2+} sparks within a depolarizing pulse is based on fast recovery from inactivation. The observation that the microdomain Ca^{2+} release can be derived from superposition of Ca^{2+} sparks in this way combined with the finding that spontaneous and voltage-triggered Ca^{2+} sparks have a quite uniform appearance have led to the speculation that a Ca^{2+} spark is produced by the opening of one single RyR [Klein et al., 1997].

The highly localized Ca^{2+} gradients caused by Ca^{2+} sparks extend for only a few micrometers and can be measured with sub-micron precision. A detailed description on how to measure Ca^{2+} sparks can be found in the Materials and Methods section.

2.5 From amphibian to mammalian muscle

For decades studies in ec-coupling and Ca^{2+} release have mostly been carried out in adult differentiated muscle preparations, as scientists try to exclude any unnecessary differences from alterations in Ca^{2+} regulation during the development of the muscle fiber. Studies have shown that the same characteristic time course of microdomain Ca^{2+} release exists in amphibian and mammalian skeletal muscle under voltage-clamp [Garcia J. et al., 1993; Melzer et al., 1986b], although in mammalian voltage-clamped cut fiber preparations the overall Ca^{2+} release was somewhat smaller. The only striking difference found was in the voltage dependence of the ratio between the peak of release and the steady level, which showed a distinct bell-shape in amphibians, but was basically constant in mammalians. As the peak of release can be attributed to CICR (see 2.2.3), this ratio is an indicator for the relative contribution of CICR to Ca^{2+} release. Hence, it was reasoned that mammalian muscle fibers could exhibit less CICR and remain more under the control of voltage than amphibians [Shirokova et al., 1996b].

Another evidence of enhanced voltage control of release in mammalians is the phenomenon of repolarization induced stop of caffeine induced release (RISC) that is present in mammalians [Suda et al., 1994], but not amphibians [Shirokova et al., 1996a]. Experiments on RISC consist first of an application of caffeine, which results in Ca^{2+} release from the SR. This is at first followed by a depolarization, which enhances Ca^{2+} release, and then by a repolarization. The repolarization completely stops the release only in mammalians.

In nanodomain Ca^{2+} release, there is evidence that CICR is crucial for the generation of Ca^{2+} sparks. Interestingly, Ca^{2+} sparks are very frequent in adult skeletal amphibian muscle, but to date in experiments with adult skeletal mammalian muscle they have been either absent in voltage-clamped cut skeletal muscle fibers [Shirokova et al., 1998] or they have appeared very infrequently in intact fibers [Conklin et al., 1999]. Scientists have thus far been unable to show abundant elementary Ca^{2+} release in adult mammalians. However, in developing mammalian muscle Ca^{2+} sparks are as frequent as in amphibians, exhibiting an even greater variety in widths and durations. Also their existence does not depend on any underlying isoform of RyR, although differences in spark morphology (FWHM, duration. etc.) have been reported [Shirokova et al., 1999; Conklin et al., 1999; Ward et al., 2000].

3 Determination of free ion concentrations with light-sensitive indicators

Intracellular ion concentrations can be measured with a variety of methods, including NMR techniques and ion selective electrodes. However, the most successful tools to measure the free Ca^{2+} ion concentration in living cells have been Ca^{2+} selective dyes that change their optical properties upon binding to Ca^{2+} ions. In addition to their high selectivity for Ca^{2+} ions they are easy to use and suitable for measurements of fast changes in the Ca^{2+} concentration (ms range). Binding of Ca^{2+} ions to Ca^{2+} dyes changes their absorption or emission spectrum. This is due to the interaction of the dye-bound Ca^{2+} ions with the electrons of the dye, which for fluorescence dyes usually involves some conjugated double bonds within the dye molecule [Thomas M.V., 1982]. By measuring the transmitted or emitted light intensity, it is possible to distinguish between the free and bound dye within a probe. Furthermore, with the knowledge of the corresponding dissociation constant, one can determine the underlying free Ca^{2+} concentration.

3.1 Theory of absorption and fluorescence

Absorption

In quantum theory the absorption process can be understood as the transition of a system from one energy state into another by annihilation of a photon. The energy difference ΔE between the two states corresponds then to the photon energy $h\nu$, where h is the Planck constant and ν is the frequency of the photon. Every molecule has its characteristic absorption spectrum according to its possible energy states and will therefore contribute to absorption within matter.

Macroscopically, the decline in radiation intensity by absorption can be described by

$$I_T = \hat{I} \cdot e^{-p\alpha(\lambda)}, \tag{3.1}$$

where I_T is the transmitted intensity, $\hat{I}$ is the incident intensity, p is the path length through the studied probe and $\alpha(\lambda)$ is the absorption coefficient. This is Bouguer-Beer´s law of absorption in matter.

The absorption, which within solutions is also called extinction, is defined as

$$A(\lambda) = \log\left(\frac{\hat{I}}{I_T}\right) = p \cdot c \cdot \varepsilon(\lambda), \tag{3.2}$$

where c is the concentration of the absorbing solvent and $\varepsilon(\lambda)$ is the extinction coefficient. This is the law of Lambert-Beer.

Using these equations it is possible to measure concentrations of absorbing substances via light intensities when the path length is known. It should be stated that the above laws neglect scattering processes and thus one is urged to use long wavelengths in experiments (Rayleigh scattering $\sim 1/\lambda^4$) to minimize errors.

Fluorescence

After a system in the ground state has absorbed a photon and is now in an electronically excited state, it can relax back to its ground state by either re-emitting a photon or by radiationless decay. The process of re-emission is called luminescence. If the luminescence is due to a quantum theory allowed transition into the ground state this process is referred to as fluorescence, if the transition is not allowed after quantum mechanical rules it is called phosphorescence. The lifetimes of the excited states for phosphorescence is in the order of milliseconds to seconds and can in single cases even reach days [Vogel H., 1995]. This is in contrast to fluorescence decays which usually occur within 10^{-7}-10^{-9} s after absorption [Lakowicz J.R., 1983].

The processes and the lifetimes involved in fluorescence are schematically shown in Fig. 3.1. From the ground state S_0 the fluorophore is normally excited into some higher vibrational states of S_1, S_2 or S_3. Immediately thereafter part of the energy is transferred to the surrounding medium as heat and the system thereby relaxes to the lowest vibrational state of S1. This is called internal conversion and it occurs within 10^{-12} s. After solvent relaxation the emission of a photon or radiationless decay from $S_{1'}$ returns the system into one of the vibrational states of S_0 [Lakowicz J.R., 1983]. As can be seen the emitted photons are usually of higher wavelength then the absorbed photons. This effect is termed Stokes shift and with the use of optical interference filters it allows the detection of emitted photons without any contribution of the incident light source, thus leading to a low background and a higher signal to noise ratio in experiments.

The intensity that is absorbed by a fluorescent indicator is just the difference between the incident intensity $\hat{I}$ and the transmitted intensity I_T given by Bouguer-Beer´s law. In addition a proportionality factor, termed quantum yield, is introduced which is defined as

$$q = \frac{number\ \ of\ \ fluorescence\ \ photons}{number\ \ of\ \ absorbed\ \ photons}. \tag{3.3}$$

Then the intensity due to fluorescence can be written as

$$I_F = q \cdot (\hat{I} - I_T) = q \cdot \hat{I} \cdot \left(1 - e^{-p \cdot c \cdot \varepsilon(\lambda)}\right). \tag{3.4}$$

In the case of a low indicator concentration $\left(c \cdot \varepsilon(\lambda) << 1\right)$, the exponential function can be expanded in a Taylor series, where only constant and linear terms contribute significantly to the fluorescence intensity, which can then be approximated as

$$I_F \cong q \cdot \hat{I} \cdot p \cdot c \cdot \varepsilon(\lambda). \tag{3.5}$$

For low fluorophore concentrations one can also neglect the inner filter effect, where the fluorophore itself reabsorbs part of the emitted fluorescence photons and thus decreases the fluorescence output. In addition interactions with the solvent or other solutes, i.e. quenching, can attenuate the fluorescence intensity.

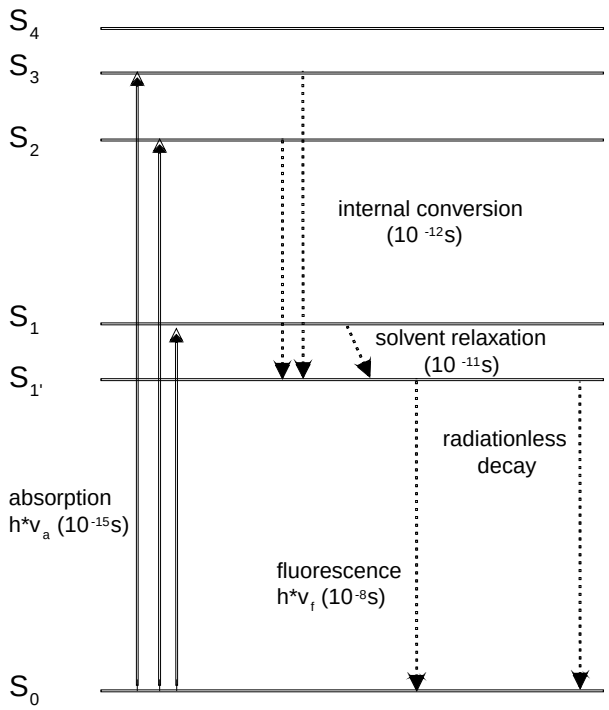

Fig. 3.1 Schematic drawing of typical transitions between energy states and their lifetimes for a fluorophore. Absorption occurs from the ground state S_0 to electronically excited states S_1,S_2,S_3, etc. Further subdivision of all energy levels into the vibrational states is not shown. S1´ corresponds to the S1 state lowered by solvent relaxation. Adopted from Lakowicz J.R. [1983], taken from Uttenweiler et al. [1999].

3.1.1 Absorption measurement of [Ca^{2+}] and [Mg^{2+}] with Antipyrylazo III

Antipyrylazo III (ApIII) [Scarpa et al., 1978] is a metallochromic Ca^{2+} indicator that has already been used to study the Ca^{2+} release from the SR [Kovács et al., 1979]. ApIII changes its absorption spectrum when either the free Ca^{2+} concentration, [Ca^{2+}], or the free Mg^{2+} concentration, [Mg^{2+}], is altered. It exhibits its most prominent change in the absorption at 720 nm for a change in [Ca^{2+}]. ApIII has no isosbestic point in the absorption spectrum for Ca^{2+} ions and the absorption vanquishes at wavelengths greater than 780 nm. For a change in [Mg^{2+}] the greatest change in the absorption is at 600 nm and there exists an isosbestic point in the spectrum at 550 nm. Absorption spectra for different [Mg^{2+}] are shown on the right hand side of in Fig. 3.2 (normalized to the absorption at 550 nm). Because 550 nm is an isosbestic point for the reaction with [Mg^{2+}], this wavelength is usually used for calibrations to determine the dye concentration in the cell, as there will be no interference by Mg^{2+} ions [Kovács et al., 1983].

The stoichiometry of the reaction of ApIII with Mg^{2+} ions is 1:1 [Ríos et al., 1981]. Therefore in equilibrium there exists a first order dissociation constant given by

$$K_{MgDye} = \frac{[Mg^{2+}]\cdot[Dye]}{[DyeMg^{2+}]}, \tag{3.6}$$

where $[Dye]$ is the free concentration of ApIII and $[DyeMg^{2+}]$ is the concentration of ApIII bound to Mg^{2+} ions.

The reaction with Ca^{2+} ions follows a stoichiometry of 1:2 [Ríos et al., 1981]. Thus, the equilibrium is given by a second order dissociation constant

$$K_{CaDye} = \frac{[Ca^{2+}]\cdot[Dye]^2}{[Ca(Dye)_2]}, \tag{3.7}$$

where $[Ca(Dye)_2]$ now denotes the concentration of ApIII bound to Ca^{2+} ions.

Introduction of the total ApIII concentration,

$$Dye_t = [Dye] + 2[Ca(Dye)_2], \tag{3.8}$$

yields

$$K_{CaDye} = \frac{[Ca^{2+}]\cdot(Dye_t - 2[Ca(Dye)_2])^2}{[Ca(Dye)_2]}. \tag{3.9}$$

In cells both divalent ions are always present, hence the Mg^{2+} ions interfere with the binding of ApIII to Ca^{2+} ions. However, [Mg^{2+}] is expected to not change significantly within microdomains during Ca^{2+} release, as its concentration is in the range of 0.4-1 mM. The quantification of Ca^{2+} signals within cells then requires the use of an apparent dissociation constant for the binding of Ca^{2+} ions that corrects for the presence of free Mg^{2+} ions.

According to simultaneous reactions with the two ions the total concentration of ApIII can be expressed as

$$Dye_t = [Dye] + 2[Ca(Dye)_2] + [MgDye]. \tag{3.10}$$

It is convenient to introduce

$$\alpha = \frac{K_{MgDye}}{[Mg^{2+}] + K_{MgDye}}, \tag{3.11}$$

which is the magnesium-free fraction of the calcium-free dye. Then from all equations in this sections it follows that

$$\frac{K_{CaDye}}{\alpha^2} = \frac{[Ca^{2+}] \cdot (Dye_t - 2[Ca(Dye)_2])^2}{[Ca(Dye)_2]}. \tag{3.12}$$

The apparent dissociation constant for Ca^{2+} binding, $\tilde{K}_{CaDye}$, is then related to K_{CaDye} by

$$\tilde{K}_{CaDye} = \frac{K_{CaDye}}{\alpha^2} = K_{CaDye} \cdot \left(\frac{[Mg^{2+}] + K_{MgDye}}{K_{MgDye}} \right)^2. \tag{3.13}$$

It becomes clear that once a calibration of the equilibrium constants of the dye in the used optical system has been carried out separately for each divalent ion, the apparent dissociation constant can be derived rapidly with eqn. 3.13 if $[Mg^{2+}]$ is known. This can be established by measuring $[Mg^{2+}]$ when cells are at rest, as $[Ca^{2+}]$ is low then.

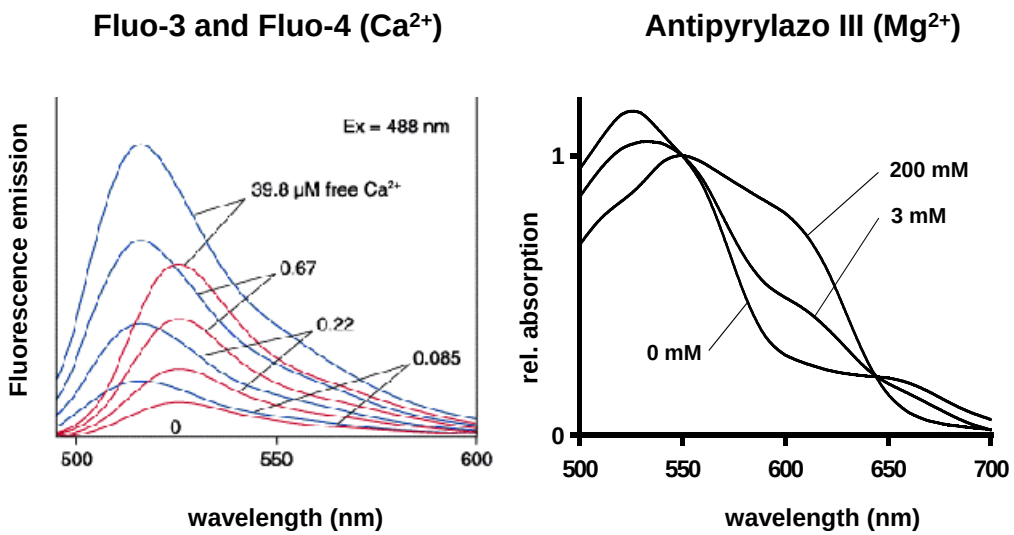

Fig. 3.2 Left: Fluorescence emission spectra of Fluo-3 (red) and Fluo-4 (blue) at an excitation wavelength of 488 nm for various $[Ca^{2+}]$. Fluo-4 has a higher fluorescence output than Fluo-3. (Taken from the product information web page of Molecular Probes, www.molecularprobes.com). Right: Absorption spectrum of Antipyrylazo III for various $[Mg^{2+}]$ normalized to the absorption at 550 nm.

3.1.2 Fluorescence measurements of [Ca^{2+}] with Fluo-3 and Fluo-4

The fluorescence Ca^{2+} indicators Fluo-3 and the newer conjugate Fluo-4 exhibit their absorption maximum in the visible part of the spectrum at around 490-505 nm. Thus they are an ideal tool for the excitation with the 488 nm line of an Ar-ion or Ar/Kr-ion laser. Because of their medium range affinity (about 1 µM in the intracellular medium [Harkins et al., 1993]) and the fact that the free dyes are almost non-fluorescent, they are suitable to measure spatially resolved Ca^{2+} signals with a relatively high signal to noise ratio. Utilizing confocal laser scanning microscopy Fluo-3 has been the standard dye to measure Ca^{2+} sparks [Tsugorka et al., 1995; Klein et al., 1996; Shirokova et al., 1997 and 1998]. When complexed to Ca^{2+} ions the fluorescence of Fluo-3 can increase about 50-100 fold and Fluo-4 even surpasses this increase about 2 fold. The fluorescence emission spectra for both dyes are shown in Fig. 3.2 in the left panel.

Both dyes have a 1:1 stoichiometry for binding to Ca^{2+} ions. Hence, a similar relation as shown in eqn. 3.6 applies in equilibrium (exchanging “Ca” for “Mg” in the formula). The affinity for Mg^{2+} ions is in both cases negligible in physiological experiments. The relatively long excitation wavelength reduces effects of photo damage, cell-autofluorescence and light scattering compared to commonly used UV-excited dyes like Fura-2 and Indo-1.

3.2 Fluorescence Microscopy techniques

Increasing interest in intracellular Ca^{2+} signaling in the past decade has motivated the development of sophisticated techniques for the measurement of changes in calcium concentrations. The most commonly used tools are fluorescence indicators in conjunction with microscopy techniques. New fluorescent dyes, especially for the use in ratiometric measurements, have been used in epi-illuminated fluorescence microscopy [Uttenweiler et al., 1998]. Confocal laser scanning microscopy now allows the measurement of elementary Ca^{2+} release events [Cheng et al., 1993] and two photon excitation microscopy enables the spatially restricted dissociation of so-called ´caged compounds´
[Lipp et al., 1996].

3.2.1 Epi-illuminated fluorescence microscopy

In standard fluorescence microscopy of cells the fluorescence light from a large fraction of the epi-illuminated cell is collected by a photo diode or a photo multiplier which measure timely resolved changes of intracellular Ca^{2+} concentrations. These measurements yield spatially greatly averaged signals. However, the analog setup of the photon detectors allow a high time resolution in the measurement of macroscopic changes in [Ca^{2+}], that can occur within milliseconds. Thus, it is still a good method to use when one is interested in dynamic

macroscopic Ca^{2+} signals. The errors in the quantification of the Ca^{2+} signals due to "assumed" intracellular dye concentrations or incorrect calibrations can be reduced with the use of ratiometric methods. Analyzing ratios of fluorescence signals obtained at either different excitation wavelengths (i.e. Fura-2) or different emission wavelengths (i.e. Indo-1) eliminates parameters like the dye concentration or the illumination intensity.

For instance with Fura-2, which shifts its excitation spectrum upon binding to Ca^{2+} ions, one can establish a dual-excitation ratio measurement. Let R be the ratio of the two fluorescence intensities F_1 and F_2 that correspond to the wavelengths λ_1 and λ_2. Then the free Ca^{2+} concentration in equilibrium can be obtained from the simple formula

$$\left[Ca^{2+}\right] = K_{Cadye} \cdot \beta \cdot \frac{R - R_{\min}}{R_{\max} - R}, \tag{3.14}$$

where $R_{\max}$ and $R_{\min}$ are the ratios of fluorescence intensities at a saturating calcium concentration and in the absence of Ca^{2+} ions, β is the ratio of fluorescence intensities for the free and the bound dye at λ_2 and K_{Cadye} is the dissociation constant for Fura-2 binding to Ca^{2+} ions [Grynkiewicz et al., 1985].

Digital cameras enable the measurement of spatially resolved Ca^{2+} signals and the now available products make it, in principal, possible to observe spatially restricted Ca^{2+} signals in the ms range, although at a lower time resolution compared with standard photometric systems. In addition, improved digital image analysis methods can increase the depth resolution of data, i.e. by removing out of focus information by deblurring algorithms [Agard et al., 1984; Monck et al., 1992].

3.2.2 Confocal laser scanning microscopy

An observed specimen is a three-dimensional object and can be viewed as a stack of object planes perpendicular to the optical axis. In conventional microscopy information from all of these axial planes contribute to the formation of the image, although object parts become more diffracted with greater distance from the focus plane. This out of focus information disturbs the interpretation of spatially restricted signals as one has not enough information about its origin.

With confocal microscopy the depth resolution is greatly improved. This is established by inserting a pinhole into the optical pathway in front of the detector so that only light from the focal plane is completely transmitted through the pinhole. Light from points out of focus is severely reduced in intensity as the diffracted disks are greater than the pinhole and, therefore, only part of the information of these points will reach the detector. The thus achieved depth discrimination is then limited by the size of the pinhole (see Fig. 2.3). In addition to the wavelength and the numerical aperture of the objective, the pinhole also contributes to the lateral resolution of the system.

For the observation of extended objects a laser beam passes a scan unit before it is coupled into the microscope and focused on the specimen. The movement of the laser spot on the object level is usually controlled by galvanometric mirrors in the scan head, which for very fast scan rates can also be realized via acusto-optical mirrors (AOM). The laser excited fluorescence photons are normally detected with photo-multipliers.

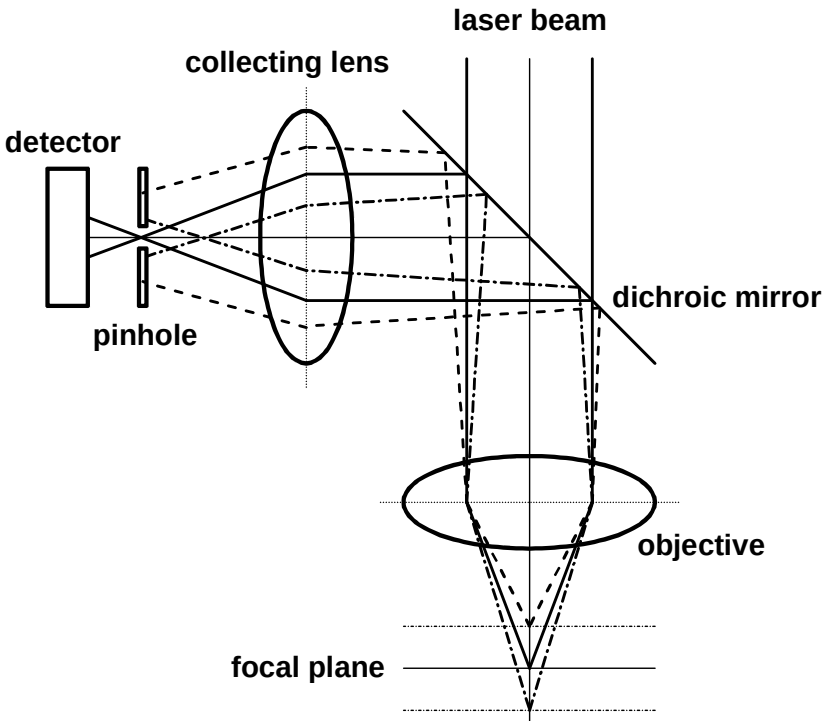

Fig. 3.3 The principal of depth discrimination in confocal microscopy. Only light from the focal plane is completely transmitted through the pinhole in front of the detector. From Feierabend M. [1999].

The resolution of the optical system is basically given by the full width at half maximum (FWHM) of its point spread function (PSF) in the respective direction. The PSF of a confocal system can be measured as the diffracted intensity distribution obtained by imaging a sub-resolution fluorescence bead. For an ideal, point-shaped pinhole the PSF can be exactly calculated using the paraxial approximation as shown in Wilson [1990]. In this case the axial intensity distribution in optical units u is given by

$$I(u) = \left(\frac{\sin(u/4)}{u/4} \right)^4 , \tag{3.15}$$

where $u = 0$ marks the center of the PSF. The axial optical units are related to the real axial coordinate r_z by

$$u = \frac{8\pi}{\lambda} \cdot n \cdot \sin^2(\alpha/2) \cdot r_z . \tag{3.16}$$

In this formula λ is the considered wavelength and $n \cdot \sin\alpha$ corresponds to the numerical aperture of the system.

The lateral intensity distribution in optical units v is then

$$I(v) = \left(\frac{2J_1(v)}{v} \right)^4, \tag{3.17}$$

where J_1 is the first order, first grade Bessel function. The lateral optical units are defined as

$$v = \frac{2\pi}{\lambda} \cdot n \cdot \sin\alpha \cdot r_{xy}. \tag{3.18}$$

Again λ and $n \cdot \sin\alpha$ are the wavelength and the numerical aperture, respectively. The lateral radius of the PSF is denoted as r_{xy}.

The same calculation can be carried out for a conventional microscope which yields under the same assumptions an axial intensity distribution of

$$I(u) = \left(\frac{\sin(u/4)}{u/4} \right)^2 \tag{3.19}$$

and a lateral intensity distribution of

$$I(v) = \left(\frac{2J_1(v)}{v} \right)^2. \tag{3.20}$$

Hence, the two systems are different in that the confocal microscope has a fourth order dependence and the conventional microscope has only a second order dependence on the respective functions. This is due to the fact that the pinhole resembles a minimal detector size and that therefore also the lens in front of the pinhole matters for the detected intensity, which is not the case in the conventional microscope.

Therefore, the differences in the optical setup result, in this ideal case, in an approximately 1.4 fold improvement of lateral as well as axial resolution of the confocal microscope.

In reality the pinhole cannot be point-shaped, causing the obtained resolutions to be sub-optimal. A too small pinhole results in a great loss of signal in a low level fluorescence environment. This could be compensated by an increase in excitation intensity. However, in cell physiological experiments, this is not only limited by photobleaching of the indicator, but also by possible photodamage to the cell. Thus, the size of the pinhole is usually determined by a good compromise between the resolution improvements and a suitable signal to noise ratio.

3.2.3 Two photon excitation laser scanning microscopy

The spatially restricted excitation of fluorescence by means of two photon absorption can also serve as a basis for a scanning microscope. In two photon excitation two photons are simultaneously absorbed by the indicator. The two photons can be of the same wavelength, which in turn is then longer than the one photon emission wavelength. The probability for a fluorophore to absorb a photon-pair depends on the square of the instantaneous light intensity. This is why pulsed lasers are used for the excitation, as very brief but intense pulses increase the average absorption probability compared to continuous wave lasers for the same average laser power [Denk et al., 1995]. With the paraxial approximation the absorption probability at the center of the focused laser spot during a single pulse can be related as [Denk et al., 1990]

$$p_{abs} \propto \xi \cdot \frac{\delta \cdot \langle P \rangle^2}{f_p} \cdot \left(\frac{\pi \cdot {A_{NA}}^2}{h \cdot c \cdot \lambda} \right)^2, \tag{3.21}$$

where δ is the two photon cross-section of the fluorophore, $\langle P \rangle$ is the average laser power, f_p is the pulse repetition frequency, A_{NA} is the numerical aperture of the objective, h is the Planck constant, c is the speed of light in vacuum and λ is the wavelength. The factor ξ is called the two-photon advantage and depends on the shape of the laser pulse in time.

The absorption spectra for one and two photon absorption of the same fluorophore can be different as the quantum mechanical selection rules for the allowed transitions are not the same (Birge R.R., 1979), thus for complex molecules like fluorescence indicators the cross sections for two photon absorption can usually not be predicted. However, the fluorescence emission spectra are basically unaltered, as they are always related to a one photon process (Curley et al., 1992).

In two photon excitation laser scanning microscopy (TPLSM) the spatial resolution is obtained by the quadratic dependence of the absorption probability on the laser power, which yields efficient excitation of fluorophores only near the focus. Usually, the spatial resolution obtained with the same fluorophore is better in a confocal system than in a two photon excitation system [Sheppard et al., 1990; Nakamura et al., 1993]. However, TPLSM does not require a pinhole and thus allows a more effective collection of photons, as all detected light stems from the excited volume. Therefore, the resolution of a TPLSM can be greatly improved by an increase in detector size, i.e. by means of a 4-Pi microscope (Hell et al., 1992).

One of the main advantages of a TPLSM is the reduction of photodamage in the cell. This results on the one hand from the longer excitation wavelength that is less absorbed by cell compounds. On the other hand it is based on the fact that photodamage at the excitation wavelength of the dye occurs only within the spatially restricted absorption volume. In confocal or conventional microscopy photodamage at this wavelength will be caused all along the light beam inside the object. This is true especially with the use of dyes that normally

absorb in the UV part of the spectrum, where the two photon excitation wavelength is then in the visible range. Still, the greater wavelength of the laser induces a higher amount of heat at the focal spot, as absorption by water is enhanced in the near infrared.

Instead of the excitation of a fluorophore, the TPLSM can be used for the local dissociation of caged compounds, where absorption in the UV range is usually required to break the caging bonds.

4 Materials and Methods

4.1 Physiological preparations

The goal of this study was the measurement and quantification of micro- and nanodomain Ca^{2+} release from the SR in skeletal muscle fibers, a process that is highly dependent on the intracellular environment of the muscle fiber. Therefore, two fiber preparations were used that allow direct access to the myoplasm, the voltage-clamped cut fiber and the chemically permeabilized or ´skinned´ fiber. They differ from an intact fiber as indicated in Fig. 4.1.

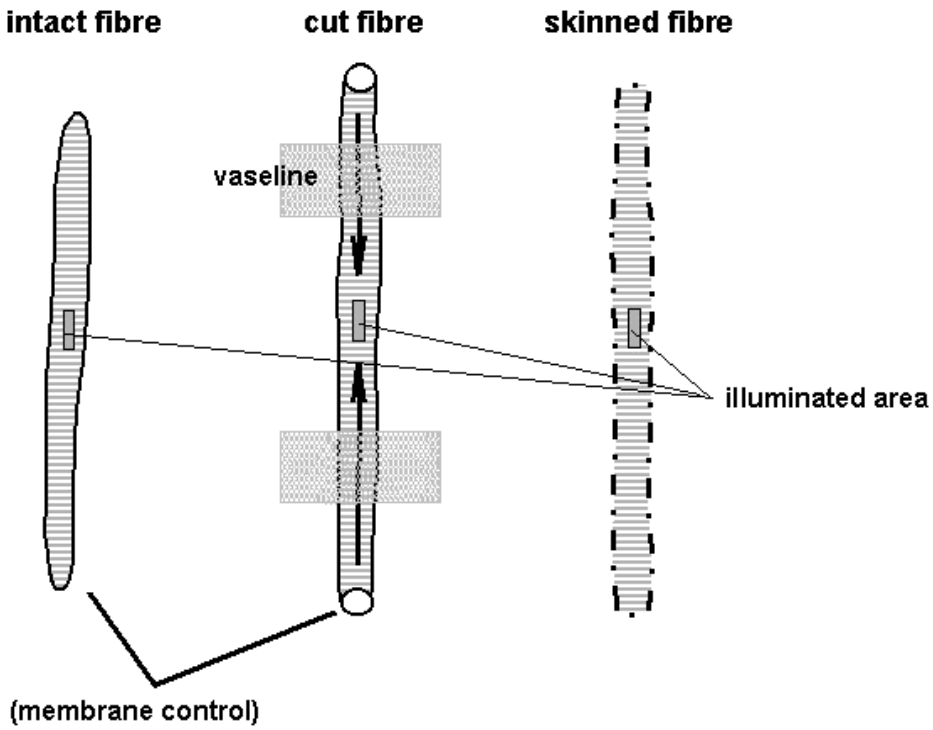

Fig. 4.1 General differences in fiber preparations.

The cut fiber preparation in muscle research was invented by Hille et al. [1976] and is used in combination with the so-called vaseline gap technique. In this method single muscle fibers are mounted into an experimental chamber with three solution pools (see section 4.2.1 for

more details), so that the cut ends of the fiber are fixed to the end pools and the rest of the fiber stretches through the middle pool. The three pools are then electrically isolated by vaseline, which is put around the fiber and the chamber walls between different pools. The cut ends of the fiber are then further permeabilized by temporal exposition to saponin (0.01% for 2 min). The middle section of the fiber membrane can then be voltage-clamped, where the electrical contact to the fiber interior is established through the permeabilized ends of the muscle fiber in the end pools. In addition, the permeabilized ends allow diffusional access to the myoplasm. Because the end pools have a much larger volume than the interior of the muscle fiber, the concentration in the middle section of the fiber - where Ca^{2+} release is actually measured - will equilibrate with time with the solute concentrations set in the end pools.

The chemically skinned fiber preparations contain 1-5 single fibers that are fixed to the bottom of a one pool chamber The temporal exposition to a skinning solution, containing saponin, permeabilizes the whole extracellular membrane, but not the membrane of the SR [Fink et al., 1984]. This allows studies on calcium release with an even more controlled setting of intracellular solute concentrations as equilibration with the bath solution is achieved within less than a second.

4.1.1 Solutions

The studied muscle fibers have been isolated from their physiological environment. To keep all compounds of the cell that are the object of study working as in a living body, it is necessary to simulate this environment. This counts especially for the ional composition of the aqueous solutions in which the fibers are dissected and studied. The natural free concentrations for simple ions in the intra- and extracellular space are well known [Schmidt R.F., et al 1993] and are thus the basis for the design of the used experimental solutions. For the setting of multiple free ion concentrations the interactions with the other ions have to be taken into account. Therefore, based on the binding properties of the solutes, the total and free ion concentrations have been calculated with the program REACT developed by Smith and coworkers [Smith et al., 1985].

This program utilizes an iteration procedure developed by Fabiato et al. [1979]. Together with the determination of free and total ion concentrations for the ligands and metal ions, this program calculated the pH and the ionic strength (IS) of the solution. This is necessary, as dissociation constants for the binding of charged particles are dependent on IS and temperature. The correction of the dissociation constants for a different IS and temperature is based on the Debye-Hückel theory [For a detailed review see Kirsch W.G., 1997].

The absolute concentrations of all substances in the experimental solutions used are given in table 4.1 and 4.2. The Ringer solutions for the respective species simulate the natural external ion compositions and were used to store the complete muscle in between dissections of single fibers for the experiment. The relaxing solutions were used during dissection,

because the exchange of K^+ for Na^+ ions causes a long time depolarization and thus an inactivation of the DHPRs, thus the fibers cannot be contractively activated during that time by changes in voltage, which could be caused by fiber cutting.

	frog		mouse	
	ringer	relaxing	ringer	relaxing
NaCl	115	-	145	-
NaOH	for pH 7.0	-	for pH 7.2	-
KCl	2.5	-	5	-
KOH	-	for pH 7.0	-	for pH 7.0
$CaCl_2$	1.8	-	2.5	0.3
$MgCl_2$	-	2	1	10
K-glutamate	-	120	-	140
EGTA	-	1	-	1
HEPES	10	10	10	10
glucose	5	5	10	5
pH	7.0	7.0	7.2	7.0

Table 4.1 Ionic composition of preparation solutions (all values are in mM).

A variety of solutions that were used for the recording of Ca^{2+} signals was prepared. The voltage-clamped cut fibers were surrounded by an external solution, in which the major metal ions, except Ca^{2+} ions, were substituted and channel blockers were included to decrease possible fluxes through ion channels in the external membrane and therefore ensure that the fiber was properly voltage-clamped during depolarizations.

All other solutions in Table 4.2 are internal solutions and thus contain ATP and in addition creatine phosphate (CP) and glucose as an energy back-up system. In all internal solutions the free Ca^{2+} ion concentration was set to 100 nM by the addition of $CaCl_2$. The reference solution for the micro- and nanodomain Ca^{2+} release experiments refers to voltage-clamped cut fibers and is in both cases based on Cs-glutamate so that fluxes of ions through the external membrane are minimized. In reference solutions the calculated free Mg^{2+} ion concentration was 0.61 mM and the difference between the micro- and the nanodomain solution is the total EGTA concentration. EGTA is mainly introduced into a solution for the effective buffering of low concentrations of $[Ca^{2+}]$, but due to its buffer capacity in higher concentrations it can also prevent severe contraction of muscle cells for short depolarizations, as it was needed in the microdomain experiments. The high Mg solution was the same in micro- and nanodomain experiments and the free Mg^{2+} ion concentration was buffered by $MgSO_4$ to be 7.0 mM. The washout solution contained citric acid as a buffer for Mg^{2+} ions and the calculated free Mg^{2+} ion concentration was 0.13 mM. The solutions for chemically permeabilized fibers are basically identical with the reference solution for nanodomain experiments, their $[Mg^{2+}]$ was set to 0.4 mM for frog and 0.61 mM for mouse.

	voltage-clamped cut fibers					permeabilized fibers	
	microdomain			nanodomain			
	external	reference	high Mg	reference	washout	frog	mouse
TEA-OH	130	-	-	-	-	-	-
TTX	0.001	-	-	-	-	-	-
3,4 Di-AP	1	-	-	-	-	-	-
CsOH	-	for pH	for pH	for pH	for pH	for pH	-
citric acid	-	-	-	-	5	-	-
Cs-glutamate	-	110	105	115	110	110	-
K-glutamate	-	-	-	-	-	-	140
CH_3SO_3	150	-	-	-	-	-	-
$MgCl_2$	-	1	-	0.5	-	0.25	5
$MgSO_4$	-	-	17	-	-	-	-
$Ca(OH)_2$	10	-	-	-	-	-	-
$CaCl_2$	-	1.72	0.19	0.25	0.27	0.25	0.1
HEPES	-	10	10	10	10	10	10
TRIS	5	-	-	-	-	-	-
EGTA	-	10	1	1	1	1	0.5
CP	-	5	5	5	5	5	5
glucose	-	5	5	5	5	5	5
Mg-ATP	-	5	5	5	5	5	-
Na_2-Atp	-	-	-	-	-	-	5
pH	7.0	7.0	7.0	7.0	7.0	7.0	7.0
mosmol/kg	275	260	260	260	260	260	300

Table 4.2 Ionic composition of external and internal solutions (all values are in mM).

4.1.2 Dissection of single muscle fibers

Ca^{2+} release from the SR in skeletal muscle was studied in three animal species. Single muscle fibers were dissected from *semitendinosus* muscle of the frog *Rana pipiens*, from *tibialis anticus* muscle of the frog *xenopus leavis* and from *extensor digitorum longus* (EDL) muscle of *Balb/c* mice and *whistar* rats. Frogs were sacrificed by decapitation and pithing after being deeply anaesthetized by immersion in a 15% ethanol-water solution, while mice and rats were sacrificed by the exposure to a high dose of CO_2. In all cases the respective muscle was surged from the animal immediately after the time of death and kept in Ringer solution in the fridge at 4°C. In all cases the muscle was stretched and fixed to the bottom of a sylgard coated petry dish by darting insect needles through the tendons. Single fiber dissection was carried out in the relaxing solution for the respective species and followed the procedure described in Kovács et al. [1983]. Thereafter the fiber was transferred and mounted in either a double vaseline gab chamber or a skinned fiber chamber, which are described in section 4.2.1.

4.1.3 Voltage-clamp

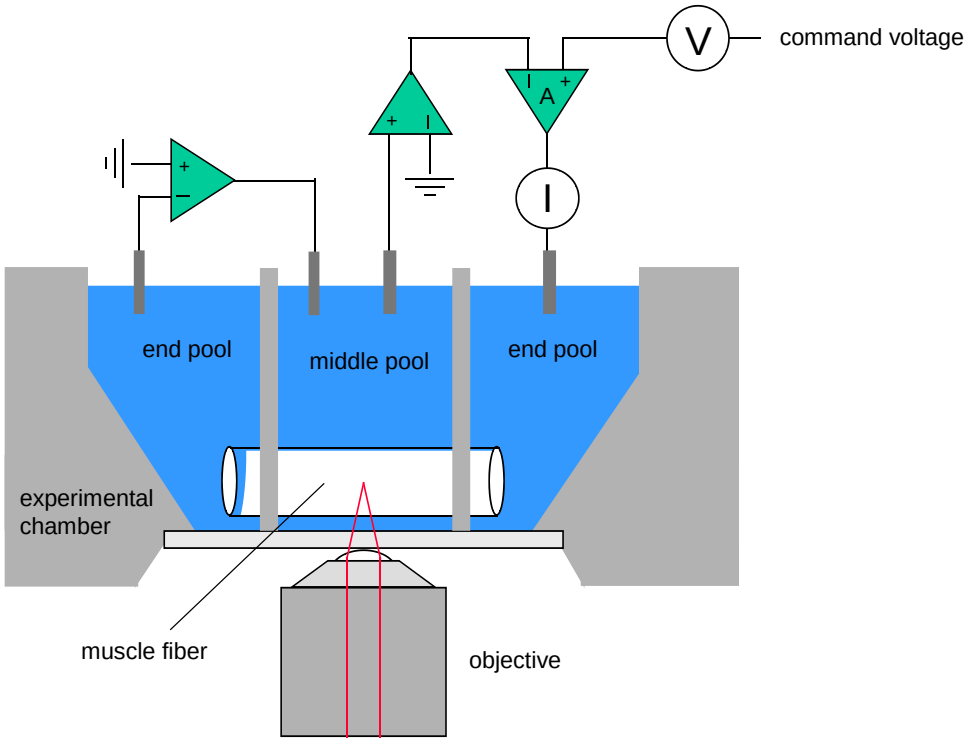

Fig. 4.2 The principal of voltage-clamp in a double vaseline gap chamber. Voltage control of the cell membrane is achieved by an inversely coupled feed-back circuit, which compensates currents across the membrane that would otherwise deviate the membrane potential from the set command voltage.

The opening of voltage-gated ion channels is mainly dependent on the potential across the membrane, therefore the invention of the basic voltage-clamp technique [Cole K.S., 1982] and their further improvements, like the patch-clamp technique [Neher et al., 1976] has been an important advance for electrophysiology. Voltage-clamp was used on cut skeletal muscle fibers mounted in a vaseline-gap chamber to control the opening and closing of DHPRs that trigger the Ca^{2+} release from the SR.

This method is based on an inversely coupled feed-back circuit as shown, in principal, in Fig. 4.2. The potential at the interior of the fiber at one end pool is inversely compared to ground and any difference is added to the potential of the bathing solution. The potential of the bathing solution is then equal to the potential across the membrane. The membrane potential measured in bathing solution is then inversely compared with a command voltage V by operational amplifier A. Any difference in potential at the input of operational amplifier A results in a compensation current I injected into the interior of the fiber at the other end pool

that has the inverse sign of the current actually flowing across the membrane, hence the membrane potential is clamped constantly to the value of the command voltage.

4.2 Hardware

4.2.1 Experimental chambers

The experimental chambers for the voltage-clamped cut fiber experiments were identical to the ones described by Brum et al. [1987] for microdomain experiments and by Shirokova et al. [1996a] for nanodomain experiments. The principal of a double vaseline gap chamber for microdomain experiments is shown in Fig. 4.3. It consists of three compartments. Two of them are built as mobile inlays, so that the distance between the inlays can be adjusted. The mounting procedure is as follows: First, the front parts of the inlays that include a 300 µm wide and 300 µm deep slit are covered with vaseline. Then a single muscle fiber is fixed to the bottom of one inlay with a scotch tape and then moderately stretched across the slits and fixed to the bottom of the other inlay. After the vaseline has been put all around the fiber in the area of the slits, an exactly matching cover was pressed on top of each inlay to seal them electrically from the middle pool. Then the electrodes were connected to the pools via agar-bridges and electrical and optical recording could start.

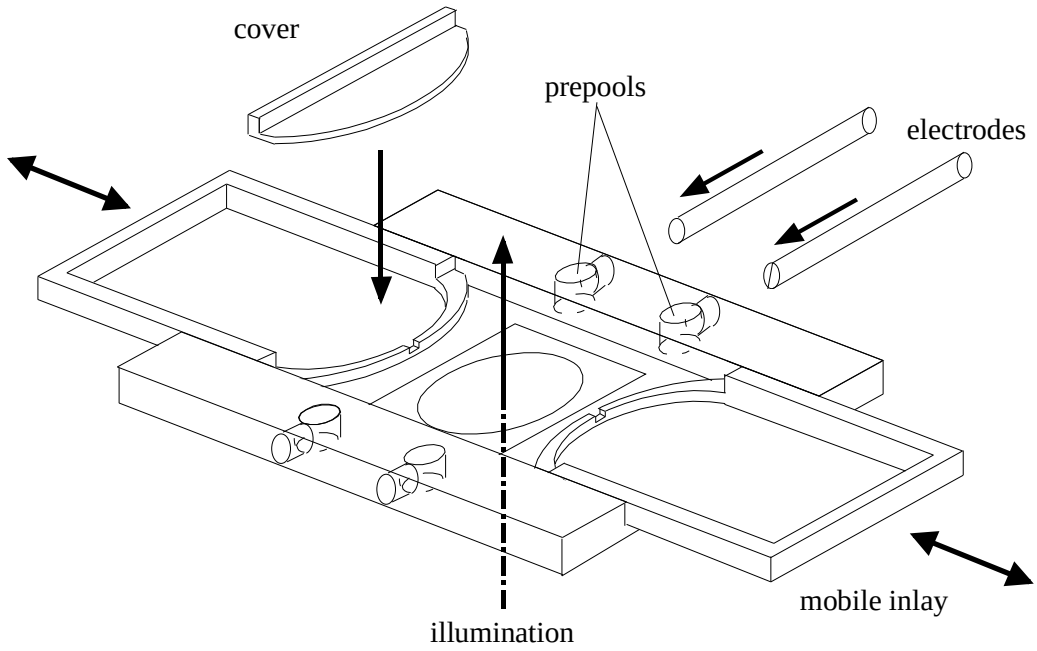

Fig. 4.3 Double vaseline gap chamber for voltage-clamped cut fibers.

The vaseline gap chamber and mounting procedure for nanodomain experiments was very similar, except that the whole chamber was made out of one part and had no bottom. Then a

zero glass cover slip was glued to the bottom side of the chamber. Therefore, in this chamber the fiber was mounted directly on the cover slip. The reason for this was the small working distance (200 µm) of the objective of the corresponding setup.

The chemically skinned fiber chamber consisted of only one pool of about 1mm in diameter. Again the bottom of the chamber was made of a zero glass cover slip and was covered completely with vaseline except for a small region large enough to span about 5 single mouse EDL fibers or 2 frog *tibialis anticus* fibers next to each other across. On both ends the fibers were then fixed to the vaseline covered bottom with scotch tapes.

4.2.2 Microdomain optical setup and data acquisition

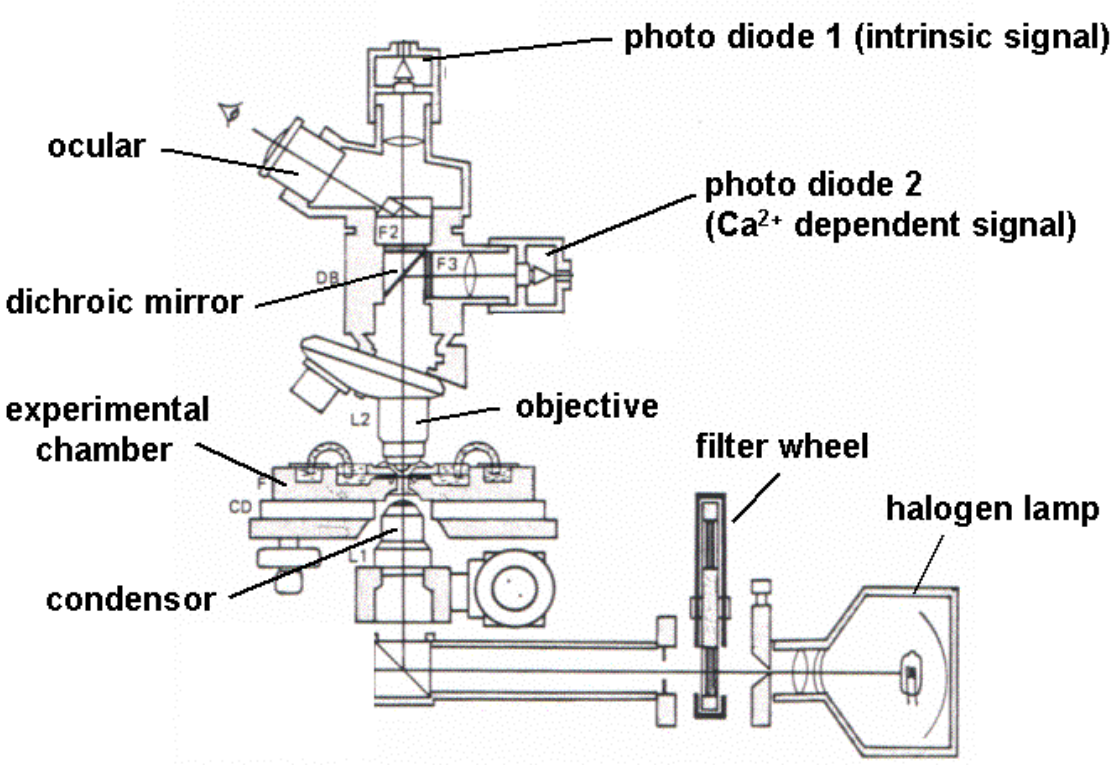

Fig. 4.4 Optical setup for experiments on microdomain Ca^{2+} release with ApIII. Light from a halogen lamp passes through interchangeable interference filters and is then focused by a condensor onto the fiber. The transmitted light is collected with two photo diodes to allow simultaneous recording of Ca^{2+} dependent and Ca^{2+} independent (intrinsic) absorption signals.

The optical setup of the microdomain experiments was basically the same as in Shirokova et al. [1996b] and light intensity could be measured with two photo diodes simultaneously (see Fig. 4.4). It was only used for absorption measurements with Antipyrylazo III (ApIII), although the setup also supported fluorescence measurements. For simplicity only details regarding the absorption measurements are given.

The fiber was epi-illuminated by a standard 100-W tungsten halogen light bulb through a slit of adjustable size and a filter wheel to manually interchange between the desired interference filters (IF). The transmitted light was collected with a 40x, 0.8 NA water-immersion objective (LUM PlanFl, Olympus, Hamburg) mounted on an upright Olympus microscope frame (BHSP, Olympus, Hamburg). All interference filters and dichroic mirrors used were custom made by Omega Optical, Inc. (Brattleboro, VT, USA). There were three configurations used in our experiments. The first was used to measure dye concentration of ApIII as described in Brum et al. [1988b]. Light passed through an IF centered at 550 nm (bandwidth 50 nm) and was then transmitted through the probe or glass capillary before being directly focused on photo diode 1 (no dichroic mirror in the light path). The second configuration used for determination of $[Mg^{2+}]$ was the same as the first, except that the interference filter before the probe was changed to a 600 nm bandpass (bandwidth 100 nm). The third configuration allowed the measurement of Ca^{2+} dependent changes in the absorption of ApIII. Now the filter wheel was turned to insert an IF that passed all wavelengths ?>600 nm into the light path. Then, after passing through the fiber, the light was split at a dichroic mirror and wavelengths of ?<800 nm were collected through a barrier filter centered at 720 nm (bandwidth 10 nm) with photo diode 2 (dye signals related to changes in $[Ca^{2+}]$), while greater wavelengths passed the dichroic mirror and were again collected by photo diode 1 (dye-independent, intrinsic signals).

The voltages of the photo diodes were acquired in ´track-hold mode´. In this mode [Vergara et al., 1978] the difference between the voltage output of the photo diode and an initial value of the same output is amplified, digitized and stored. The voltage from photo diode 2 is fed to the input of a track-and-hold circuit and to the adding input of an instrumentation amplifier (IA) of gain G. The other input of the IA receives the output of the track and hold. At time 0, before application of a step depolarization, the track and hold circuit is signaled to hold, therefore at $t > 0$ only the adding input of IA measures a change in photo diode voltage, therefore the with G amplified signal is proportional to the difference of photo diode voltages before and after the pulse.

Electrical connection to the experimental chamber was achieved by Ag/AgCl-pellets that ended in prepools containing a 3 mM KCl solution. From these prepools agar-bridges connected to the respective solution pool in the double vaseline gab chamber. The four electrodes were attached to a self-built preamplifier that contained the actual voltage-clamp circuit. An electric circuit of the preamplifier is given in the appendix (section 7.2). The recorded electrical signals were then fed into an 8-pole Bessel filter.

All optical and electrical signals were connected to a D/A board (HSDAS) and subsequently to a PC (Pentium 90 MHz) that stored self-written software, that allowed the editing and application of complex voltage pulse protocols as described in [González et al., 1993]. During an experiment, the muscle fiber was usually held at the natural resting potential of -90 mV, from which changes in voltage with rectangular shape in time, so-called step depolarizations, were applied to potentials ranging from -80 mV to +40 mV.

4.2.3 Nanodomain optical setup and data acquisition

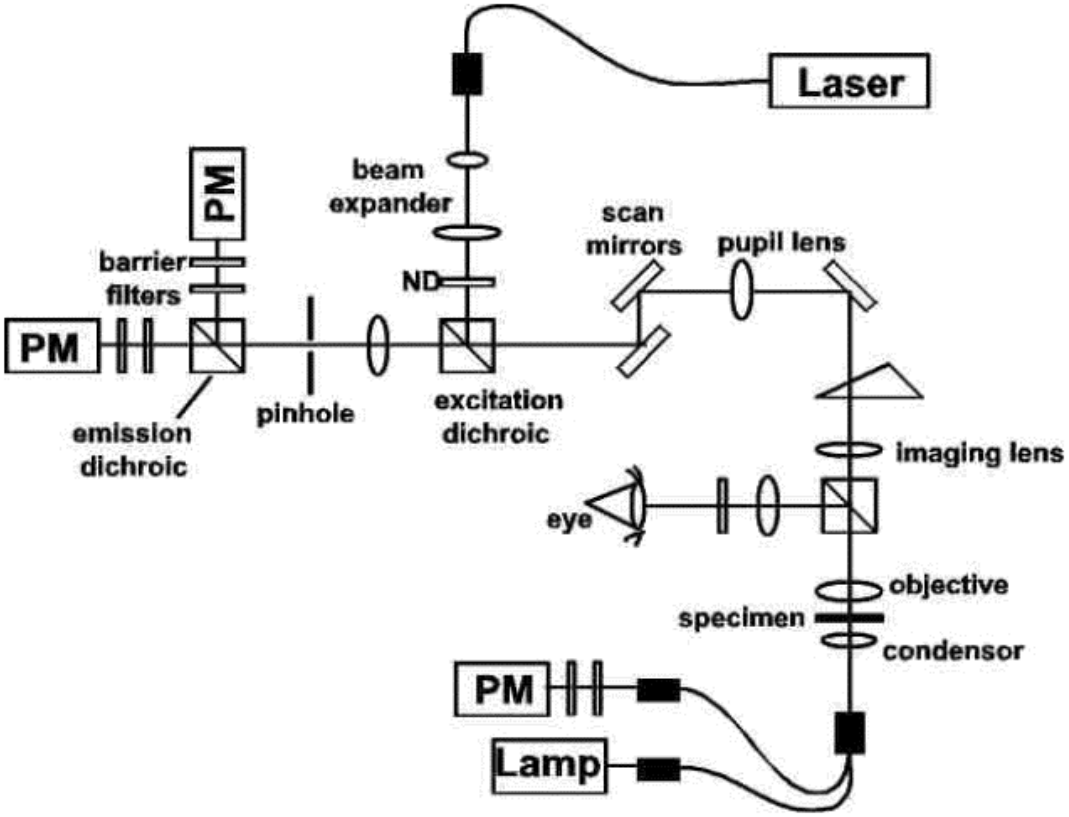

Fig. 4.5 The Olympus optical setup for the measurement of nanodomain Ca^{2+} release from the SR was a confocal laser scanning microscope. Exciting Fluo-4 with an Ar/Kr-ion laser that was coupled via galvanometer driven scan mirrors into an inverted microscope, the spatially resolved fluorescence was simultaneously detected confocally through a pinhole with a photomultiplier.

Two nanodomain setups have been used during the course of this study, the from now on called Olympus setup and Biorad setup. In principal, the two setups were similar in that they both consisted of a laser with a 488 nm line that was coupled through a galvanometer mirror-operated scanhead into an inverted microscope.

The Olympus setup (Fluoview, Olympus, Hamburg, Germany) was used for studies of nanodomain Ca^{2+} release in skinned fibers (see Fig. 4.5). In the used configuration, it utilized the 488 nm line of an Ar/Kr-ion laser (Omnichrome, Melles Griot Inc., CA, USA) that was coupled via fiber optics into the scan head. A neutral density filter set (ND) allowed the decrease to 0%, 1.5%, 6%, 20% or 50% of the incident laser intensity before the laser beam was reflected by the excitation dichroic mirror onto the galvanometer driven scan mirrors. Thereafter the xy-deviated beam was transmitted through a pupil lens into the Olympus $IX70^2$ microscope and through the objective (40x, 1.15 NA, UApo/340) onto the preparation, where Fluo-4 was excited. After taking the same optical path backwards, the emitted fluorescence light passed the excitation dichroic, a 150 µm pinhole and a longpass barrier filter (510 nm) before being collected with a photomultiplier (PM). In general, the Olympus setup has the

possibility to collect fluorescence light with two PMs by inserting of the emission dichroic mirror into the light path. Then, for instance, fluorescence light of two fluorophores can be simultaneously excited, if wanted with both accessible lines of the Ar/Kr-ion laser (488 nm, 568 nm), and separately detected. It was also possible to acquire transmission images, as laser light could be passed through the objective and a differential interference contrast (DIC) optic to a separate PM. A PC (400Mhz/pentiumII) in combination with the Fluoview software was used to control data acquisition.

The Biorad setup (MRC 1000, Biorad, Hercules, CA, USA) was used for the investigation of nanodomain Ca^{2+} release in voltage-clamped cut fibers. In difference to the Olympus setup it consisted of an Ar-ion laser (488 nm, 514 nm), the MRC 1000 scanhead and an inverted Zeiss microscope (Axiovert 100 TV, Zeiss Inc., Oberkochen, Germany) with a 40x, 1.2 NA water-immersion objective. In principal, this setup offered the same possibilities for fluorescence measurements, as it also had a two photomultiplier detection unit and a transmission detection unit including DIC optic. With this setup Fluo-3 was used as a Ca^{2+} indicator. The Biorad setup was synchronized via a TTL signal to work in conjunction with similar electronics and electrical recording circuits as in the microdomain experiments.

4.3 Analysis of microdomain measurements

In this section, first, the equations needed for the quantitative measurement of Ca^{2+} ion and Mg^{2+} ion related signals will be derived. A close look on calibrations for the measurements of $[Mg^{2+}]$ is taken, as they were originally derived during this work and used for the first time in muscle research. Then a method, originally developed by Melzer et al. [1987], for the calculation of microdomain Ca^{2+} release from the SR will be presented.

4.3.1 Determination of $[Mg^{2+}]$

ApIII was used to measure the free Mg^{2+} ion concentration in resting fibers before we applied step depolarisations in voltage-clamped cut fibers. As $[Mg^{2+}]$ is not changing greatly during a calcium transient, the measured $[Mg^{2+}]$ at rest was assumed to be the same as during any applied pulse protocol. $A(\lambda)$, the absorption of the probe containing ApIII, was measured consecutively at the wavelengths 550 nm and 600 nm with the first and second configuration of the microdomain setup. The wavelength of 550 nm was chosen as it corresponds to the isosbestic point of the ApIII absorption spectrum for $[Mg^{2+}]$ binding. At 600 nm the absorption of ApIII shows its greatest decrease for a rise in $[Mg^{2+}]$ compared to other wavelengths (see Fig. 3.2). As $[Ca^{2+}]$ was set to 100 nM in calibrations and resting fibre conditions, we assumed that the ratio of the absorptions *RA*, defined as $RA = A(600)/A(550)$, depended only on $[Mg^{2+}]$ and dye parameters. With p, the optical path length, Dye_t, the total

dye concentration in the ApIII containing volume and the extinction coefficients ε_{Mgdye}, for bound and ε_{dye}, for unbound dye, the maximal and minimal absorption at a certain wavelength is given by

$$A_{\max}(\lambda) = A_{\max,total}(\lambda) - A_f(\lambda) = p \cdot \varepsilon_{dye}(\lambda) \cdot Dye_t, \quad (4.1)$$

$$A_{\min}(\lambda) = A_{\min,total}(\lambda) - A_f(\lambda) = p \cdot \varepsilon_{Mgdye}(\lambda) \cdot Dye_t, \quad (4.2)$$

where the total measured absorption was corrected for the constant intrinsic absorption of the fibre, A_f (not necessary when using glass capillaries). Therefore, in equilibrium, [Mg^{2+}] can be expressed by

$$[Mg^{2+}] = K_{Mgdye} R_{550} \frac{R_{\max} - RA}{RA - R_{\min}}, \quad (4.3)$$

$$\text{where } R_{\max} = \frac{A_{\max}(600)}{A_{\min}(550)}, \quad R_{\min} = \frac{A_{\min}(600)}{A_{\min}(550)} \text{ and } R_{550} = \frac{A_{\max}(550)}{A_{\min}(550)}. \quad (4.4)$$

For our chosen wavelengths R_{550} equals unity, because of the isosbestic point of the ApIII absorption spectrum. The two required absorption measurements to obtain RA (and hence [Mg^{2+}]) in fibers were always executed within 30 seconds at a given time.

4.3.2 Calibration of [Mg^{2+}] measurements

Initial calibrations to determine the binding of ApIII to Mg^{2+} were done in KCl-based solutions. The internal solutions used in release experiments were all based on Cs-glutamate. When measuring [Mg^{2+}] in the internal solutions on the basis of the KCl-based calibration parameters, the resulting [Mg^{2+}] was always lower than the one theoretically predicted by the dissociation constants of the Mg^{2+} buffers in the solution. This could be either due to a difference in the extinction coefficient of ApIII in the compared solutions or due to the additional binding of Mg^{2+} ions to one or more compounds in the internal solution.

First, the differences in the extinction coefficient for the free and bound dye are given, while comparing a KCl-based solution with our internal solution. At 550 nm the extinction coefficients were 2.1±0.2 10^4 $M^{-1}cm^{-1}$ (KCl) and 2.4±0.2 10^4 $M^{-1}cm^{-1}$ (internal) for both free and bound dye. At 600 nm it changed from 1.38±0.2 10^4 $M^{-1}cm^{-1}$ (KCl) to 1.47±0.2 10^4 $M^{-1}cm^{-1}$ (internal) for free dye and from 0.54±0.2 10^4 $M^{-1}cm^{-1}$ (KCl) to 0.94±0.2 10^4 $M^{-1}cm^{-1}$ (internal) for bound dye. This results in a less prominent change of RA with [Mg^{2+}] in the internal solution. This change in the extinction coefficient was mainly due to the presence of ATP, as similar changes were found in the extinction coefficient when ATP was the only solute that was added between different KCl-based solutions. This might be due to the forming of tertiary compounds between ApIII and ATP, but this effect was not studied in more detail.

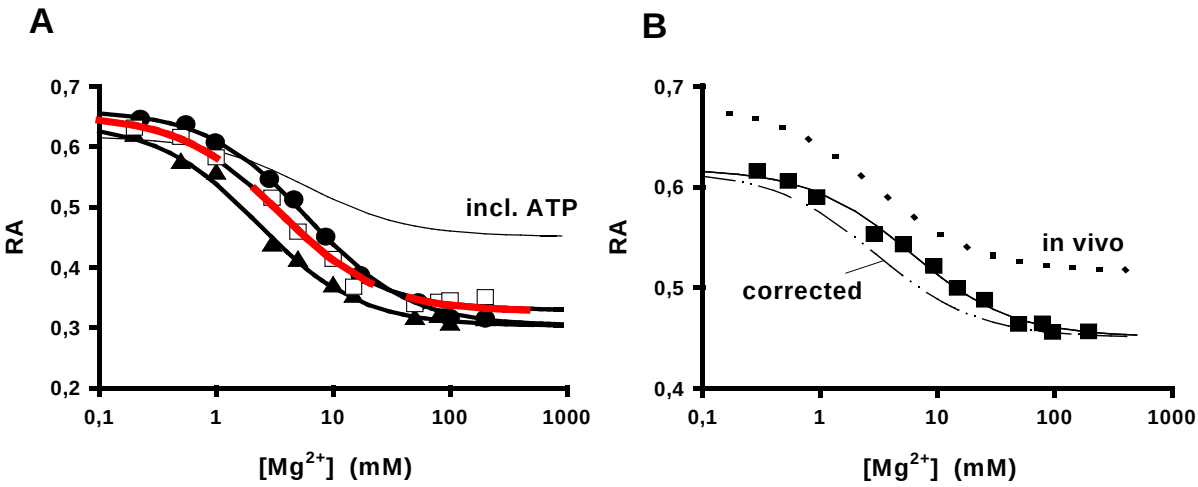

Fig. 4.6 Effects of different solvents on the measurement of $[Mg^{2+}]$ using absorption of ApIII. Solid lines correspond to best fits with eqn. (4.3), dashed traces give the fits assuming binding of Mg^{2+} to glutamate when changing from CsCl to Cs-glutamate based solutions. Calibrations were done in KCl (●), CsCl (▲), Cs-glutamate (□) and internal solutions (■). **A** The solid line tagged 'incl. ATP' is the same as the fit in B for the internal solutions. **B** The dash-dotted trace is calculated from the glass capillary calibration of internal solutions by correcting for glutamate binding and the dotted trace is the in vivo calibration used in experiments with frog fibres.

In addition, the dye changed its absorption properties when glutamate was inserted into the solutions. For the other anions in the internal solutions, like EGTA, ATP or sulfate there exist known dissociation constants for the binding to Mg^{2+} ions. For glutamate no such dissociation constant is reported, hence there exists the possibility that glutamate actually binds to Mg^{2+} ions. This would be an important detail for the correct calculation of $[Mg^{2+}]$ in the solutions for experiments, therefore the effect of glutamate was studied more thoroughly. The results of the measurements of $[Mg^{2+}]$ in different solutions are shown in Fig. 4.6. It is important to note that the value of $[Mg^{2+}]$ to which a certain data point is plotted, is the value obtained by calculating $[Mg^{2+}]$ as if there was no binding by glutamate unless otherwise noted. Panel A shows calibration data for salt solutions based on KCl (●), CsCl (▲) and Cs-glutamate (□) containing 500 µM ApIII. The solid lines give the fit with eqn. 4.3 for these and the complete internal solutions with all solutes (tagged incl. ATP). The parameters for these and all following fits corresponding to the calibrations are given in table 4.3.

The actual data points of the complete internal solution are given in panel B (■), the corresponding fit is again added. A shift of the calibration curve to the right can be seen when changing from CsCl to Cs-glutamate. This shift can be either explained by a change in the dissociation constant of the dye or by a change in $[Mg^{2+}]$ when substituting glutamate for chloride.

In addition similar calibration experiments (data not shown) have been carried out with the fluorescence indicator furaptra and with Mg^{2+} selective electrodes [Kirsch et al., in prep.].

All changes measured with the three different methods can be most easily explained by a dissociation constant of glutamate for Mg^{2+} ions in the range of 100 mM, because it is

relatively uncertain that all three indicators will change their selectivity for Mg^{2+} ions by the same magnitude. In all three methods the data in Cs-glutamate was fitted under the assumption, that glutamate binds Mg^{2+} ions 1:1 and that this is the only change in comparison to CsCl (The only exemption is the data with ApIII, panel A, that was additionally adjusted for some small changes in R_{max} and R_{min}). The fit for ApIII is shown in panel A as the thick dashed line and the obtained dissociation constants for Mg^{2+} ions binding to glutamate were for experiments with ApIII 160±80 mM, with Furaptra 86±20 mM and with Mg^{2+} ion selective electrodes 110±10 mM. The data was fitted well in all cases and the corresponding overall dissociation constant is 106±20 mM, which was used in the calculation of $[Mg^{2+}]$ in the complete internal solutions. Together with the original measurement with ApIII (■) the corrected calibration curve for glass capillaries is shown as the dash-dotted trace in panel B, with a resulting dissociation constant for Mg^{2+} ions binding to ApIII of 3±0.2 mM.

	R_{max}	R_{min}	$K_{DyeMg^{2+}}$
KCl	0.66 ±0.01	0.30 ±0.01	0.17 ±0.01
CsCl	0.64 ±0.01	0.30 ±0.01	0.43 ±0.04
Cs-glutamate	0.65 ±0.01	0.33 ±0.01	0.29 ±0.03
internal	0.62 ±0.01	0.45 ±0.01	0.17 ±0.02
corrected	0.62 ±0.01	0.45 ±0.01	0.33 ±0.02
in vivo	0.68 ±0.02	0.52 ±0.02	0.33 ±0.02

Table 4.3 Fit parameters for calibration data obtained using equation 4.3

Calibration in vivo for binding of ApIII to Mg^{2+} ions

The 0.61 mM and 7.0 mM $[Mg^{2+}]$ containing internal solutions were then applied to several single saponin treated fibres (0.01% for 2 min), slightly pressed between a microscope slide and a coverslip surrounded by thick vaseline. The average values for *RA* were 0.65±0.02 at 0.61 mM Mg and 0.56±0.02 at 9 mM. The value for *RA* at 0.61 mM $[Mg^{2+}]$ exceeds even the value for R_{max} obtained at 0 $[Mg^{2+}]$ (R_{max} = 0.62) in the glass capillary. Because the difference (0.9) between the *RA* values at the two $[Mg^{2+}]$ was the same in fibers and in the glass capillary, the calibration curve obtained in the glass capillary was simply shifted upwards by 0.06 units and used as the calibration curve to interpret fiber results in vivo.

4.3.3 Shift of effective membrane potential

It is expected that an elevated internal $[Mg^{2+}]$ has an effect on the measured membrane potential by screening the negative surface membrane charges [Deutsch et al., 1994]. To investigate this effect the voltage distribution of charge movement of inactivated DHPRs was

studied in voltage-clamped cut fibers. This distribution can be approximated by a single Boltzmann function [Brum et al., 1988a] of the form

$$Q = Q_{\max} \cdot \frac{1}{1 + e^{k(V - V_{0.5})}} . \qquad (4.5)$$

The voltage $V_{0.5}$, where half of the charge is moved by a step polarization, was used to characterize a possible shift in membrane potential.

The inactivation of the DHPRs was achieved by holding the fiber at 0 mV. Experiments were carried out in 0.61 mM [Mg^{2+}] and 5-9 mM [Mg^{2+}]. Only the charges that moved at the turn-off of the step polarization were used for the analysis. The established voltage distribution for each fiber was then fitted with eqn. 4.5 and the fit parameters are given in table 4.4. The average shift of $V_{0.5}$, which corresponds to the shift of the effective membrane potential by high [Mg^{2+}], was -8±0.5 mV. To correct for this shift any potential applied under voltage-clamp was changed by -10 mV when working in high intracellular [Mg^{2+}]. This applied for the holding potential (low [Mg^{2+}]: -90 mV, high [Mg^{2+}]: -100 mV) as well as for depolarizations. From now on only the true membrane potential will be used in referrals to depolarization voltages. For instance, if a trace in a graph is marked with a voltage of -30 mV, which corresponds to the real potential across the membrane, we would have actually applied –40 mV under voltage-clamp in high [Mg^{2+}].

	0.61 mM [Mg^{2+}]			5-9 mM [Mg^{2+}]		
fiber#	Q_{max}	$V_{0.5}$	k	Q_{max}	$V_{0.5}$	k
	[nCµF^{-1}]	[mV]	[mV^{-1}]	[nCµF^{-1}]	[mV]	[mV^{-1}]
1509	34.3	-103.2	0.05	42	-112.5	0.05
1511	33.3	-96.8	0.05	38	-105.8	0.05
1512	33	-101.6	0.05	41	-106.6	0.05
1514	37.9	-97.5	0.05	30	-104.1	0.05
1526	55.8	-94.1	0.07	51	-97.4	0.07
avg.	1	-98.9±0.5	0.053±0.001	1	-106.9±0.5	0.053±0.001

Table 4.4 Fit parameters for several fibers in solutions with 0.61 mM [Mg^{2+}] and 5-9 mM [Mg^{2+}] obtained using equation 4.5.

4.3.4 Diffusion of Mg^{2+} ions

As in voltage-clamped cut fibers a change of the intracellular solution is realized by inserting the solution into the end pools, the time it takes for the solutes to diffuse into the middle section becomes a crucial factor for experiments. Therefore, the time course of the

change in [Mg^{2+}] in microdomain experiments was determined. First of all it was a test, if the measurement of [Mg^{2+}] with ApIII could be carried out in actual experiments with voltage-clamped cut fibers. Second, no calibration for the measurement of [Mg^{2+}] was implemented at the nanodomain experimental setup and therefore it was necessary to know at which time during the experiment the final [Mg^{2+}] was reached.

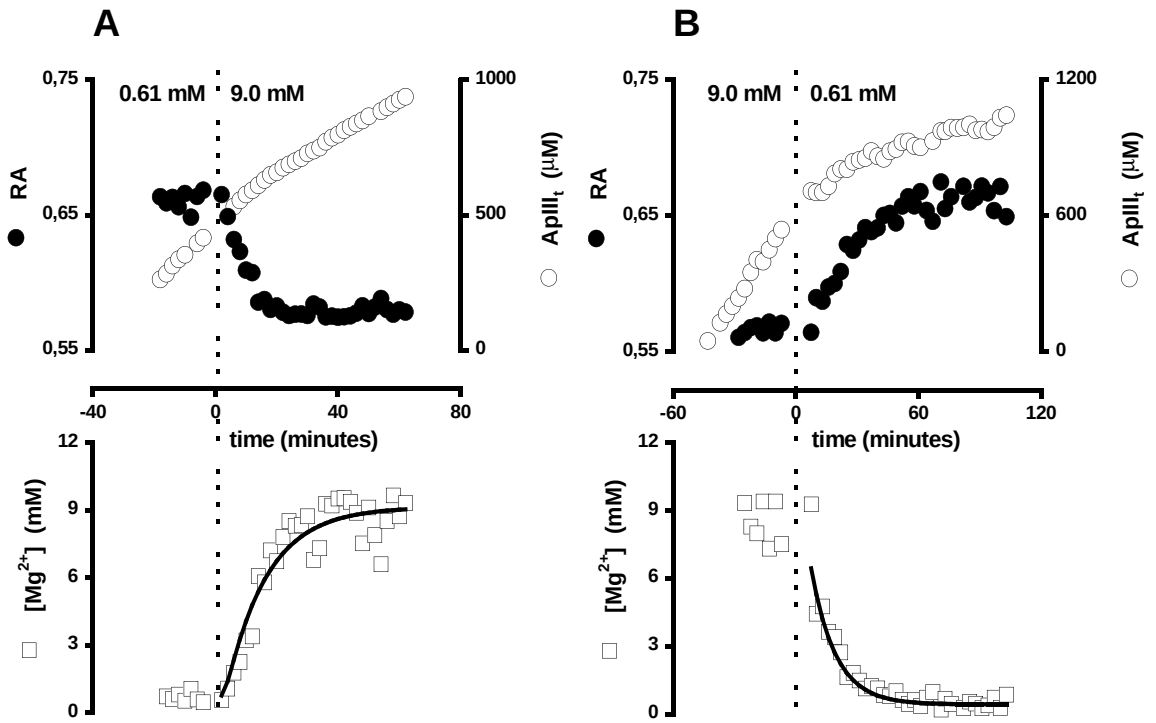

Fig. 4.7 Inward (A) and outward (B) Mg^{2+} ion diffusion in voltage-clamped cut fibers measured with ApIII. Solutions in the end pools were exchanged at t=0 (dashed line) from 0.61 mM to 9 mM [Mg^{2+}] or vice versa. The upper panels show the increase of the total ApIII concentration during the experiment and the change in *RA* after the solution is exchanged, both measured in the middle pool. The lower panels show the corresponding change of [Mg^{2+}], given by eqn. 4.3. The thick line gives the fit of the time course of [Mg^{2+}] with a simple diffusion model using eqn. 4.6. Parameters of the fit and the resulting diffusion coefficients are given in table 4.5. The fiber is equilibrated with the new [Mg^{2+}] as set in the end pools after about 45-60 minutes.

In Fig. 4.7 two experiments are shown where [Mg^{2+}] in the internal solution in the end pools was changed from 0.61 mM to 9.0 mM (A) and vice versa (B). The time axis in every experiment was shifted so that the solution exchange occurred at the vertical dashed line, at t=0. The ApIII concentrations were different in both solutions to allow for dye loading with higher [ApIII] in the end pools in the starting solution and to keep [ApIII] inside the fibre below 1.1 mM during the rest of the experiment, where the fibre interior is equilibrating with the new [Mg^{2+}] from the end pools. As Fig. 4.7 shows, [ApIII] (○) is rising throughout the experiments, however, after the exchange RA (●), the ratio of the absorptions at 600 nm and

550 nm, is relaxing to a new value. The lower panel shows the calculated [Mg^{2+}] (□) inside the fibre using eqn. 4.3 and the in vivo parameters for R_{max}, R_{min} and $K_{DyeMg^{2+}}$ from table 4.3. The time course of [Mg^{2+}] was compared with a model of one-dimensional diffusion in a cylinder by fitting the first 5-11 elements of

$$[Mg^{2+}](t) = s + c \cdot \left\{ 1 - \frac{4}{\pi} \cdot \sum_{n=0}^{\infty} \frac{(-1)^n}{2n+1} \cdot \exp\left(- \frac{(2n+1) \cdot \pi^2 \cdot D_{app} \cdot t}{4 \cdot L^2} \right) \right\}, \qquad (4.6)$$

where s is starting value at t=0 for [Mg^{2+}] , c is the maximum concentration change, L is the diffusion distance (usually 550 µm) and D_{app} is the apparent diffusion coefficient for [Mg^{2+}] (Kovacs et al., 1983). D_{app} was 1.85±0.23 10^{-6} cm^2s^{-1} (n=3) for inward diffusion when the sarcomere length (s.l.) was 2.7 µm to 3.4 µm and 0.81±0.13 10^{-6} cm^2s^{-1} (n=4) when it was greater than 3.4 µm, showing that stretching of the fibre can slow down diffusion. For moderately stretched fibres with s.l. shorter than 3.4 µm the apparent outward diffusion coefficient was 1.71±0.29 10^{-6} cm^2s^{-1} (n=3). Different initial and final [Mg^{2+}] in the end pools were used in the experiments. Parameters of the experiments are summarized in table 4.5. The conclusion from the diffusion measurements in microdomain preparations is that a moderately stretched fibre is equilibrated with [Mg^{2+}] as set in the end pool solutions after about 45-60 minutes.

#	D_{app} (10^{-6} cm^2s^{-1})	c=? [Mg^{2+}] (mM)	s=[Mg^{2+}]$_{t=0}$ (mM)	s.l. (µm)	∅ (µm)
in					
1560	1.53±0.15	8.5±1	0.61	2.7	73
1508	1.69±0.26	1.1±0.1	0.61	3.4	76
1510	2.33±0.29	2.1±0.1	0.61	2.8	60
1584	0.86±0.04	8.3±1	0.61	3.5	70
1585	0.73±0.09	11.7±1.2	0.61	3.9	62
1590	0.68±0.13	8.0±1.5	0.61	3.8	81
1583	0.98±0.24	8.3±1.5	0.61	3.7	71
out					
1530	2.05±0.2	3.9±0.3	4.7±0.3	2.7	99
1596	1.37±0.47	6.5±0.8	7±1	3.4	91
1567	1.72±0.2	9±1	10±1	2.9	86

Table. 4.5 Fit parameters for diffusion experiments according to equation 4.6.

4.3.5 Calibration of [Ca^{2+}] measurements and determination of dye concentration

The determination of the dye concentration and the processing of the absorption records were analogous to the calculations by Brum et al. [1988b] as the same experimental setup was used for experiments. In configuration 3 of the microdomain setup the signals of the two photo diodes were recorded in ´track-hold mode´ [Vergara et al., 1978] (see section 4.2.2). The acquired voltage signals produced by the light focused on the photo diodes can then be expressed as

$$V_k(t) = G_k \cdot \left(V^{PD}{}_k(t) - V^{PD}{}_k(0)\right) \propto I_k(t) - I_k(0), \tag{4.7}$$

where G_k is the gain of the adding instrumentation amplifier, $V^{PD}{}_k$ is the voltage output of the photo diode, I_k is the light intensity and $k = 1,2$ is the index for the number of the photo diode in the microdomain setup (see section 4.2.2). Therefore a change in the absorption of the studied object can be written as

$$\Delta A(t)_k = A_k(t) - A_k(0) = \log\left(\frac{I_k(0)}{\hat{I}(0)}\right) - \log\left(\frac{I_k(t)}{\hat{I}(t)}\right), \tag{4.8}$$

where $\hat{I}$ is the incident light intensity on the muscle fiber and A_k is the absorption of the muscle fiber. Because $\hat{I}$ is assumed not to change during the experiment equation 4.8 can be transformed to

$$\Delta A_k(t) = -\log\left(\frac{V_k(t) \cdot G_k{}^{-1} + V^{PD}{}_k(0)}{V^{PD}{}_k(0)}\right). \tag{4.9}$$

Photo diode 1 measures only changes in the intrinsic absorption of the muscle fiber, as ApIII absorbs light only below 800 nm. Photo diode 2 records changes of intrinsic absorption as well, but in addition also the change of absorption of ApIII due to different free calcium concentrations in the fiber. Hence, it can be written

$$\Delta A_1(t) = \Delta A_f(t), \tag{4.10}$$

$$\Delta A_2(t) = \Delta A_{Ca^{2+}}(t) + \Delta A_f(t). \tag{4.11}$$

The intrinsic absorption change has been shown to depend on wavelength according to the equation [Melzer et al., 1986]

$$\Delta A(t, \lambda_1) = \left(\frac{\lambda_2}{\lambda_1}\right)^{\alpha} \Delta A(t, \lambda_2), \tag{4.12}$$

where the exponent α in this formula was found to be different from fiber to fiber. It can be calculated as

$$\alpha = \frac{\log(\Delta A_2(0)/\Delta A_1(0))}{\log(850/720)} \tag{4.13}$$

at the beginning of an experiment, where no dye has been diffused into the fiber and hence, the photo diode signals depend only on the intrinsic absorptions. The absorption change due to binding of Ca^{2+} ions, $\Delta A_{Ca^{2+}}(t)$, can then be calculated using equations 4.11 and 4.12.

The determination of the total dye concentration inside the fiber at a certain time during the experiment was achieved with measurements by photo diode 1 at 550 nm (configuration 1), which were carried out twice, once with the fiber in the light path to obtain V_{in} and once without to obtain V_{out}. During these measurements the fiber was kept in its resting state, held at -90 mV. This means that the free Ca^{2+} concentration is very low and the absorption corresponds only to the free dye molecules and the intrinsic absorption. Then the total dye concentration can be determined as

$$Dye_t = \frac{\log(V_{out}(t_{\exp})/V_{in}(t_{\exp})) - \log(V_{out}(0)/V_{in}(0))}{0.7 \cdot p \cdot \varepsilon_{550}} = \frac{A_{Dye} - A_f}{0.7 \cdot p \cdot \varepsilon_{550}}, \tag{4.14}$$

where p is the path length (fiber diameter), ε_{550} is the extinction coefficient for the free dye at 550 nm and the factor 0.7 takes into account that only 70% of the fiber volume is accessible to the dye [Baylor et al., 1983]. A_f is measured at the start of an experiment ($t_{\exp} = 0$), where no dye has yet diffused from the end pool into the fiber. The value for ε_{550} was determined during the course of this work to $2.4 \cdot 10^4$ $M^{-1}cm^{-1}$ (see section 4.3.2).

4.3.6 Calculation of Ca^{2+} transients

The determination of the concentration of Ca^{2+} ions bound to ApIII and the following calculation of the time dependent free calcium concentration, the so-called calcium transient, was originally derived by Kovács et al. [1983].

From the Ca^{2+} dependent change in absorption with time the concentration of dye bound to Ca^{2+} ions could be calculated as

$$[Ca(Dye)_2](t) = \frac{\Delta A_{Ca^{2+}}(t)}{0.7 \cdot p \cdot \Delta\varepsilon_{720} \cdot \Delta A_{\max} \cdot 2}, \tag{4.15}$$

where p is the path length (fiber diameter), $\Delta\varepsilon_{720} = \varepsilon_{Ca(Dye)_2} - \varepsilon_{Dye}$ is the difference in extinction coefficients at 720 nm corresponding to the bound and free form of the dye and $\Delta A_{\max}$ is the maximum absorption change (if all dye was bound). The factor 2 is needed, as

ApIII binds in the ratio of 2:1 to Ca^{2+} ions and all calibration parameters were expressed with regard to the dye concentration. The values $\Delta\varepsilon$ =0.1785·10-5 $\mu M^{-1}\mu m^{-1}$ and ΔA_{max} =0.2636 for the actual calculation were taken from [Ríos et al., 1981].

Then, as ApIII is a low affinity dye (see below) the Ca^{2+} transient was calculated by assuming instant equilibrium of the dye with Ca^{2+} ions at all times during the experiment. This assumption was found to be good, as kinetical calculations with on and off rate constants yielded the same results. In equilibrium the Ca^{2+} transient is given by

$$[Ca^{2+}](t) = K_{DyeCa^{2+}} \frac{[Ca(Dye)_2](t)}{(Dye_t - 2\cdot[Ca(Dye)_2](t))^2}, \qquad (4.16)$$

where $K_{DyeCa^{2+}}$ is the dissociation constant of ApIII for Ca^{2+} binding. The value for this dissociation constant was calculated from the temperature of the experiment interpolating linearly between the published values of 25500 μM^2 (at 21°C) and 17500 μM^2 (at 5°C) [Kovács et al., 1983].

4.3.7 Calculation of microdomain Ca^{2+} release

The problem of deriving release flux from Ca^{2+} transients has been solved in both skeletal and heart muscle. The procedure presented in this section follows closely the method discussed by Melzer et al. [1987]. When Ca^{2+} is released, a fraction of it binds to the indicator dye and determines the absorption signal, from which the amount of Ca^{2+} binding to the dye can be derived. The rest of the released Ca^{2+} either remains free or is removed by other buffers in the cell, as there are parvalbumin, troponin, EGTA and the binding sites at the Ca^{2+} pump, which in addition translocates Ca^{2+} ions back into the SR. The rate of Ca^{2+} ions released from the SR can thus be expressed by

$$\frac{dCa^{2+}_{release}}{dt} = \frac{d[Ca^{2+}]}{dt} + \frac{d[Ca(Dye)_2]}{dt} + \sum_i \frac{d[buffer^i Ca^{2+}]}{dt} + \frac{dCa_{pump}}{dt}$$

$$= \frac{d[Ca^{2+}]}{dt} + \frac{d[Ca(Dye)_2]}{dt} + \frac{drem}{dt}, \qquad (4.17)$$

where $[buffer^i Ca^{2+}]$ denotes the concentration of the $buffer^i$ bound to Ca^{2+} ions and dCa_{pump}/dt is the rate at which Ca^{2+} ions are pumped into the SR by the Ca^{2+} pump. As the rate of Ca^{2+} release is related to the source that increases $[Ca^{2+}]$, the rest of the terms, excluding the Ca^{2+} ion binding by the dye, will be referred to as the rate of removal *drem/dt*, as these terms mainly cause a decrease in myoplasmic $[Ca^{2+}]$.

The rates corresponding to the removal system can be written as

$$\frac{d\left[buffer^{i}Ca^{2+}\right]}{dt} = k^{i}{}_{on}\left(buffer_{total}{}^{i} - \left[buffer^{i}Ca^{2+}\right]\right)\cdot\left[Ca^{2+}\right] - k_{off}{}^{i}\left[buffer^{i}Ca^{2+}\right], \qquad (4.18)$$

$$\frac{dCa_{pump}}{dt} = p_{\max}\cdot\left(\frac{\left[pumpCa^{2+}\right]}{pump_{t}}\right)^{2} = p_{\max}\cdot\left(\frac{\left[Ca^{2+}\right]}{\left[Ca^{2+}\right]+K_{p}}\right)^{2}, \qquad (4.19)$$

where $k^{i}{}_{on}$ and $k_{off}{}^{i}$ are the on and off rate constant for the binding of $buffer^{i}$ to Ca^{2+} ions and $buffer_{total}{}^{i}$ is the total concentration of $buffer^{i}$. $p_{\max}$ is the maximum pump rate of the Ca^{2+} pump, which in turn translocates Ca^{2+} ions into SR proportional to the square of the fraction of occupied pump binding sites. The whole term was made proportional to the square of the occupancy of these pump sites to account for the existence of two Ca^{2+} sites per pump molecule [Meissner et al., 1973] that have to be occupied to permit translocation [Inesi G., 1985].

Under voltage-clamp Ca^{2+} transients are elicited by step depolarizations from the holding potential. This method to derive the Ca^{2+} release flux from the SR uses the fact, that upon repolarization after the pulse the release of Ca^{2+} ions under normal physiological conditions is terminated within a few milliseconds [Melzer et al., 1984]. The Ca^{2+} transient can then be expressed by the known rate of change of the complexed dye and by the rate of removal as

$$\frac{dCa^{2+}{}_{release}}{dt} = 0 \quad \Rightarrow \quad \frac{d\left[Ca^{2+}\right]}{dt} = -\frac{d\left[dyeCa^{2+}\right]}{dt} - \sum_{i}\frac{d\left[buffer^{i}Ca^{2+}\right]}{dt} - \frac{dCa_{pump}{}^{2+}}{dt} \qquad (4.20)$$

Therefore, the decay of the Ca^{2+} transient after the pulse, that gives the relaxation of $\left[Ca^{2+}\right]$ to its resting level can be used to determine the properties of the removal system. This is done by varying parameters like rate constants, total intrinsic buffer concentrations or the maximum pump rate to fit the decay of the Ca^{2+} transient after the pulse. The necessary initial values of the underlying buffer concentrations in their free and bound states can be calculated from the $\left[Ca^{2+}\right]$ during the pulse until release has been turned off. Thereafter, it is computed what $\left[Ca^{2+}\right]$ the removal system would produce with the current removal parameters. Then the real Ca^{2+} transient and the predicted can be compared and removal parameters are changed accordingly until both time courses match well. A typical Ca^{2+} transient under voltage-clamp for a medium depolarization voltage (0 mV) is shown in Fig. 4.8 at left. The predicted $\left[Ca^{2+}\right]$ by the removal after release has been turned off is plotted as the thick red trace, which fits well to the real Ca^{2+} transient.

If this procedure is followed with many Ca^{2+} transients at the same time, which correspond to step depolarizations of a great variety of voltages and durations, the resulting removal system that is able to reproduce all the decays within Ca^{2+} transients therefore simulates the underlying processes in the cell correctly, at least for the range of studied pulse voltages and

durations. This is not to say that the parameters of the in this way established removal system have true values and that this would be a method to ´measure´ any underlying rate constant. Complex as the presented model is, it still does not include all known aspects of transport and binding within a muscle cell.

However, the established removal system allows to calculate the rate of removal at any time during the Ca^{2+} transients in the studied experiments. Thus, the rate of Ca^{2+} release flux from the SR can now be calculated with equation 4.17 by adding the terms of the differentiated Ca^{2+} transient, the differentiated time course of the concentration of the complexed dye and the rate of removal of Ca^{2+} ions from the myoplasm using the parameters of the fitted removal system in conjunction with the known Ca^{2+} transient. An example for a resulting time course of Ca^{2+} release is shown in Fig. 4.8. It was calculated from the Ca^{2+} transient at left.

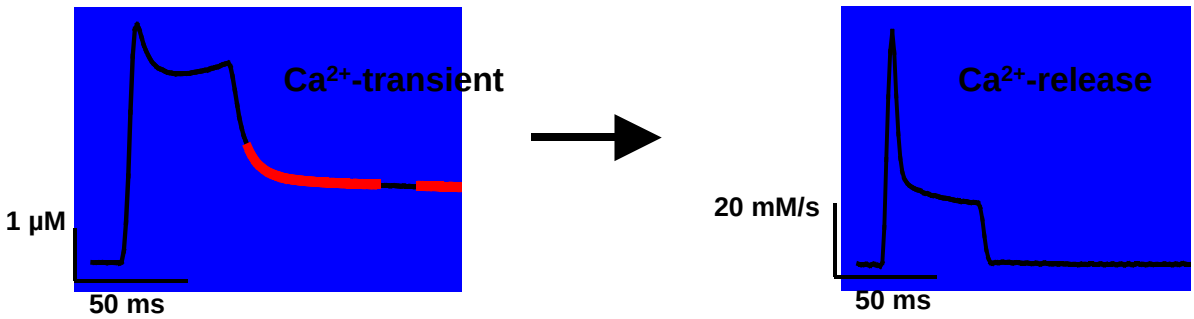

Fig. 4.8 Calculation of microdomain Ca^{2+} release is determined by fitting the removal system to the decay of the measured Ca^{2+} transients. Left: Ca^{2+} transient elicited by a step depolarization from -90 mV to 0 mV for 50 ms. The thick red line corresponds to $[Ca^{2+}]$ predicted from the fitted parameters in the removal system. Right: The resulting time course of Ca^{2+} release from the SR, which is given by equation 4.17.

The microdomain removal system included the following variable parameters: The concentration and rate constants for Ca^{2+} binding sites on troponin [Potter et al., 1975], the concentration of parvalbumin and the rate constants for related binding sites that can bind both Ca^{2+} and Mg^{2+} ions [Gerday et al., 1976] the rate constants of Ca^{2+} binding to EGTA, the concentration of the binding sites at the Ca^{2+} pump, [pump sites], together with their dissociation constant, K_{pump}, and the maximum pump rate. The binding of parvalbumin to Mg^{2+} ions was calculated similar to equation 4.18, except that $\left[Mg^{2+}\right]$ is substituted for $\left[Ca^{2+}\right]$. The values for $\left[Mg^{2+}\right]$ were taken from the calculated internal solutions. During the calculations $\left[Mg^{2+}\right]$ was assumed to stay constant as it is present in muscle cells in about 1 mM concentration.

The actual calculation of Ca^{2+} release flux from the SR was based on a FORTRAN program developed by the lab of Dr. E Ríos (Rush University, Chicago, USA), which during the course of this work was changed to correct for the binding of Mg^{2+} ions to ApIII according to equation 3.14.

This program works in two steps as described by Brum et al. [1988b]: First, from the beginning of the step depolarization until 14 ms after its end the equations 4.18 and 4.19 are solved numerically by Eulers method for each buffer using the measured Ca^{2+} transient as the driving concentration for the reactions (For more information about the Euler method see also section 4.4.6.). This yields the occupancy of all binding sites at 14 ms after the end of the pulse. Second, starting at 14 ms after the pulse the equations 4.18 and 4.19 were used to generate the time course of $[Ca^{2+}]$. The other purpose of the computations was to find ´best fit´ values of the parameters. The method, as described in previous work [Melzer et al., 1986a], started with linearization of the equations in the neighborhood of an initial set of values of the parameters. The partial derivatives of the predicted $[Ca^{2+}]$ with respect to each parameter, required by the linearization procedure, were calculated by imposing a small increment on the corresponding parameter. Then a set of correction terms was determined to make the sum of square deviations of the predicted $[Ca^{2+}]$ minimum. The procedure was iterated from the corrected values until no further improvement of the fit was found. The whole fitting process was carried out simultaneously on several Ca^{2+} transients, generated with pulses of different amplitudes and durations, at different times during the experiment.

The parameter values for the removal system are different from fiber to fiber. In the course of fitting the removal system mainly three parameters were altered: the two rate constants for binding of EGTA to Ca^{2+} ions and the maximum pump rate. The value for the fitted parameters will be given with the certain experiment in the results chapter.

4.4 Analysis of nanodomain measurements

This section describes in detail how the line scanning images that contain the nanodomain fluorescence signals were processed. It will be explained how the detected fluorescence events were parameterized to describe their morphology. It presents a method to derive the Ca^{2+} release flux from the SR that determines the increase in the myoplasmic free calcium concentration as a function of space and time, which follows a procedure described in detail by Ríos et al. [1999].

All processing of the digital image analysis of the nanodomain fluorescence data has been carried out with the software Interactive Data Language (IDL, Research systems Inc., USA). The software IDL provides an environment to compute multidimensional arrays with script language programs, including a multitude of standard digital imaging analysis subroutines.

The IDL source code of two programs written with IDL is given in the appendix. The program FLASH was written for the calculation of morphological spark parameters in permeabilized fibers and is described in section 4.4.2 and 4.4.3. The program RELEASE calculates the spatially and temporally resolved Ca^{2+} release flux from the SR from averaged

fluorescence arrays containing Ca^{2+} sparks. It was originally written by Dr. E. Ríos (Rush University, Chicago, USA) and was modified in the context of this work.

4.4.1 Calibration and determination of dye concentrations

When the dye concentration is low the total fluorescence can generally be expressed as

$$F = MB_{\min}([Dye] + q[DyeCa^{2+}]), \tag{4.21}$$

where M is the adjustable gain of the scanner, $B_{\min}$ is a calibration constant, $[Dye]$ and $[DyeCa^{2+}]$ are the concentrations of free and bound dye, q is the ratio between the fluorescence of dye bound to Ca^{2+} ions and free dye. The minimal and maximal fluorescence is then given by

$$F_{\min} = MB_{\min} Dye_t, \tag{4.22}$$

$$F_{\max} = qF_{\min}, \tag{4.23}$$

with Dye_t being the total concentration of dye given by

$$Dye_t = [Dye] + [DyeCa^{2+}]. \tag{4.24}$$

If the dye is in equilibrium with Ca^{2+} ions, then with

$$K_{DyeCa^{2+}} = \frac{[Ca^{2+}] \cdot [Dye]}{[DyeCa^{2+}]}, \tag{4.25}$$

it follows that

$$F = MB_{\min} \frac{K_{DyeCa^{2+}} + q[Ca^{2+}]}{K_{DyeCa^{2+}} + [Ca^{2+}]} Dye_t = F_{\min} \cdot \frac{K_{DyeCa^{2+}} + q[Ca^{2+}]}{K_{DyeCa^{2+}} + [Ca^{2+}]}, \tag{4.26}$$

where $K_{DyeCa^{2+}}$ is the dissociation constant governing Ca^{2+} binding of the dye. Applying this equation to the resting condition, where $F = F_0$, it follows that

$$F_0 = F_{\min} \cdot \frac{K_{DyeCa^{2+}} + q[Ca^{2+}]_0}{K_{DyeCa^{2+}} + [Ca^{2+}]_0}, \tag{4.27}$$

where $[Ca^{2+}]_0$ is the free calcium concentration at rest, which corresponds to the over the whole cytoplasm averaged intracellular calcium concentration of a cell in its nonexcited state, where no additional calcium is released by external triggers. In that state $[Ca^{2+}]$ is basically equivalent to the value set by the EGTA buffered internal solution. In the used experimental

solutions $\left[Ca^{2+}\right]_0$ is set to 100 nM and thus it is 10 fold lower than the dissociation constant of Fluo-3 inside the myoplasm (~1 µM [Harkins et al., 1993]). This simplifies equation 4.27 to

$$F_0 = F_{\min} \cdot \frac{K_{DyeCa^{2+}} + q\left[Ca^{2+}\right]_0}{K_{DyeCa^{2+}}} = c \cdot F_{\min} . \tag{4.28}$$

For the determination of the dye concentration in the Biorad setup, the following formula was used, which was determined by Dr. Shirokova (Rush University, Chicago, USA):

$$Dye_t = \frac{K_{DyeCa^{2+}} \cdot F_0(x)}{l \cdot k_{\max} \cdot \left[Ca^{2+}\right]_0} \cdot e^{-([gain-1000]\cdot 0.011)}, \tag{4.29}$$

where *l* is the laser intensity, *gain* is the value of the gain in the Biorad software and $k_{\max}$ is a factor that contains $B_{\min}$.

In the Olympus setup the dye concentration inside skinned fibers was assumed to be 60 µM, which is the same as in the solution outside the fiber. This is a low estimate and if this assumption is in error, the resulting calculated Ca^{2+} release would be less than in reality.

4.4.2 Line scanning

Due to the brief nature of nanodomain Ca^{2+} release events (down to 4-6 ms in duration), the confocal laser scanning microscopy was carried out in line scanning mode to enhance the time resolution (2 ms per line). In all experiments presented in this work the orientation of the scan line was along the fiber axis, thereby scanning over tens of sarcomeres. The scan line is always considered to be aligned with the x-axis, when referring to a coordinate system within the muscle fiber.

The orientation of the scan line in a muscle fiber loaded with Fluo-3 is shown in Fig 2.7. From this xy-scan of fluorescence of the fiber at left it becomes clear, that the Ca^{2+} indicator Fluo-3 inside the cell produces a periodic pattern of fluorescence. This pattern is coaligned with the sarcomeric structure of the muscle fiber, in that the high intensities are usually located in the middle of the sarcomere [Klein et al., 1996; Shirokova et al., 1997]. This pattern is thought to be either due to protein-specific binding of Fluo-3 within the cell or to specific areas that are easier to access for the dye [Tsugorka et al., 1995]. Whatever the origin may be, in interpretations of the fluorescence signals the locations with higher intensity in this pattern are assumed to reflect a respective higher dye concentration.

This pattern is also always imaged by the line scan as shown in Fig 4.9 left and Fig 4.10 A. The fluorescence image at left in Fig.4.9 was obtained by the Biorad setup and corresponds to a frog muscle fiber under voltage-clamp. The applied step depolarization from -90 mV to -55 mV for 400 ms elicited spatially discrete Ca^{2+} signals. The image in Fig. 4.10 A was acquired in a permeabilized frog muscle fiber with the Olympus setup. Here the Ca^{2+} sparks

occur spontaneously throughout the image. In both cases, the elevations in fluorescence corresponding to the Ca^{2+} sparks are superimposed on the periodic pattern.

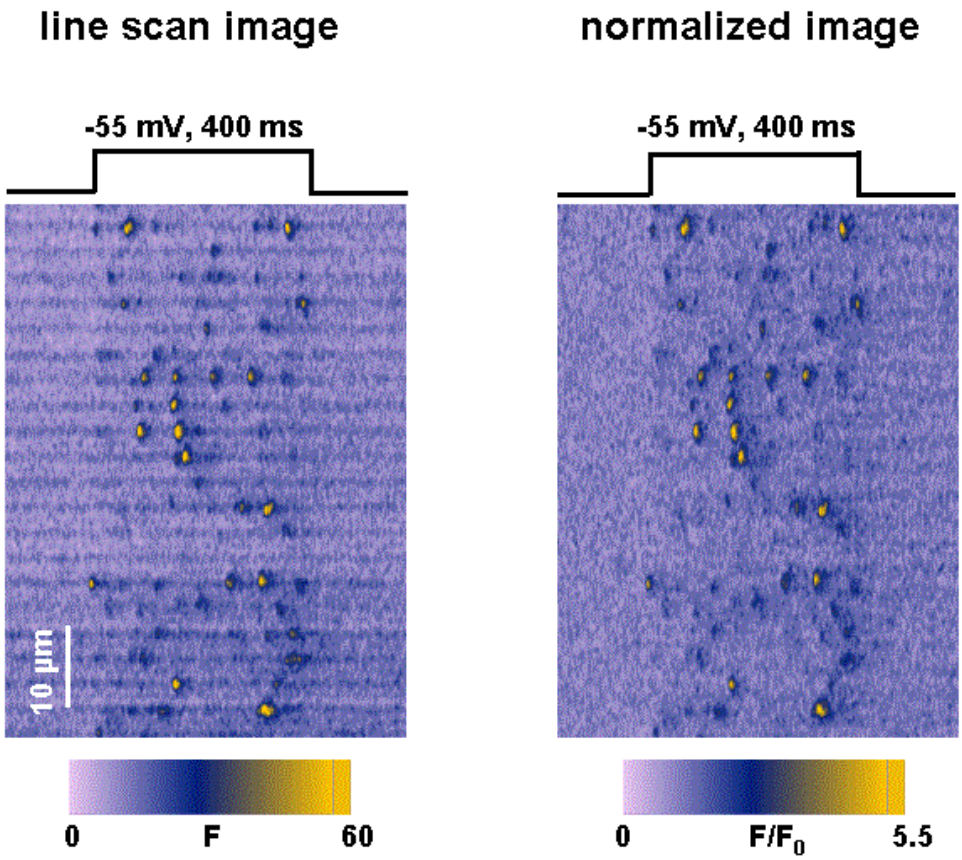

Fig. 4.9 Left: Line scan image from a voltage-clamped cut skeletal muscle fiber, obtained with the Biorad setup. Ca^{2+} sparks occur during the applied step depolarization from –90 mV to –55 mV for 400 ms. Right: Corresponding image of normalized fluorescence $F(x,t)/F_0(x)$. The periodic pattern within the line scan is removed.

The line scan images are arrays of fluorescence intensities $F(x,t)$. For further analysis, the images acquired under voltage-clamp were normalized to the averaged resting fluorescence $F_0(x)$ before the pulse, which removes the periodic pattern from the image as shown in Fig 4.9. The total dye concentration $Dye_t(x)$ was then calculated from the thus obtained $F_0(x)$, using eqn. 4.29.

The images in permeabilized fibers were treated differently, as there is no general location within the image, where sparks can be predicted to occur. Rather, every Ca^{2+} spark was analyzed separately, a procedure that will be described in section 4.4.3

4.4.3 Measurement of Ca^{2+} spark morphology

The shape and size of Ca^{2+} sparks is characterized in images or image areas of normalized fluorescence $F(x,t)/F_0(x)$. For voltage-clamped cut frog fibers, where Ca^{2+} sparks are elicited during voltage pulses, Ca^{2+} sparks were analyzed with an automatic detection

program that is able of characterizing thousands of events in a reasonable analysis time [Cheng et al., 1999; González et al. (Kirsch), 2000b]. This could only be achieved, because the fluorescence events in adult amphibian muscle have a very stereotyped shape. On the basis of mammalian Ca^{2+} release events, which were for the first time measured in abundance in this study, where the events exhibit a greater variety of spatio-temporal shapes, a new program had to be developed that will be described in this section. The image processing routines are, in principal, analogous to the ones used for voltage-clamp experiments. The difference is that an automatic detection was not incorporated due to the non-stereotyped morphology and the spontaneous character of spark generation that led to arbitrary locations of release events within the image. All Ca^{2+} release events in amphibian and mammalian muscle fibers obtained with the Olympus setup were analyzed with this new program.

Ca^{2+} release events were detected by eye. Then an image area before the event was selected via cursor and the fluorescence within this area was averaged with respect to time to yield $F^{area}{}_0(x)$. Part of the image, given by the width of the selected area, was then normalized to $F^{area}{}_0(x)$. Pixels within the normalized image part that were greater than three times the standard deviation of $F^{area}{}_0(x)$ were then temporally displayed with zero intensity to give a visual confirmation that the event was not due to noise.

After this confirmation, two areas were selected in the original, non-normalized image via cursor, one before and one after the event. The image area in between, which contains the event, was then normalized to the averaged baseline fluorescence from the two selected areas, computed as an average weighed by the size of the two selected areas. The three areas were then circumvented with lines to mark the object as shown in Fig. 4.10 A.

All further analysis was done in the normalized spark containing image area, which was displayed in another window (Fig. 4.10 B.). Four morphological parameters were determined: Amplitude [F/F_0], full width at half maximum (FWHM) [µm], full duration at half maximum (FDHM) [ms] and rise time [ms]. The amplitude was obtained as the maximum intensity value within the image area after a filtering procedure, which averaged three pixels in spatial direction only. The other three parameters were determined in the unfiltered normalized image area. The FWHM was the number of pixels with half maximum intensity, which were counted in the one-dimensional array through the maximum in x direction, times the x-resolution of the image. The FDHM was computed analogous to the FWHM, except that pixels were counted in t direction and multiplied by the time resolution. The rise time was calculated as the number of pixels before the event greater than 10% of the maximum, starting at the maximum and counting backward in time in the one-dimensional array through the maximum until a pixel missed the criterion. These parameters and the position of the maximum in the original image of all events analyzed as above were saved in a file. In addition, with the size being determined by the size of the image area, the complete one-dimensional array through the maximum in t and x direction was displayed as a normal xy-graph in separate windows as shown in Fig 4.10 C and D. The source for the array in

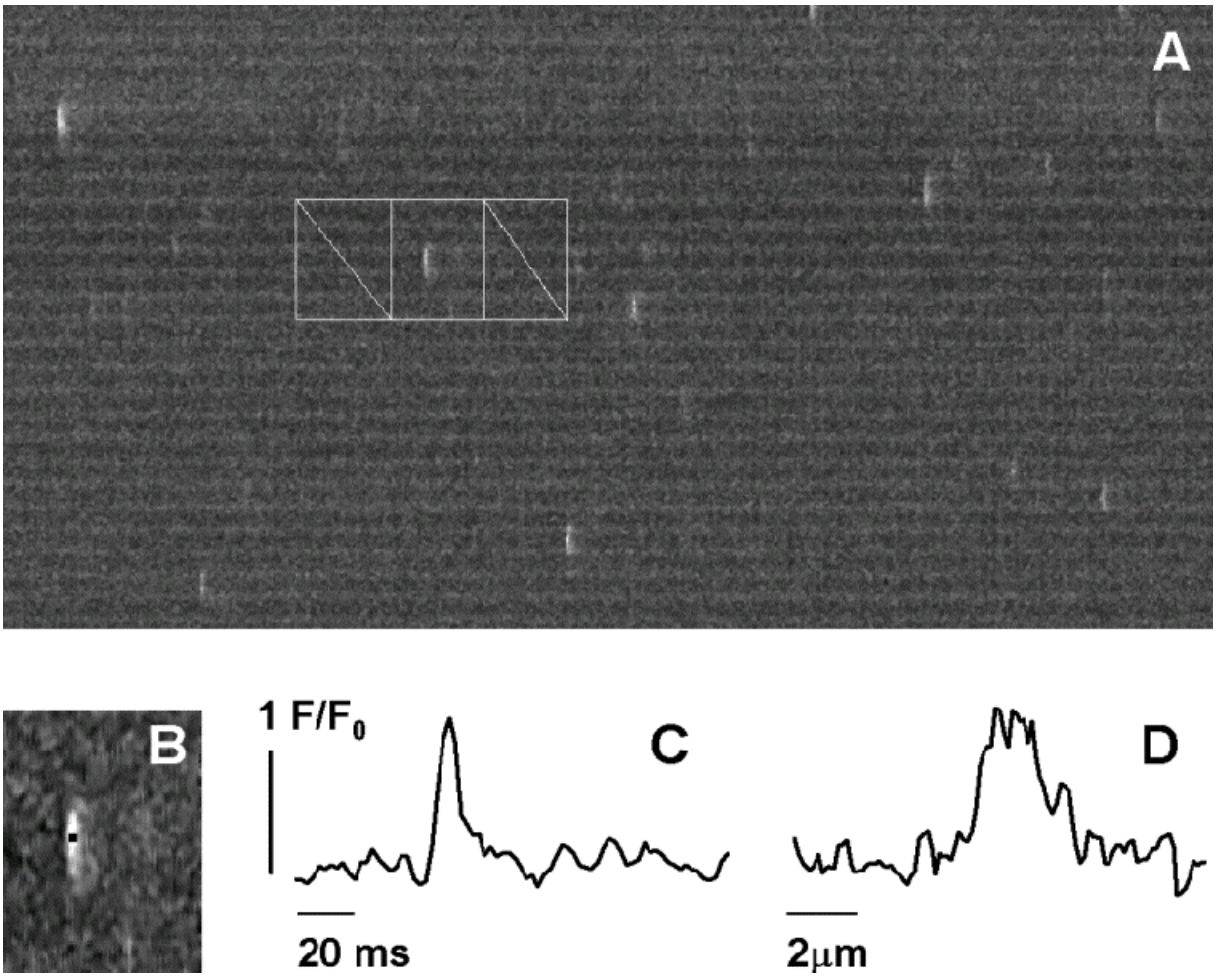

Fig. 4.10 **A** Example of a line scan image (512 x 1000 pixel corresponding to 69.888 μm x 2 s) from an amphibian skinned muscle fiber. The periodic pattern results from the sarcomeric structure. Short discrete release events originating at triads can be seen. Sparks were individually analyzed. The fluorescence F(x,t) prior and after the spark was averaged to obtain a function of baseline fluorescence $F_0(x)$, which was used to normalize the image area that contains the spark. Then the magnitude and the position of the spark is determined. Only sparks with amplitudes exceeding 1.5 F/F_0 were analyzed. **B** The maximum of the spark in the normalized image is marked by a black 3x3 mask. All morphological parameters of the sparks (amplitude [F/F_0], full width at half maximum (FWHM) [um], rise time [ms] and full duration at half maximum (FDHM) [ms] were determined within this image area. **C** Time course of fluorescence through the maximum of the spark. **D** Spatial profile of spark through its maximum.

t direction was the image area filtered by 3 spatial pixels, but it was the non-filtered image area for the array in x direction. These arrays will from now on be referred to as time course and spatial profile of the event, respectively, and if desired they were saved in separate files.

After the computing, the maximum of the current event was marked with zero intensity in the image area as well as in the original image to ensure that no spark was measured twice in an image. In all data presented later in this work, the Ca^{2+} release events taken for further analysis had at least an amplitude of 1.5 F/F_0, this was set as an additional selection criterion and was mainly due to noise that made a reasonable determination of the morphological parameters impossible. This does not mean that there were no events with a lower amplitude.

As just described, the morphological spark parameters were assessed for each event individually. For the calculation of the underlying changes in the free calcium concentration and further of the spatially resolved Ca^{2+} release individual events were too noisy. Therefore, this more sophisticated analysis was only performed on averages of at least 100 events. To obtain averages of Ca^{2+} sparks, the individual events were superimposed at their maximum. This was done in a standard size image array (45x45 pixels or 60x60 pixels), which was cut out of the original image of absolute fluorescence. This averaging procedure is only meaningful when the selected events have a quite similar shape. The averaging of the baseline fluorescence F_0 needed for the release calculation was accomplished by averaging the 45 or 60 pixel wide parts of the baseline fluorescence of the corresponding image, centered around the x-position where the selected sparks occurred.

4.4.4 Deblurring

The fluorescence signals corresponding to Ca^{2+} sparks have been imaged with confocal laser scanning microscopy. Therefore the fluorescence distribution in time and space within the object has been convoluted with the PSF of the microscope. This convolution can in general be written as [Agard et al., 1989]

$$F(X,Y,Z) = \iiint f(x,y,z) \cdot PSF(x-X, y-Y, z-Z) \cdot dx \cdot dy \cdot dz \,, \tag{4.30}$$

where $F(X,Y,Z)$ is the resulting blurred fluorescence signal, $f(x,y,z)$ is the original fluorescence object and PSF denotes the point spread function of the microscope.

In order to calculate the Ca^{2+} release from the SR underlying Ca^{2+} sparks, the fluorescence images first have to be deconvoluted. The deblurring procedure used for the data presented in this work was similar to the one described in Ríos et al. [1999].

One simplification of eqn. 4.30 can be made as fluorescence intensities have only been studied in line scanning mode. If the orientation of the line scan corresponds to the x-axis, then *F* only has to be evaluated at *Y*=0 and *Z*=0. This yields

$$F(X) = F(X,0,0) = \iiint f(x,y,z) \cdot PSF(x-X, y, z) \cdot dx \cdot dy \cdot dz \,. \tag{4.31}$$

Now several assumptions are made to simplify the problem. First, the object fluorescence signal *f* is symmetric with respect to all spatial coordinates. That implies that *f* is separable into the independent symmetric functions $g_1(x)$, $g_2(y)$ and $g_3(z)$, hence, it can be written as

$$f(x,y,z) = f(0) \cdot g_1(x) \cdot g_2(y) \cdot g_3(z) \,. \tag{4.32}$$

The next assumption is that the PSF can be reproduced by the product of two gaussian functions, which is a good approximation for the two confocal setups used to measure nanodomain Ca^{2+} release [Ríos et al., 1999; Feierabend M., 1999]. The PSF is then given by

$$PSF = G(x, y)H(z), \tag{4.33}$$

with

$$G(x, y) = \frac{1}{2\pi\sigma_{xy}^{\ 2}} \exp\left[-\frac{(x^2 + y^2)}{2\sigma_{xy}^{\ 2}}\right] \tag{4.34}$$

and

$$H(z) = \frac{1}{2\pi\sigma_{z}^{\ 2}} \exp\left[-\frac{z^2}{2\sigma_{z}^{\ 2}}\right]. \tag{4.35}$$

Equation 4.31 can then be expressed as

$$F(X) = f(0) \cdot \int g_1(x) \cdot G(x - X) \cdot dx \int g_2(y) \cdot G(y) \cdot dy \int g_3(z) \cdot H(z) \cdot dz, \tag{4.36}$$

where $G(x - X) \equiv G(x - X, 0)$ and $G(y) \equiv G(0, y)$.

For further simplification the integrals over y and z can now be defined as

$$J = \int g_2(y) \cdot G(y) \cdot dy \tag{4.37}$$

and

$$L = \int g_3(z) \cdot H(z) \cdot dz. \tag{4.38}$$

Accordingly it follows that

$$F(X) = f(0) \cdot J \cdot L \cdot \int g_1(x) \cdot G(x - X) \cdot dx \tag{4.39}$$

With this equation it is possible to obtain $g_1(x)$ from the given fluorescence signal $F(x)$ via Fourier transformation. The Fourier transform of this equation can be written as

$$\tilde{F}(Y) = \frac{1}{\sqrt{2\pi}} \int F(X) \cdot e^{iYX} \cdot dX = \varepsilon \cdot \frac{1}{\sqrt{2\pi}} \int \left(\int g_1(x) \cdot G(x - X) \cdot dx \right) \cdot e^{iYX} \cdot dX, \tag{4.40}$$

where $\varepsilon = f(0) \cdot J \cdot L$.

The convolution theorem states that the Fourier transform of a convolution (consisting of two functions) can be expressed as the product of the separate Fourier transforms of the two convolved functions times $\sqrt{2\pi}$. Therefore, this equation can be written as

$$\tilde{F}(Y) = \varepsilon \cdot \sqrt{2\pi} \cdot \tilde{g}_1(Y) \cdot \tilde{G}(Y), \tag{4.41}$$

Thus, the object fluorescence signal can be expressed by back transformation as

$$g_1(x) = \frac{1}{\sqrt{2\pi}} \cdot \int \tilde{g}_1(Y) \cdot e^{-ixY} \cdot dY = \frac{1}{2\pi \cdot \varepsilon} \cdot \int \frac{\tilde{F}(Y)}{\tilde{G}(Y)} \cdot e^{-ixY} \cdot dY. \tag{4.42}$$

As g_1 has to be scaled, so that $g_1(0)=1$, the prefactors need not to be considered within Fourier transforms. Finally, evaluating eqn. 4.39 at $x=0$ yields

$$f(x,0,0) = f(0)\cdot g_1(x) = \frac{F(0)}{J^2 L}\cdot g_1(x). \tag{4.43}$$

This is the desired deblurred fluorescence signal for a given time.

In the numeric deblurring algorithm the Fourier transform in discrete space is realized by the FFT-function. The Fourier transformations are carried out for every time t_j in the numerical array. The deblurring algorithm is a part of the IDL program RELEASE given in the appendix (see 7.1.2).

4.4.5 Calculation of the spatially and temporally resolved [Ca^{2+}]

The analysis for microdomain Ca^{2+} signals, which is applicable to spatially homogeneous changes of $[Ca^{2+}]$ in time, has to be expanded to include time and spatial coordinates. Thus, in addition to changes in concentration by the law of mass action, diffusion has to be included in the calculation of spatially resolved $[Ca^{2+}]$ to account for the relaxation of concentration gradients across the spatial coordinate.

The diffusion equation in three space dimensions and time can generally be written as

$$\frac{\partial c(\vec{x},t)}{\partial t} = \text{div}\,(D\ \text{grad}\ c(\vec{x},t)), \tag{4.44}$$

where $c(\vec{x},t)$ resembles the concentration. For isotropic and concentration independent diffusion, which is assumed to take place in the experiments considered, D is a scalar and called diffusion coefficient. Then eqn. 4.44 can be written as

$$\frac{\partial c(\vec{x},t)}{\partial t} = D\Delta c(\vec{x},t), \tag{4.45}$$

where Δ is the Laplace operator.

Again the simplification applies that nanodomain Ca^{2+} release is only measured in line scanning mode. Thus, only one spatial coordinate has to be included in the description. This results in the problem to find an approximation of the Laplace operator that differentiates only with respect to the x coordinate, but that still includes the contributions of diffusion in perpendicular directions. Under the assumption that the fluorescence increase is spherically symmetric, a function of time and the distance to its center, the dependence of the fluorescence with x gives all the information needed to calculate the Laplacian correctly [Ríos et al., 1999] as

$$\Delta = \frac{\partial}{\partial x^2} + \frac{2}{x}\cdot\frac{\partial}{\partial x}. \tag{4.46}$$

This is a very general assumption and in skeletal muscle it is based on two observations: First, the morphological parameters (amplitude, FWHM, FDHM) of Ca^{2+} sparks in amphibian skeletal muscle show no significant change when the orientation of the line scan is varied (unpublished data from the lab of E. Ríos). Second, the vast majority of fluorescence signals corresponding to Ca^{2+} sparks have a circular shape, when they are measured with a high speed confocal microscope in xy-scan mode [Brum et al., 2000, submitted].

In order to derive $[Ca^{2+}]$ from the fluorescence signal, the first step is to determine the concentration of dye bound to Ca^{2+} ions. In general, the total fluorescence of a dye in equilibrium with Ca^{2+} ions can be written as

$$F = MB_{\min}\frac{K_{DyeCa^{2+}} + q[Ca^{2+}]}{K_{DyeCa^{2+}} + [Ca^{2+}]}Dye_t, \tag{4.26}$$

where $K_{DyeCa^{2+}}$ is the dissociation constant governing Ca^{2+} binding and Dye_t is the total concentration of dye. With the knowledge of the total dye concentration, which either has to be assumed or is calculated from calibrations (see section 4.4.1), the expression for the total fluorescence can be further transformed using equations 4.22-26 and the free calcium concentration can be expressed as

$$[Ca^{2+}] = K_{DyeCa^{2+}}\frac{F - F_{\min}}{F_{\max} - F}, \tag{4.47}$$

wherefrom the concentration of dye bound to Ca^{2+} ions can be obtained, which is now given in dependence of x and t, as the considerations above are valid for every point in space and time. It can be written as

$$[DyeCa^{2+}](x,t) = Dye_t(x)\cdot\frac{[F(x,t) - F_{\min}(x)]}{[F_{\max}(x) - F_{\min}(x)]}, \tag{4.48}$$

and by substituting $F_0 = c \cdot F_{\min}$ (eqn. 4.28 in section 4.4.1) the concentration of the complexed dye is also equivalent to

$$[DyeCa^{2+}](x,t) = Dye_t(x)\cdot\frac{c\cdot F(x,t) - F_0(x)}{(q-1)\cdot F_0(x)}. \tag{4.49}$$

The concentration of the complexed dye was obtained with this equation, as it has the advantage, that it is only explicitly dependent on properties of the dye, but not on the absolute values of $F_{\max}$ or $F_{\min}$. In fact, it is independent of any properties of the utilized optical setup, as long as the dye concentration is known.

The spatially and temporally resolved $[Ca^{2+}]$ can now be obtained from the concentration of complexed dye as follows. During Ca^{2+} sparks, $[Ca^{2+}]$ is changing steeply in space and

time. For the nanodomain Ca^{2+} signals measured in this work it is evaluated as that needed to produce the observed change in fluorescence. It was therefore numerically calculated by solving the diffusion-reaction equation that governs the evolution of dye bound to Ca^{2+} ions, which is given by

$$\frac{\partial[DyeCa^{2+}](x,t)}{\partial t} = k_{on}[Dye](x,t)[Ca^{2+}](x,t) - k_{off}[DyeCa^{2+}](x,t) + D_{DyeCa^{2+}}\Delta[DyeCa^{2+}](x,t), \tag{4.50}$$

where k_{on} and k_{off} are the on and off rate constants for the reaction of Ca^{2+} ions with the dye and $D_{DyeCa^{2+}}$ is the diffusion coefficient for the complexed dye. The necessary numerical differentiation in space and time was carried by convolution with a 17-element Kaiser window kernel, with a corner frequency of either 2.45 μm^{-1} or 1.75 μm^{-1} [Hamming R.W., 1989].

4.4.6 Calculation of nanodomain Ca^{2+} release

This section describes how to calculate the Ca^{2+} release flux from the spatially resolved concentration of dye bound to Ca^{2+} ions. To achieve that in microdomain experiments, the sole difficulty has been to determine the rate of removal of Ca^{2+} ions by buffers in the cell, which must be added to the rate of change of free and dye-bound Ca^{2+} ions to calculate release flux from the SR. The same applies to nanodomain experiments, but the mobility across the spatial coordinate of the diffusible buffers has to be included. Therefore, the Ca^{2+} release flux from the SR is given by

$$\frac{\partial Ca^{2+}{}_{release}(x,t)}{\partial t} = \frac{\partial[Ca^{2+}](x,t)}{\partial t} - D_{Ca^{2+}}\Delta[Ca^{2+}](x,t) + \\ + \frac{\partial[DyeCa^{2+}](x,t)}{\partial t} - D_{DyeCa^{2+}}\Delta[DyeCa^{2+}](x,t) + \frac{\partial rem}{\partial t}(x,t), \tag{4.51}$$

where $D_{Ca^{2+}}$ and $D_{DyeCa^{2+}}$ are the diffusion coefficients for Ca^{2+} ions and their complex with the dye and $\frac{\partial rem}{\partial t}$ is the removal term, which is given by

$$\frac{\partial rem(x,t)}{\partial t} = MP \cdot \left(\frac{[Ca^{2+}]}{[Ca^{2+}] + K_p} \right)^2 (x,t) + \\ + \sum_i k^i{}_{on} \cdot [b^i](x,t) \cdot [Ca^{2+}](x,t) - k_{off}{}^i \cdot [b^i Ca^{2+}](x,t) - D_{b^i Ca^{2+}} \cdot \Delta[b^i Ca^{2+}](x,t). \tag{4.52}$$

The first term in this equation gives the rate at which Ca^{2+} ions are pumped back into the SR by the SR Ca^{2+} pump, where *MP* is the maximum pump rate and the term within the brackets

is the same expression as in section 4.3.7 for the occupancy of the Ca^{2+} binding sites at the pump at every point in space or time [Brum et al., 1988b]. The next term is a sum over all buffers b^i inside the cell that react with Ca^{2+} ions and may diffuse within the myoplasm. In this expression $D_{b^iCa^{2+}}$ is the diffusion coefficient of b^i, $k^i{}_{on}$ and $k^i{}_{off}$ are the onrate and offrate for Ca^{2+} binding for the respective buffer, $b^i{}_{total}$ is the total buffer concentration, $[b^iCa^{2+}]$ and $[b^iMg^{2+}]$ are the concentrations of the buffer bound to Ca^{2+} and Mg^{2+} respectively, where the buffer binding to Mg^{2+} ions is given by its own diffusion-reaction equation as

$$\frac{\partial[b^iMg^{2+}](x,t)}{\partial t} = k^i{}_{on}\cdot[b^i](x,t)\cdot[Mg^{2+}] - k^i{}_{off}\cdot[b^iMg^{2+}](x,t) + D_{b^iMg^{2+}}\cdot[b^iMg^{2+}](x,t). \quad (4.53)$$

Note that the free buffer at any point in space and time is assumed to follow the expression

$$[b^i] = b_{total}{}^i - [b^iCa^{2+}] - [b^iMg^{2+}], \quad (4.54)$$

which is equivalent to saying that the total buffer concentration at any place is constant over time, because free and bound buffer are assumed to have the same diffusion coefficient.

The considered buffers b^i inside the myoplasm are ATP, parvalbumin, EGTA, troponin and the pump binding sites. As one can see, there are two contributions for the Ca^{2+} pump to the change of $[Ca^{2+}]$ inside the myoplasm, the binding of Ca^{2+} ions to the pump sites and, in dependence of how many pump sites are bound, the actual pumping of Ca^{2+} ions into the SR. In addition, not all terms have to be considered for all buffers. The diffusible buffers in the myoplasm are ATP, parvalbumin and EGTA, for the rest the diffusion coefficient is set to zero. Furthermore, only ATP and parvalbumin form complexes with Mg^{2+} ions, for the rest the concentration terms governing the binding to Mg^{2+} ions is set to zero as well. $[Mg^{2+}]$ is assumed to stay constant with respect to time and space.

Ca^{2+} release flux was determined by first calculating the time as well as spatial derivatives of $[Ca^{2+}]$. After that only the removal term has to be calculated as the spatial and time derivatives of $[DyeCa^{2+}]$ have already been calculated to obtain $[Ca^{2+}]$. The removal term is then determined by simultaneously solving the diffusion-reaction equations for all buffers using the Euler forward method. For that, the time $it_j = t_{j+1} - t_j$ between two adjacent values $[Ca^{2+}](x_i,t_j)$ is divided into 100 intervals (interval time=0.02 ms). The adjacent values of $[Ca^{2+}](x,t)$ in time are linearly interpolated to obtain dca_{ij}, the increment in free calcium concentration defined as

$$dca_{ij} = \frac{[Ca^{2+}](x_i,t_{j+1}) - [Ca^{2+}](x_i,t_j)}{100}. \quad (4.55)$$

Then for each interval it_j, starting at $j = 0$ (that means calculating in the same direction as real time within the numerical array), the removal terms are subsequently calculated as follows:
At each of the 100 time points t_k within it_j, the removal terms are calculated for each point in space x_i, using the value of $\left[Ca^{2+}\right](x_i, t_j) + (k-1) \cdot dca_{ij}$ as the current concentration of free calcium. Hence, a value at a prior point in time for a free calcium concentration determines the mass action and diffusion at the next point in time.
Finally, all terms corresponding to $\left[Ca^{2+}\right]$, to $\left[DyeCa^{2+}\right]$ and to removal are added to yield the spatially and temporally resolved Ca^{2+} release flux. The differentiations with respect to time and space have been carried as in section 4.4.5. The numerous dissociation constants, rate constants and other necessary parameter used in the calculation of Ca^{2+} release flux from the SR are given in table (4.6).
After the Ca^{2+} release flux it is interesting to calculate the underlying corresponding ionic electric current under the assumption, that all Ca^{2+} ions were released through a point source, as then comparisons to electrophysiological measurements of single channel currents are possible. This can be achieved by computing the volume integral of the spatially resolved Ca^{2+} release flux. Under the assumption that Ca^{2+} sparks are spherically symmetric this point source current is calculated as

$$I_{ca^{2+}} = \sum_{i=1}^{k} 4 \cdot \pi \cdot (i - 0.5)^2 \cdot \frac{\partial Ca^{2+}{}_{release}(i,t)}{\partial t} \cdot dx^3 \,,$$

where i is the array index in x-direction (the spark maximum is at $i = 0$), dx is the true spatial increment of the release flux array (i.e. dx = 0.1365 µm in the Olympus setup at zoom 5) and k is the last array index number (determines the radius of the volume integral).

Fluo3: Ca^{2+} on rate	$3.2 \cdot 10^{7}$ $M^{-1}s^{-1}$	Harkins et al., 1993
Fluo3: Ca^{2+} dissociation constant	1.03 µM	Harkins et al., 1993
EGTA: Ca^{2+} on rate	$0.2 \cdot 10^{7}$ $M^{-1}s^{-1}$	Smith et al., 1984
EGTA: Ca^{2+} dissociation constant	1 µM	Smith et al., 1984
Troponin: Ca^{2+} on rate	$5.7 \cdot 10^{6}$ $M^{-1}s^{-1}$	Baylor et al., 1983
Troponin: Ca^{2+} off rate	11.4 s^{-1}	Baylor et al., 1983
ATP: Ca^{2+} on rate	$1.5 \cdot 10^{6}$ $M^{-1}s^{-1}$	Baylor et al., 1998
ATP: Ca^{2+} off rate	$3 \cdot 10^{4}$ s^{-1}	Baylor et al., 1998
ATP: Mg^{2+} on rate	$1.5 \cdot 10^{6}$ $M^{-1}s^{-1}$	Baylor et al., 1998
ATP: Mg^{2+} off rate	195 s^{-1}	Baylor et al., 1998
Parvalbumin: Ca^{2+} on rate	$1.25 \cdot 10^{8}$ $M^{-1}s^{-1}$	Baylor et al., 1983
Parvalbumin: Ca^{2+} off rate	0.5 s^{-1}	Baylor et al., 1983
Parvalbumin: Mg^{2+} on rate	$3.3 \cdot 10^{4}$ $M^{-1}s^{-1}$	Baylor et al., 1983
Parvalbumin:Mg^{2+} off rate	3 s^{-1}	Baylor et al., 1983
Maximum pump rate	9.8 mM s^{-1}	Ríos et al., 1999
[Parvalbumin]	1 mM	Baylor et al., 1983
[Pump sites]	0.2 mM	Baylor et al., 1983
D_{Ca}	$3.5 \cdot 10^{-6}$ cm^2s^{-1}	Kushmerick et al., 1969
D_{Dye}	$2 \cdot 10^{-7}$ cm^2s^{-1}	Harkins et al., 1993
D_{ATP}	$1.4 \cdot 10^{-6}$ cm^2s^{-1}	Baylor et al., 1998
$D_{Parvalbumin}$	$2.6 \cdot 10^{-7}$ cm^2s^{-1}	Pechère et al., 1973
D_{EGTA}	$3.6 \cdot 10^{-7}$ cm^2s^{-1}	Pizarro et al., 1991

Table 4.6 Parameters for the calculation of nanodomain Ca^{2+} release. Values are the same as in Ríos et al. [1999].

5 Results

The methods derived in chapter 4 were applied within several experimental projects and the outcome of these projects is presented here. This chapter is divided in three parts, first, results on the measurement and quantification of microdomain Ca^{2+} release from the SR are shown. These experiments have been carried out under two conditions: in skeletal muscle fibers with a high and a normal intracellular free Mg^{2+} ion concentration. Thereafter experiments on amphibian nanodomain Ca^{2+} release under a multitude of conditions are presented. The different conditions had the purpose to evaluate the contribution of CICR to the underlying Ca^{2+} signal, and specifically to answer, if a Ca^{2+} spark could be generated by the opening of a single RyR. The last section shows the results on nanodomain Ca^{2+} release in mammalian skeletal muscle, where elementary events of Ca^{2+} release could be measured in abundance for the first time in muscle research.

5.1 Microdomain Ca^{2+} release

Microdomain Ca^{2+} release was measured and quantified in voltage-clamped cut fibers of the frog *rana pipiens* under two conditions, in a high and a normal intracellular [Mg^{2+}]. For the normal, physiological condition the reference intracellular solution was used (see section 4.1.1) and the high Mg solution was applied to reach a high intracellular [Mg^{2+}]. During the experiment, first, the high Mg solution was filled into the end pools of the double vaseline gap chamber and [Mg^{2+}] was measured in the middle section until it was equilibrated as described in section 4.3.1, then several step depolarizations of various durations and voltages were applied, including those that elicited the Ca^{2+} transients shown in Fig. 5.1 A. This set of pulses allowed the determination of the removal system as described in section 4.3.7 and the calculation of the Ca^{2+} release records shown below the respective Ca^{2+} transient. Then the solution in the endpool was changed to the reference solution and [Mg^{2+}] was measured until 0.61 mM was reached. Under this condition, after recovery from the high intracellular [Mg^{2+}], the Ca^{2+} transients shown in Fig. 5.1 B were induced by step depolarizations to the indicated voltage. Again additional pulses were applied for the determination of the removal system in reference condition and the respective Ca^{2+} release was computed for each Ca^{2+} transient. The parameters for the removal system that allowed the calculation of Ca^{2+} release records under both conditions are given in the legend of Fig. 5.1.

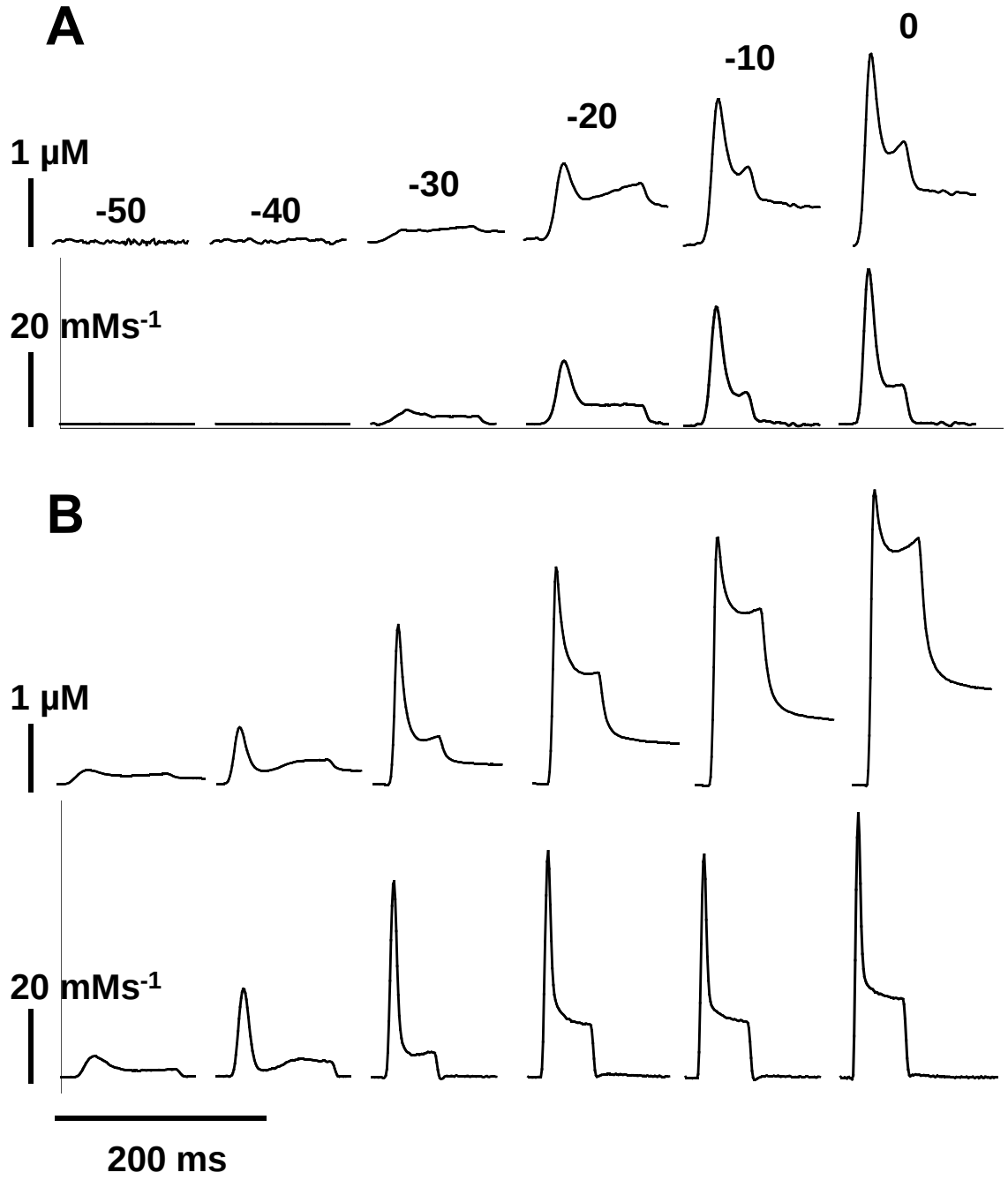

Fig. 5.1 Microdomain Ca^{2+} transients (top) and Ca^{2+} release records (bottom) induced by step depolarizations from -90 mV to the indicated potential (in mV) measured first in the high Mg solution and then, after recovery, in the reference solution in one fiber. The duration of the depolarization was either 50 ms or 100 ms. The parameters of the removal system used for the calculation of Ca^{2+} release records were in high Mg:
$k_{on,Ca:troponin}$= 125 $\mu M^{-1}s^{-1}$, $k_{off,Ca:troponin}$= 1200 s^{-1}, [troponin]= 240 µM, $k_{on,Ca:parvalbumin}$= 100 $\mu M^{-1}s^{-1}$, $k_{off,Ca:parvalbumin}$= 1 s^{-1}, $k_{on,Mg:parvalbumin}$= 0.03 $\mu M^{-1}s^{-1}$, $k_{off,Mg:parvalbumin}$= 3 s^{-1}, [parvalbumin]= 1 mM, $k_{on,Ca:EGTA}$= 4 $\mu M^{-1}s^{-1}$, $k_{off,Ca:EGTA}$= 10 s^{-1}, [EGTA]= 3 mM, K_{pump}= 1 µM, maximum pump rate= 0.5 mMs^{-1}, [pump sites]= 100 µM, $[Mg^{2+}]$= 7 mM;
in reference:
$k_{on,Ca:troponin}$= 125 $\mu M^{-1}s^{-1}$, $k_{off,Ca:troponin}$= 1200 s^{-1}, [troponin]= 240 µM, $k_{on,Ca:parvalbumin}$= 100 $\mu M^{-1}s^{-1}$, $k_{off,Ca:parvalbumin}$= 1 s^{-1}, $k_{on,Mg:parvalbumin}$= 0.03 $\mu M^{-1}s^{-1}$, $k_{off,Mg:parvalbumin}$= 3.0 s^{-1}, [parvalbumin]= 1 mM, $k_{on,Ca:EGTA}$= 1.7 $\mu M^{-1}s^{-1}$, $k_{off,Ca:EGTA}$= 9 s^{-1}, [EGTA]= 10 mM, K_{pump}= 1 µM, maximum pump rate= 0.5 mMs^{-1}, [pump sites]= 100 µM, $[Mg^{2+}]$= 0.61 mM.

The Ca^{2+} transients and Ca^{2+} release records shown are a selection taken from induced Ca^{2+} signals obtained by depolarizations within the range of -60 mV to +30 mV. The free Ca^{2+} ion concentration in this fiber increased to several micromolar at its maximum in both solutions. In all cases, when Ca^{2+} ions were released, the typical time course of Ca^{2+} release under voltage-clamp was developed (see section 2.3), where the release rate rapidly exhibits a peak and thereafter declines to a more steady level of Ca^{2+} release. The peak release rates observed reached values of several tens of millimol per second. However, there exist striking differences between Ca^{2+} transients and Ca^{2+} release records in the two studied conditions.

Ca^{2+} transients in reference conditions could be induced starting at a depolarization voltage of -50 mV. In reference solution a large peak compared to the steady level was already developed at -40 mV. Ca^{2+} release in the high Mg solution was only observed at depolarization voltages of -30 mV or higher. Furthermore, the activation of Ca^{2+} release in high Mg was slowed down, resulting in a peak release rate that was reached at later times after the start of the depolarization than in reference. Still, at depolarization voltages of 0 mV and higher (not shown) the time course of Ca^{2+} release in high Mg was very similar to reference, except for the slowed activation. In all 5 fibers evaluated, where exactly the same experiment was carried out, the magnitude of the peak release rate as well as the steady release rate (taken as the last value before the repolarization to -90 mV) was reduced by high intracellular $[Mg^{2+}]$ (between 9-88% of reference).

	7.0 mM $[Mg^{2+}]$			0.61 mM $[Mg^{2+}]$		
fiber #	$peak_{max}$	$V_{0.5}$	k	$peak_{max}$	$V_{0.5}$	k
1524	52.16	-9.9	0.1	72.48	-34.68	0.13
1525	14.2	-8.59	0.1	137.42	-31.11	0.11
1537	33.98	-9.4	0.11	40.70	-27.53	0.14
1544	37.96	-17.61	0.09	-	-	-
1602	23.13	-10.22	0.11	35.41	-30.59	0.11
	$steady_{max}$	$V_{0.5}$	k	$steady_{max}$	$V_{0.5}$	k
1524	12.29	-14.08	0.1	22.29	-17.26	0.07
1525	2.95	-12.95	0.09	32.08	-22.60	0.09
1537	12.23	-13.57	0.12	20.03	-17.53	0.1
1544	8.63	-16.58	0.15	-	-	-
1602	10.91	-23.10	0.11	12.34	-25.78	0.1

Table 5.1 Fit parameters necessary for the normalization of the voltage distributions of the peak release rate and the steady value of release (the value of the release rate at the time of repolarization) in each of the studied fibers according to equation 5.1.

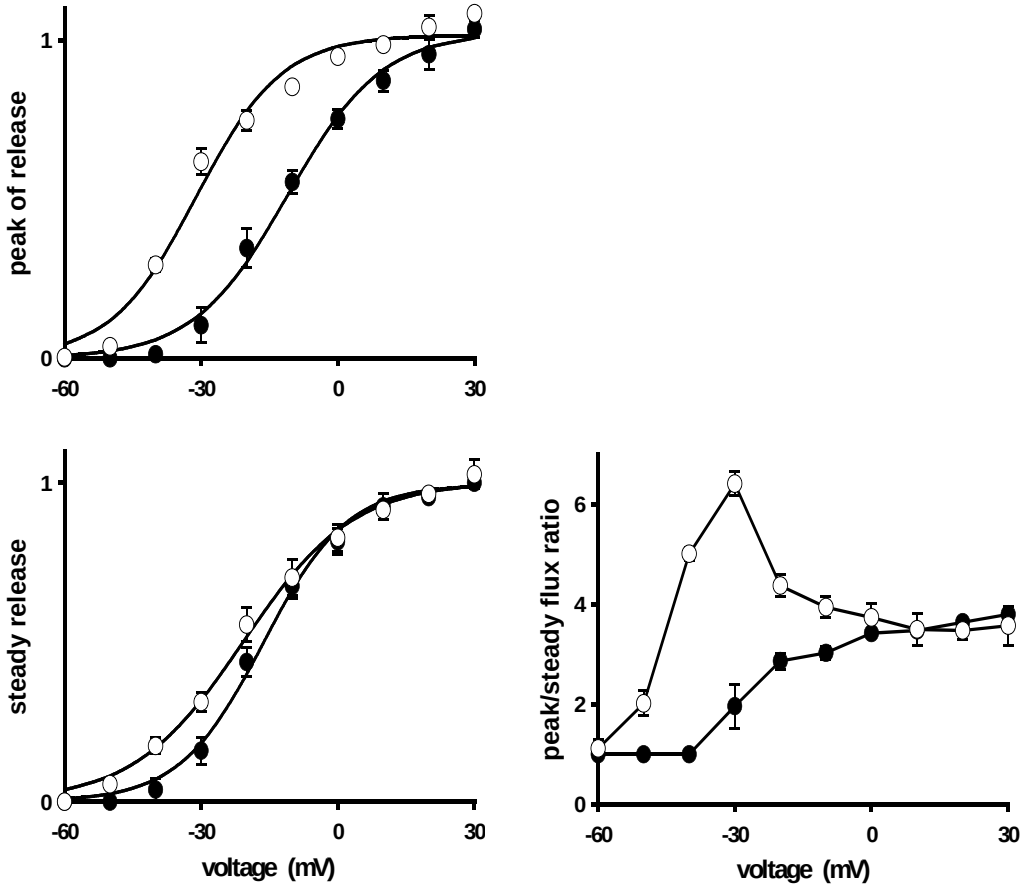

Fig. 5.2 Averaged distributions of the peak release rate, the steady value of the release rate and the ratio of peak release rate over steady value with voltage in reference (○) and high intracellular [Mg^{2+}] (●). The distribution of the peak release rates and the steady values were shifted to greater depolarization voltages by the high Mg solution. In addition, the distribution of the ratio of peak release rate over steady value became non-monotonic in high intracellular [Mg^{2+}].

The values for the peak release rate was plotted with voltage and the voltage dependence of this distribution was fitted with an equation of the form

$$P(V) = peak_{\max} \cdot \frac{1}{1 + e^{k(V - V_{0.5})}}, \tag{5.1}$$

where $peak_{\max}$ is the maximum value at the highest depolarization voltage, k^{-1} is proportional to the slope of the distribution at $V_{0.5}$, and $V_{0.5}$ is the voltage where the monotonic function *P(V)* reaches the half of its maximum value. The distribution of steady values with voltage was fitted in the same manner (obtaining a value $steady_{max}$ instead of $peak_{max}$). The fitted values of these three parameters obtained for each studied fiber for the two distributions is given in table 5.1. Then all distributions were normalized to their fitted maximum value and averaged for peak and steady values, respectively. The resulting average distributions that

show the voltage dependence for the peak of release and the steady value are shown in Fig. 5.2 and were each again fitted with equation 5.1. This way the shift of the voltage distributions of peak release rate as well as steady value to greater depolarization voltages induced by the high Mg condition can be quantified. Thus this shift was +20±3 mV for the voltage distribution of the peak release rate and +4.3±0.5 mV for the voltage distribution of the steady value.

Fig. 5.2 also shows the voltage distribution of the averaged ratio of peak over steady value for both conditions. This distribution was obtained by first computing the ratios in each fiber for each voltage and then averaging the data. The voltage dependence of this ratio of peak over steady value is strikingly different in the two conditions. In reference the distribution with voltage is non-monotonic, exhibiting a maximum at -30 mV, while in high intracellular [Mg^{2+}] it is monotonically rising with voltage. However, the values of the averaged ratios are basically the same for voltages greater than 0 mV [Kirsch et al., 1999].

5.2 Nanodomain Ca^{2+} release in amphibian muscle

In this section the results on a variety of experiments on nanodomain Ca^{2+} release in amphibians are presented. First, the results from experiments with voltage-clamped cut fibers under the same conditions as in the microdomain studies, a normal and a high intracellular free Mg^{2+} ion concentration are shown, where the spatially resolved fluorescence of Ca^{2+} sparks and the underlying Ca^{2+} release were characterized and quantified. Then striking morphological differences of elementary Ca^{2+} release events resolved between different experimental conditions in voltage-clamped cut fibers, including the two conditions of the first set of experiments, are revealed, which can be based on the structure of the Ca^{2+} release site. Then the effect of caffeine, an agonist for the opening of RyRs by Ca^{2+} ions in the myoplasm, on nanodomain Ca^{2+} release in chemically skinned fibers is described and the spatially resolved Ca^{2+} release flux from the SR in reference conditions and under exposure to caffeine is calculated.

5.2.1 Ca^{2+} sparks in high intracellular [Mg^{2+}]

In most experiments on high intracellular [Mg^{2+}] the end pools were filled with the high Mg solution and several line scan images were acquired during the time, when the Mg^{2+} ions are still diffusing into the middle section of the fiber, where the Ca^{2+} signals were measured as described in section 4.4. This way nanodomain Ca^{2+} release could be measured at intermediate intracellular [Mg^{2+}] until the whole fiber was equilibrated with the value of [Mg^{2+}] as set in the end pools. Experiments following this procedure will be referred to as washin experiments. The upper panel in Fig 5.3 shows images, normalized to the resting fluorescence, after an exposure to the high Mg solution for 60 minutes (intermediate [Mg^{2+}]),

the lower panel after exposure for 120 minutes, when the fiber was equilibrated with 7.0 mM [Mg^{2+}]. A step depolarization from -90 mV to -25 mV and to -30 mV for 400 ms was applied during the time of acquisition of the images at the left and the right side, respectively. At the white arrows time courses of normalized fluorescence have been extracted from the image and were plotted as black traces to the right of images. Note, that the scale bars for the time courses in intermediate and 7.0 mM [Mg^{2+}] are different.

In all images the step depolarization induced Ca^{2+} release from the SR, but the magnitude of the resulting change in fluorescence has decreased upon reaching 7.0 mM [Mg^{2+}] at both depolarization voltages. After 60 minutes of exposure to the high Mg solution there are more discrete release events visible than after 120 minutes at the corresponding voltage and the amplitude for any occurring Ca^{2+} spark appears to be smaller in 7.0 mM [Mg^{2+}]. Thus the intracellular [Mg^{2+}] of 7.0 mM has led to a reduced frequency and amplitude of Ca^{2+} sparks compared to conditions with lower [Mg^{2+}].

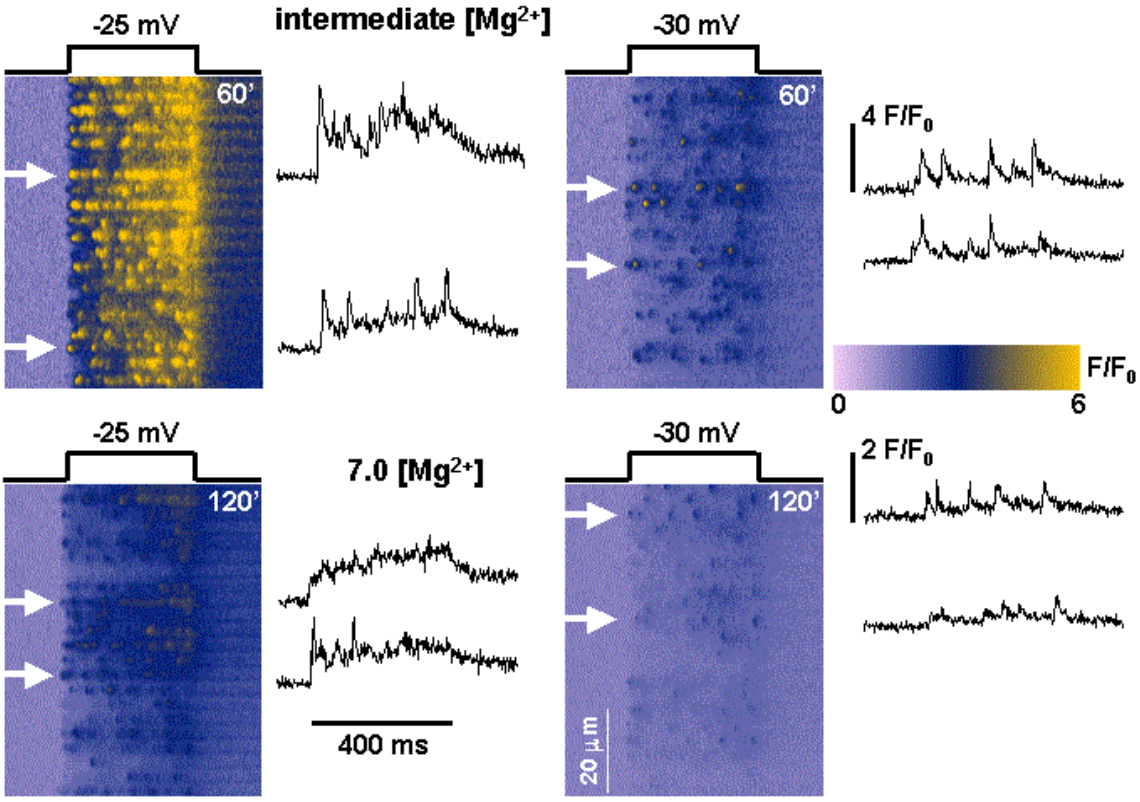

Fig. 5.3 Effect of high intracellular [Mg^{2+}] on local Ca^{2+} release elicited by step depolarizations to -25 mV and -30 mV. The upper panel shows normalized fluorescence images after an exposure to the high Mg solution for 60 minutes (intermediate [Mg^{2+}]), the lower panel after exposure for 120 minutes, when the fiber was equilibrated with 7.0 mM [Mg^{2+}]. Compared to the intermediate [Mg^{2+}] condition Ca^{2+} sparks are less frequent and appear smaller in 7.0 mM [Mg^{2+}] at both voltages. The white arrows mark the locations of some extracted time courses of fluorescence, shown to the right of the images. Note, that the scale bars for the time courses in intermediate and 7.0 mM [Mg^{2+}] are different.

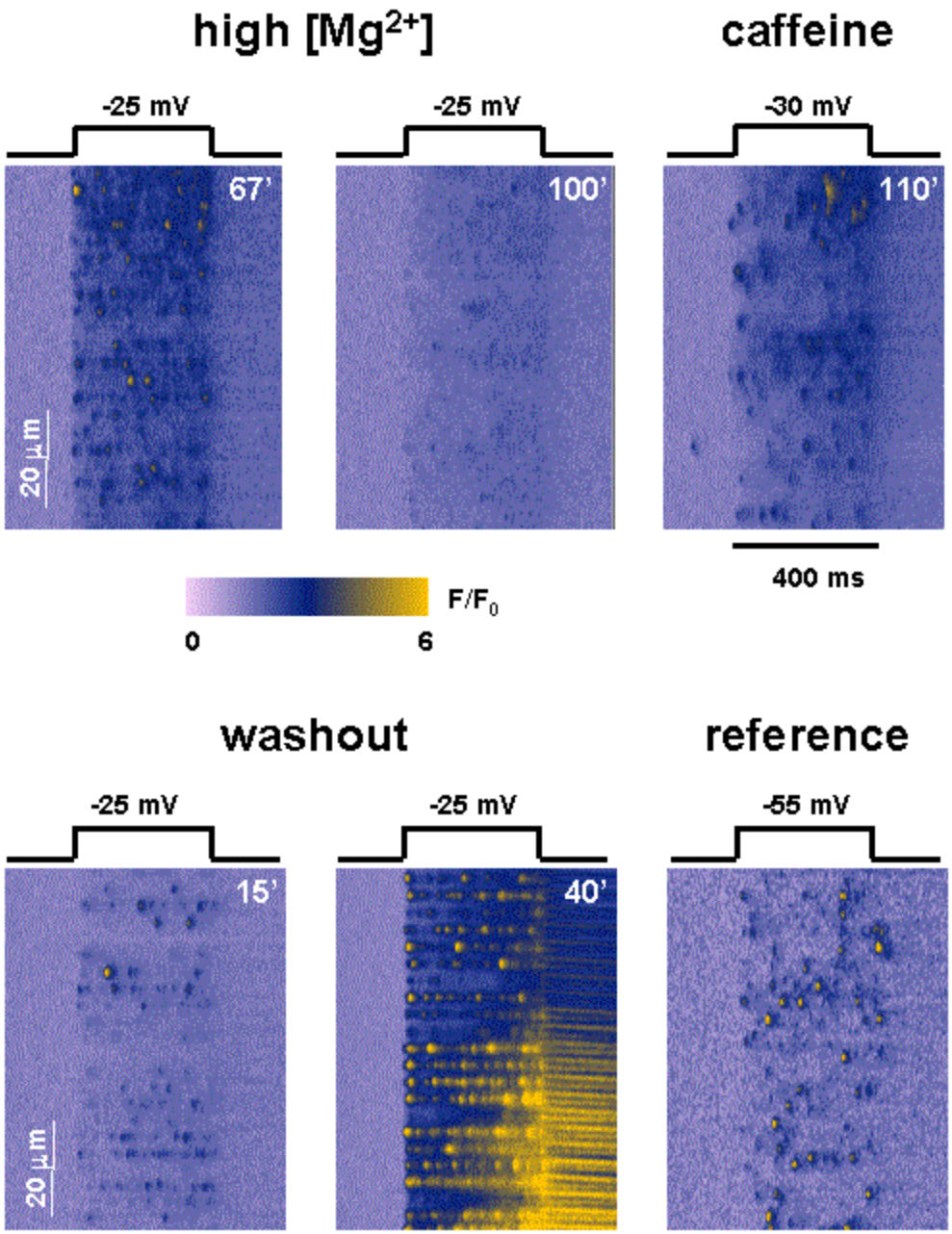

Fig. 5.4 The first two images in the upper panel show another fiber exposed to the high Mg solution after 67 and 100 minutes. Ca^{2+} sparks induced by step depolarizations from -90 mV to -25 mV appear less frequent and smaller with time. After 110 minutes 0.5 mM caffeine was added to the middle pool and then a depolarization to -30 mV elicited Ca^{2+} sparks with a higher frequency and higher amplitude than before, showing that the effect of high intracellular [Mg^{2+}] is reversible by caffeine. The lower panel corresponds to a fiber that was first exposed to the high Mg solution until it was equilibrated with 7.0 mM [Mg^{2+}]. Then the images shown were acquired 15 and 40 minutes after the solution in the end pools was exchanged to the washout solution. The number and amplitude of Ca^{2+} sparks induced by step depolarizations to -25 mV increased with time and the fiber even exhibited some movement after 40 minutes (skid pattern). This shows that the effect of 7 mM [Mg^{2+}] can be reversed by washout.

This effect of high intracellular [Mg^{2+}] was reversible. The upper panel of Fig. 5.4 shows another experiment, where the end pools were filled with the high Mg solution and line scan images that include step depolarizations to -25 mV were acquired after 67 and 100 minutes of

exposure time and normalized to their resting fluorescence (left two images). Again the frequency and amplitude of Ca^{2+} sparks was reduced with higher exposure time. Ten minutes later, adding of 0.5 mM caffeine to the external solution in the middle pool resulted in the occurrence of Ca^{2+} sparks with a higher frequency and greater amplitude at an even lower depolarization voltage of -30 mV (right image).

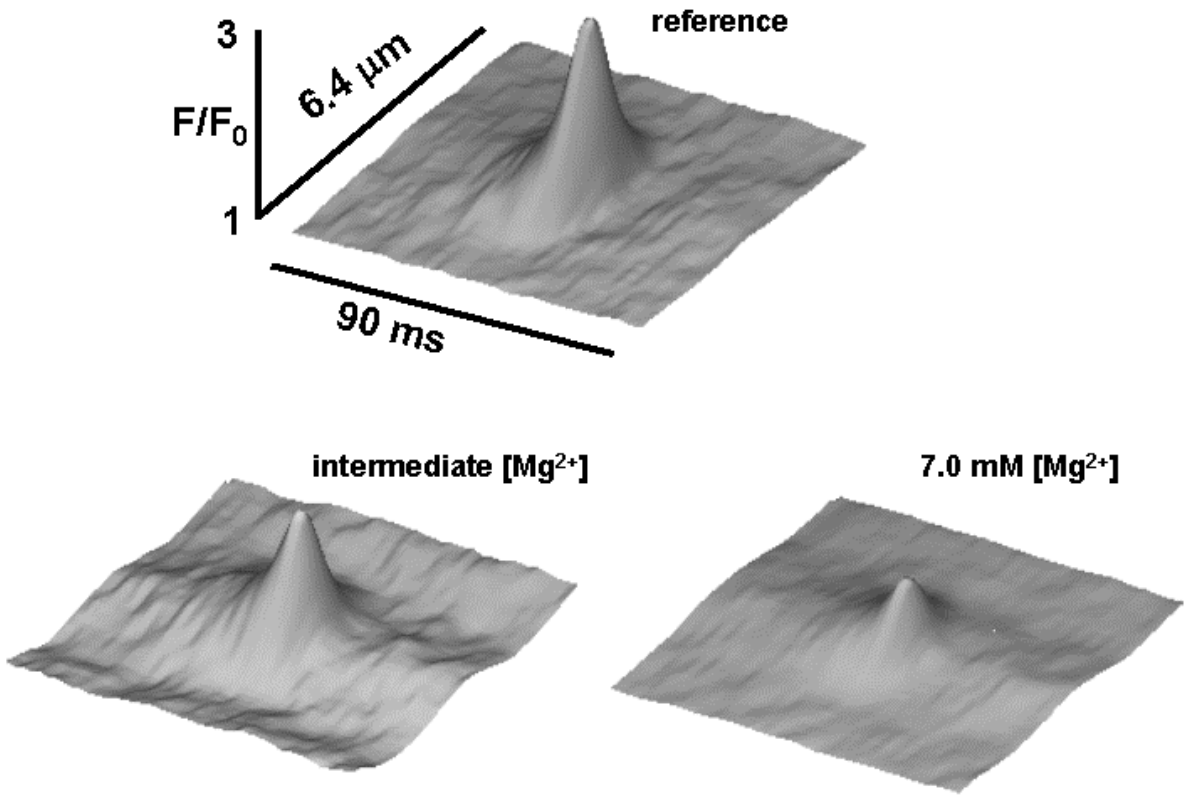

Fig. 5.5 Spatio-temporal representation of Ca^{2+} sparks under different experimental conditions for a typical fiber under reference condition and fiber 0107b (see table 5.2). These surface plots were obtained by the superposition of all events with respect to the location of their maximum amplitude and subsequent averaging. The reduced average spark amplitude in conditions with elevated intracellular [Mg^{2+}] is clearly visible.

In the lower panel of Fig. 5.4 the left two images show another experiment, where a fiber recovered from a high intracellular [Mg^{2+}] condition. In this experiment, the fiber was first equilibrated with an intracellular [Mg^{2+}] of 7.0 mM, thereafter the washout solution was filled into the end pools, which had only 0.130 mM [Mg^{2+}] and contained the Mg^{2+} ion buffer citric acid. An experiment following this procedure will be referred to as a washout experiment. The images of normalized fluorescence shown in the figure correspond to the time of 15 and 40 minutes after the end pools were filled with the washout solution and include a depolarization from -90 mV to -25 mV for 400 ms. The frequency and amplitude increased visually by washout. The fiber started even to contract by the applied depolarization to -40 mV after 40 minutes of washout. This can be seen by the fluorescence pattern that shifts

downward with time after the step pulse (the normalization procedure failed for that region of the image). The bottom right image shows a fiber in reference solution as a comparison to emphasize that under normal physiological conditions Ca^{2+} sparks of medium frequency and high amplitude can be induced by step depolarizations from -90 mV to -55 mV and that depolarization voltages of -40 mV or higher would generate so many Ca^{2+} sparks, that they could not be distinguished from each other. Therefore, the condition with high intracellular [Mg^{2+}] allows the measurement of Ca^{2+} sparks at higher depolarization voltages.

fiber #	time (min)	#	amplitude (F/F_0)	FWHM (µm)	FDHM (ms)	rise time (ms)
	Washin					
0103a	60	100	**2.43±0.05**	0.80±0.04	**8.50±0.36**	**5.51±0.32**
	120	130	**2.19±0.03**	0.82±0.04	**6.91±0.22**	**4.63±0.26**
	+caffeine	65	**2.68±0.08**	**1.41±0.08**	**8.34±0.41**	4.82±0.25
0108a	60	76	**2.51±0.05**	**0.88±0.04**	**8.87±0.37**	**5.55±0.34**
	90	27	**2.17±0.05**	**0.76±0.06**	**7.04±0.39**	**4.56±0.40**
	+caffeine	39	**2.68±0.09**	**1.09±0.09**	**8.56±0.54**	**6.43±0.49**
1022a	45	141	**3.17±0.05**	**0.95±0.03**	9.73±0.3	**5.56±0.23**
	75	139	**3.09 0.07**	**0.85 0.03**	9.76 0.32	**6.61 0.29**
1106a	50	306	**2.45±0.03**	0.82±0.02	9.4±0.21	5.8±0.18
	150	83	**2.32±0.04**	0.81±0.04	9.18±0.38	6.02±0.34
0107b	55	209	**2.67±0.04**	**0.89±0.03**	**9.59±0.24**	**6.3±0.24**
	115	191	**1.99±0.02**	**0.82±0.02**	**9.2±0.24**	**5.59±0.21**
	Washout					
1016a8	15	22	**2.82±0.15**	0.93±0.08	9.91±0.92	**4.78±0.40**
	45	219	**3.0±0.05**	0.95±0.02	10.27±0.24	**5.9±0.21**
0623a	18	138	**2.47 0.05**	**0.78 0.03**	**8.81 0.26**	**5.58 0.32**
	78	442	**2.68 0.04**	**0.87 0.02**	**8.29 0.16**	**5.03 0.17**

Table. 5.2 Averaged morphological parameters according to section 4.4.3 for each studied fiber under the respective condition in five washin and two washout experiments. The time in the table denotes the time after the exchange of the end pool solution. # refers to the number of events analyzed under the respective condition. Bold print was used when parameters changed significantly.

The average effect of high intracellular [Mg^{2+}] is visually demonstrated in Fig. 5.5, where many Ca^{2+} sparks obtained under reference, intermediate [Mg^{2+}] and 7.0 mM [Mg^{2+}] conditions were superimposed with respect to the location of their maximum values of normalized fluorescence (F/F_0) and averaged. It should be noted that the Ca^{2+} average shown for the reference condition was constructed with events from a fiber that was never exposed to

high intracellular [Mg^{2+}] and corresponds to an experiment where the measured Ca^{2+} sparks exhibited typical morphological parameters. The conditions with elevated [Mg^{2+}] are from another fiber after exposure with the high Mg solution, where the intermediate [Mg^{2+}] condition refers to events recorded before the fiber was equilibrated with 7.0 mM [Mg^{2+}]. The reduced amplitudes of the averaged Ca^{2+} sparks in elevated [Mg^{2+}] are clearly visible.

All recorded elementary Ca^{2+} release events were individually analyzed as described in section 4.4.3. The averages of all obtained parameter values in the respective fiber for a respective condition are given in table 5.2. Five washin and two washout experiments were carried out. At time zero the end pools were filled with either the high Mg solution (washin) or the washout solution. The time in the table denotes at which time the recording of events for the respective row in the table started. In washin experiments the first row for each fiber corresponds to the intermediate [Mg^{2+}] condition and the second row to the 7.0 mM condition. In two experiments caffeine was applied to the middle pool and an additional row for events recorded at 7.0 mM [Mg^{2+}] with caffeine is inserted. The events measured in the two washout experiments fall not into any of three categories of washin experiments and are given to demonstrate the recovery of spark amplitudes with time.

For washin experiments the parameter values for each fiber from table 5.2 were again averaged for general comparison of events under the intermediate [Mg^{2+}] (832 events) and the 7.0 mM [Mg^{2+}] (570 events) condition with the mean amplitude, FWHM, FDHM and rise time of Ca^{2+} sparks under reference conditions taken from a huge database of experiments consisting of 5301 events [González et al. (Kirsch), 2000b]. The obtained values are given in table 5.3.

	amplitude (F/F_0)	FWHM (µm)	FDHM (ms)	rise time (ms)
reference	**2.77±0.24**	**1.17±0.12**	**11.1±1.1**	5.52±0.55
intermediate [Mg^{2+}]	**2.64±0.04**	**0.87±0.03**	**9.22±0.3**	5.74±0.26
7.0 mM [Mg^{2+}]	**2.35±0.04**	**0.81±0.04**	**8.42±0.31**	5.48±0.3

Table 5.3 Average morphological parameters compared between reference and high intracellular [Mg^{2+}]. Intracellular 7.0 mM [Mg^{2+}] reduced the reference amplitude, FWHM and FDHM by as much as 15%, 31% and 24% respectively. Bold print was used when parameters changed significantly.

The parameters in the tables 5.2 and 5.3 confirm the reduction of the average Ca^{2+} spark amplitude by high intracellular [Mg^{2+}]. This decrease was observed in every fiber and on average in 7.0 mM [Mg^{2+}] the amplitude was 15% smaller than in reference condition. Interestingly, on average the FWHM was also decreased by 31%. This decrease in width was not present in every fiber when comparing 7.0 mM [Mg^{2+}] with intermediate [Mg^{2+}], but in the two fibers in table 5.2 (0103a, 1106a), where the FWHM showed no significant change, the value for this parameter was already as low as the averaged value in table 5.3, indicating that the width might have been decreased already under intermediate [Mg^{2+}]. Furthermore, the FDHM was reduced by as much as 24%, but the rise time showed no significant change.

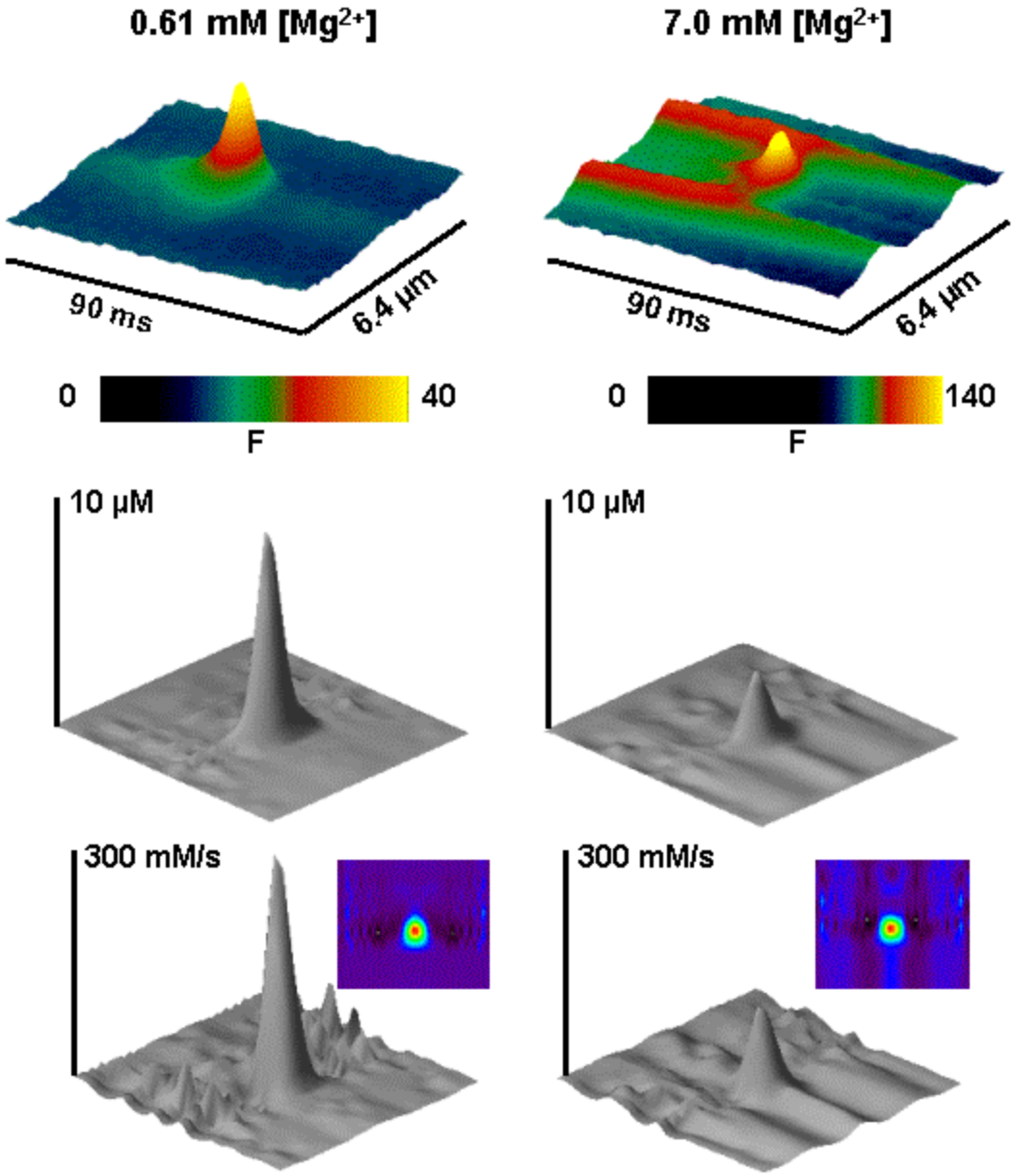

Fig. 5.6 Calculation of spatially and temporally resolved Ca^{2+} release flux for the averages of absolute fluorescence shown at top under 0.61 mM [Mg^{2+}] (reference) and 7.0 mM [Mg^{2+}] conditions. The spatially and temporally resolved [Ca^{2+}](x,t) (middle) and Ca^{2+} release flux (bottom) are greatly reduced in 7.0 mM [Mg^{2+}]. The shape of the Ca^{2+} source was similar under both conditions (blue colored projection).

As Ca^{2+} sparks under high intracellular [Mg^{2+}] are smaller in amplitude, narrower in FWHM and shorter in FDHM, the question arises, if the underlying Ca^{2+} release flux from the SR exhibits a similar reduction. For the calculation of the spatially and temporally resolved Ca^{2+} release, first, averages of absolute fluorescence as well as the corresponding average baseline fluorescence were computed as explained in section 4.4.3. The top of Fig. 5.6. shows the averages of absolute fluorescence obtained under reference (0.61 mM) and

7.0 mM [Mg^{2+}] conditions (Note that the two averages have different intensity scales as well as different color tables). As this are averages of absolute fluorescence, part of the periodic pattern is included in the average. This pattern can be better seen in 7.0 mM [Mg^{2+}] as the total dye concentration in this experiment was higher than in reference (18 µM in reference, 97 µM in 7.0 mM [Mg^{2+}]). Then $\left[Ca^{2+}\right](x,t)$ was computed from these averages as described in section 4.4.5, which is shown below the average. It is clearly visible that the resulting spatio-temporal free Ca^{2+} concentration is greatly reduced by 7.0 mM [Mg^{2+}]. The corresponding spatially and temporally resolved Ca^{2+} release flux is shown at the bottom. In the calculation, the different free Mg^{2+} ion concentrations of the internal solutions were taken into account for the reactions of the Mg^{2+} buffers (ATP, parvalbumin). The Ca^{2+} release flux from the SR is greatly reduced by 7.0 mM [Mg^{2+}] as well. The shape of the source, as shown in the blue colored top view of the Ca^{2+} release flux array, was basically the same in both conditions. Calculating the volume integral of the Ca^{2+} release flux density as described in section 4.4.6 yields the corresponding Ca^{2+} ion current of a point source that is necessary to produce the observed Ca^{2+} release flux density. Using a radius of 0.71 µm (5 pixels) as border for the computation the maximum Ca^{2+} ion current with time was 9.3 pA for the reference condition and 3.9 pA in 7.0 mM [Mg^{2+}].

5.2.2 The effect of caffeine on Ca^{2+} sparks in chemically skinned fibers

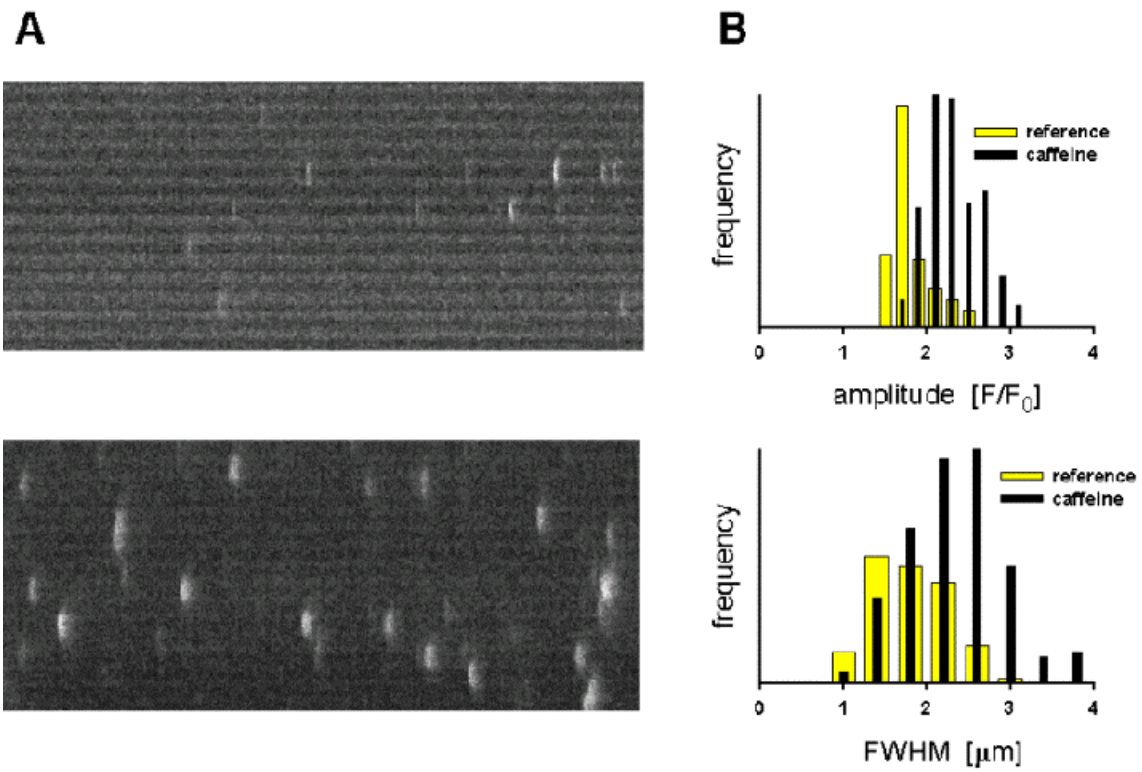

Fig. 5.7 **A** Line scan images of absolute fluorescence in a chemically skinned fiber under reference conditions (top) and after application of caffeine (bottom). The frequency of Ca^{2+} sparks increased when caffeine was present. **B** Histograms for the distribution of the parameters amplitude and FWHM in both conditions. Caffeine shifted the distributions to greater values.

The use of the frog solution (see section 4.1.1) in chemically skinned fibers of *xenopus leavis* induced a low frequency of spontaneous Ca^{2+} sparks as shown in an example line scan in Fig. 5.7 A (top) or Fig. 4.10 A. These Ca^{2+} sparks are presumably produced without the triggering of any DHPRs, as the external membrane is depolarized due to the permeabilization, thus the DHPRs should be inactivated. As in chemically skinned fiber preparations the ionic composition of the intracellular space can be easily controlled, it is the perfect system to study the dependence of Ca^{2+} sparks on ligands in the solution. To gain more evidence on the contribution of CICR to the generation of Ca^{2+} sparks, caffeine, a promoter of CICR, was inserted into the frog solution at 0.5 mM concentration. This resulted first of all in an increased frequency of Ca^{2+} sparks as shown at the bottom of Fig. 5.7 A.

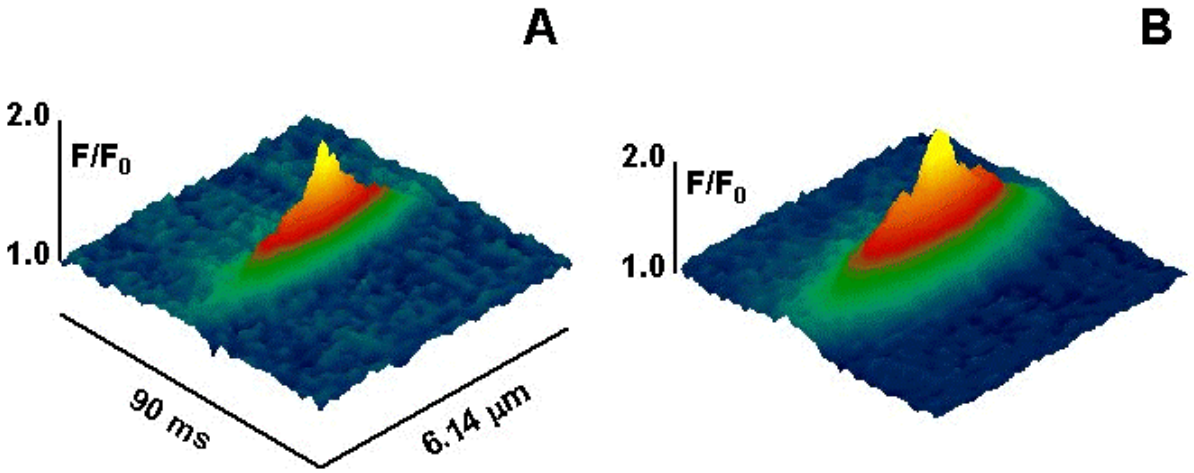

Fig. 5.8 Spatio-temporal representation of the spark average under **A** reference conditions and **B** in presence of caffeine. The average was obtained by matching the peaks of all events from the experiment shown in Fig. 5.7. The increase in amplitude and FWHM after the application of caffeine is clearly visible.

The Ca^{2+} sparks within the line scan images were individually analyzed as described in section 4.4.3 and histograms of the resulting spark parameters were obtained. The histogram for the amplitude and the FWHM of all events for both conditions are shown in Fig. 5.7 B. Caffeine shifted the distribution of events within both histograms to higher values of the respective parameter. This increase of amplitude and FWHM can also be clearly seen in the spatio-temporal 3D-representations of Ca^{2+} spark averages in Fig. 5.8, which include all events under the respective condition measured in the same fiber shown in Fig. 5.7.

	amplitude (F/F_0)	FWHM (µm)	FDHM (ms)	rise time (ms)
reference	1.87±0.02	1.84±0.04	10.10±0.23	7.09±0.23
caffeine	2.06±0.02	2.16±0.04	12.29±0.24	9.69±0.24

Table 5.4 Average morphological spark parameters in the two studied conditions. All parameters increased significantly upon application of caffeine.

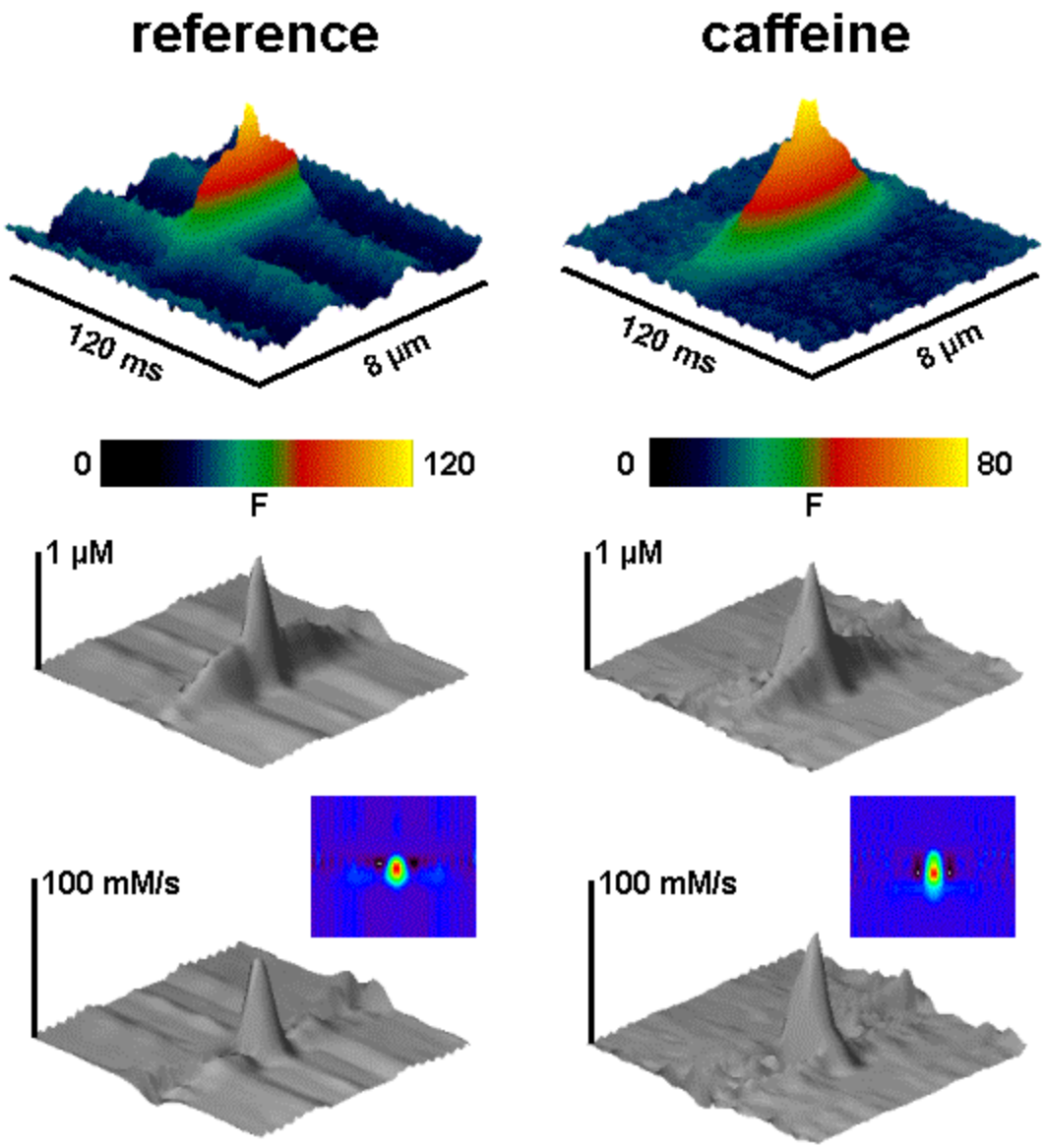

Fig. 5.9 Calculation of spatially and temporally resolved Ca^{2+} release flux for the averages of absolute fluorescence shown at top under reference condition and after application of 0.5 mM caffeine. The spatially and temporally resolved $[Ca^{2+}](x,t)$ (middle) and Ca^{2+} release flux (bottom) are higher after application of caffeine The duration of the Ca^{2+} release flux was longer in caffeine (blue colored projection).

The average morphological spark parameters for the conditions before (reference, 380 events) and after (379 events) the addition of caffeine are given in table 5.4, which shows that all parameters were significantly increased upon application of 0.5 mM caffeine [Kirsch et al., 2000a]. However, the morphological parameters of Ca^{2+} sparks in chemically skinned fibers measured with the Olympus setup were generally smaller than those obtained in voltage clamped cut fibers (i.e. see section 5.2.1) using the Biorad setup. Using the same solution internal spontaneous Ca^{2+} sparks in chemically skinned fibers have also been measured with the Biorad setup and yielded amplitudes that are comparable to those of the voltage-clamped

cut fibers (see section 5.2.3) [Gonzalez et al. (Kirsch), 2000a+b]. Therefore the difference must be either based on the different used frog species and muscles or on the optical setup, where the main difference is only the numerical aperture (NA) (1.15 for Olympus setup; 1.2 for Biorad setup).

Ca^{2+} sparks in high intracellular [Mg^{2+}] were reduced in amplitude and FWHM. This reduction was also given for the underlying spatially and temporally resolved Ca^{2+} release flux from the SR. To determine, if the increase in the average morphological parameters was due to an increased influx of Ca^{2+} ions from the SR, the spatially and temporally Ca^{2+} release flux was calculated from the averages of absolute fluorescence shown in Fig. 5.9 (top). Note again the different scale and color table used for the averages under the two conditions. That the periodic pattern due to the sarcomeric structure is less pronounced in the caffeine average is on one hand due to dye quenching induced by caffeine (see Fig. 5.7 A), on the other hand due to the more arbitrary location of the maximum fluorescence (and hence the source) with respect to the periodic fluorescence pattern of the studied fiber, whereas events in reference mostly occurred in a ´valley´ of baseline fluorescence.

The resulting spatially and temporally resolved free Ca^{2+} ion concentration and Ca^{2+} release flux from the SR under the two conditions were calculated assuming a Fluo-4 concentration of 60 µM as set by the solution. They are given in the middle and at the bottom of Fig. 5.9 respectively, both having a little higher peak values in caffeine than in reference, indicating that the increase in morphological spark parameters are at least partially due to an increase in Ca^{2+} release flux from the SR. In $\left[Ca^{2+}\right](x,t)$ two spatial components can be seen, one being as sharp and tall as in the calculation for voltage-clamped cut fibers in section 5.2.1, the other looking broad and more flat. These two components can also be seen in the spatio-temporal 3D-representations of Fig 5.8, however they do not appear in the spatially and temporally resolved Ca^{2+} release flux. The spatial width of the calculated spatially and temporally resolved Ca^{2+} release flux was similar under both conditions, but Ca^{2+} ions were released for a longer duration when caffeine was present (blue colored top view). Again the corresponding Ca^{2+} ion current of a point source that is necessary to produce the observed Ca^{2+} release flux density was calculated as described in section 4.4.6. The maximum Ca^{2+} ion current with time was 4 pA for the caffeine and 2.3 pA for the reference condition, where a radius of 0.68 µm (5 pixels) was used as a border for the integration.

5.2.3 The Ca^{2+} spark and its ember

Two modulations of Ca^{2+} release from the SR that interfere with CICR have been presented in section 5.2.1 and 5.2.2 and a quantitative analysis of the effect of high intracellular [Mg^{2+}] and caffeine has been given. There are more important differences between Ca^{2+} sparks in the considered conditions that are presented in this chapter. The same experiments presented in section 5.2.1 and similar experiments to those shown in section 5.2.2 have led to the discovery of a new release form compared to the Ca^{2+} spark: the ember.

In Fig. 5.10 four averages of Ca^{2+} sparks and their projections obtained under different conditions are given, including one condition, that has not been introduced yet. The average marked 'caffeine' was constructed from Ca^{2+} sparks recorded in voltage-clamped cut fibers under 'reference' condition (same as reference in 5.2.1) with an additional caffeine concentration of 0.5 mM. This induced also some spontaneously occurring events as shown in section 5.2.2, but these were not analyzed as they occurred at a very low frequency, as the intracellular [Mg^{2+}] was 0.61 mM and not 0.4 mM as in experiments with chemically skinned fibers. The Ca^{2+} sparks included in the average in Fig. 5.10 were elicited during a step depolarization, thus they were triggered by voltage, although at a lower depolarization voltage than in reference, as otherwise the frequency of sparks in the image was too high to analyze them, because they overlapped. The average marked 'spontaneous' was obtained from Ca^{2+} sparks in chemically skinned fibers under similar conditions as shown in section 5.2.2, except that they were measured with the Biorad setup as all other Ca^{2+} sparks presented in Fig.5.10. The average marked 'high Mg^{2+}' is the average from Fig. 5.5 under 7.0 mM [Mg^{2+}].

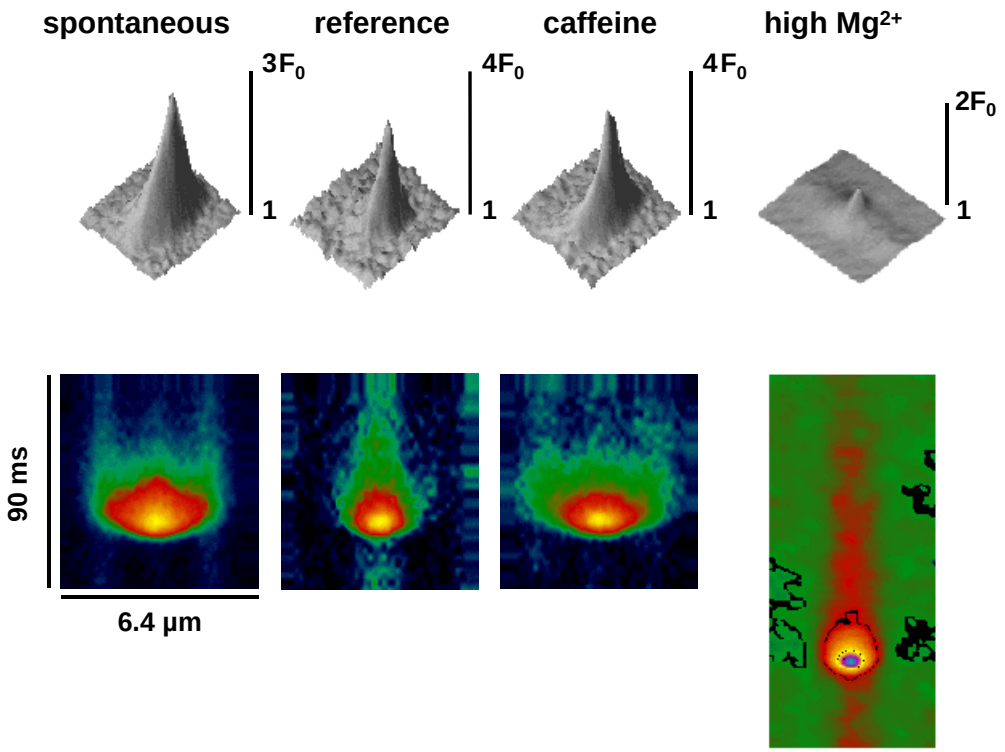

Fig. 5.10 Ca^{2+} spark averages and their projections obtained in four different conditions denoted on top. The spontaneous and the caffeine average look very similar. In the reference and even more in the high Mg^{2+} average a low intensity prolongation at the spatial core of the spark average due to voltage-operated release is observable. In parts from González et al. (Kirsch) [2000b].

The spontaneous and the caffeine average look very similar. Both being wider than the reference and both rising from and falling rapidly back to same fluorescence before and after

the spark. But something else appears in reference when one looks at the projections. The fluorescence decays not as fast after the spark as in the other two cases. There is a low intensity prolongation at the spatial core of the spark average. In the high Mg^{2+} average this low intensity prolongation at the spatial core is even more pronounced than in reference.

One difference between the conditions is the contribution of voltage to release. In spontaneous events, where the fibers are permeabilized, the voltage sensor should be inactivated and not contribute to openings of ryanodine receptors. In caffeine lower voltages than in reference were used to induce sparks and the averages under these two conditions look very similar. Just as the voltage is increased more to induce sparks in reference this feature becomes visible and as under high intracellular [Mg^{2+}] it is possible to depolarize to even higher voltages, the contribution of voltage-operated release in the generation of an elementary Ca^{2+} release event is even more enhanced. Apparently, it is voltage-operated release that produces the long lasting fluorescence decays in spark averages.

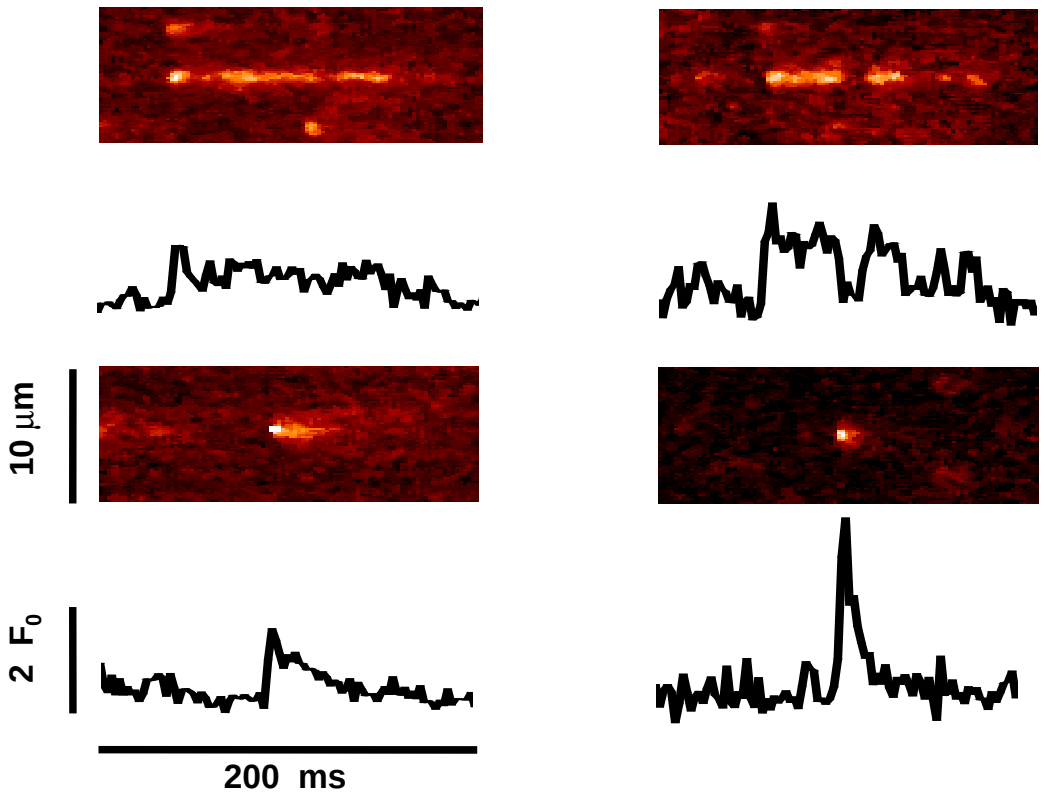

Fig. 5.11 Long lasting events in 7.0 mM intracellular [Mg^{2+}]. A typical Ca^{2+} spark, together with the time course of fluorescence through its maximum is shown on the bottom right. The other three events exhibit longer durations than a typical spark and are thought to contain higher contributions of directly voltage-operated release. From González et al. (Kirsch) [2000b].

Individual long lasting Ca^{2+} release events can be observed in line scan images under high [Mg^{2+}] conditions as shown in Fig. 5.11. A typical Ca^{2+} spark, also obtained in high [Mg^{2+}], which is similar in its morphological parameters to sparks in reference, is shown in the bottom

right image. The time courses of fluorescence of the other events, which are shown below the respective image part, are very different from that of a typical Ca^{2+} spark. These new type of events is thought to be mainly generated by directly voltage-operated release. Based on these experiments a new classification for elementary Ca^{2+} release events has arisen. Ca^{2+} release events that are only due to directly voltage-operated release have been termed embers [González et al. (Kirsch), 2000b].

5.3 Nanodomain Ca^{2+} release in mammalian muscle

This is the first time that elementary Ca^{2+} release events are presented in abundance in adult mammalian muscle. This was accomplished using chemically skinned fiber preparations in conjunction with the mouse internal solution. The frequency of the events was lower than in amphibian muscle, but still high enough to record hundreds of events within one fiber. Fig. 5.12 shows a selection of xy-scans acquired in a time series of 100 images with a time interval of 2 s. The upper panel corresponds to an experiment with a single adult mouse EDL fiber, the lower panel to an experiment with a single adult rat EDL fiber. This figure clearly shows that elementary Ca^{2+} release events exist in adult mammalian muscle.

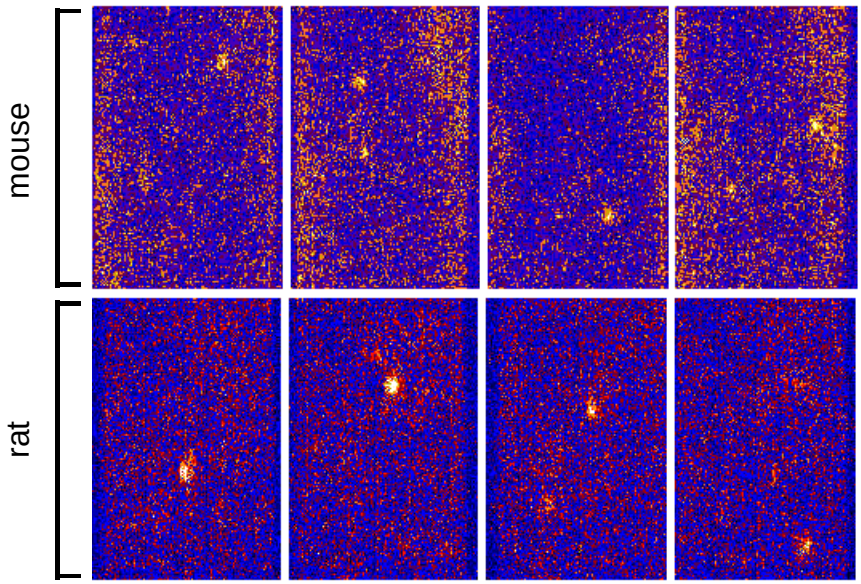

Fig. 5.12 Elementary Ca^{2+} release events in adult mammalian muscle. The images are selected from a time series of 100 xy-scans that were acquired every 2 s. The upper panel shows data from adult mouse EDL and the lower panel from adult rat EDL muscle.

It was no rarity to acquire 3-4 events within one xy-scan, however this frequency is still so low, that line scan images usually contained no more than 2-3 events and mostly only 1 or none. The difference in frequency of events between amphibian and mammalian muscle in

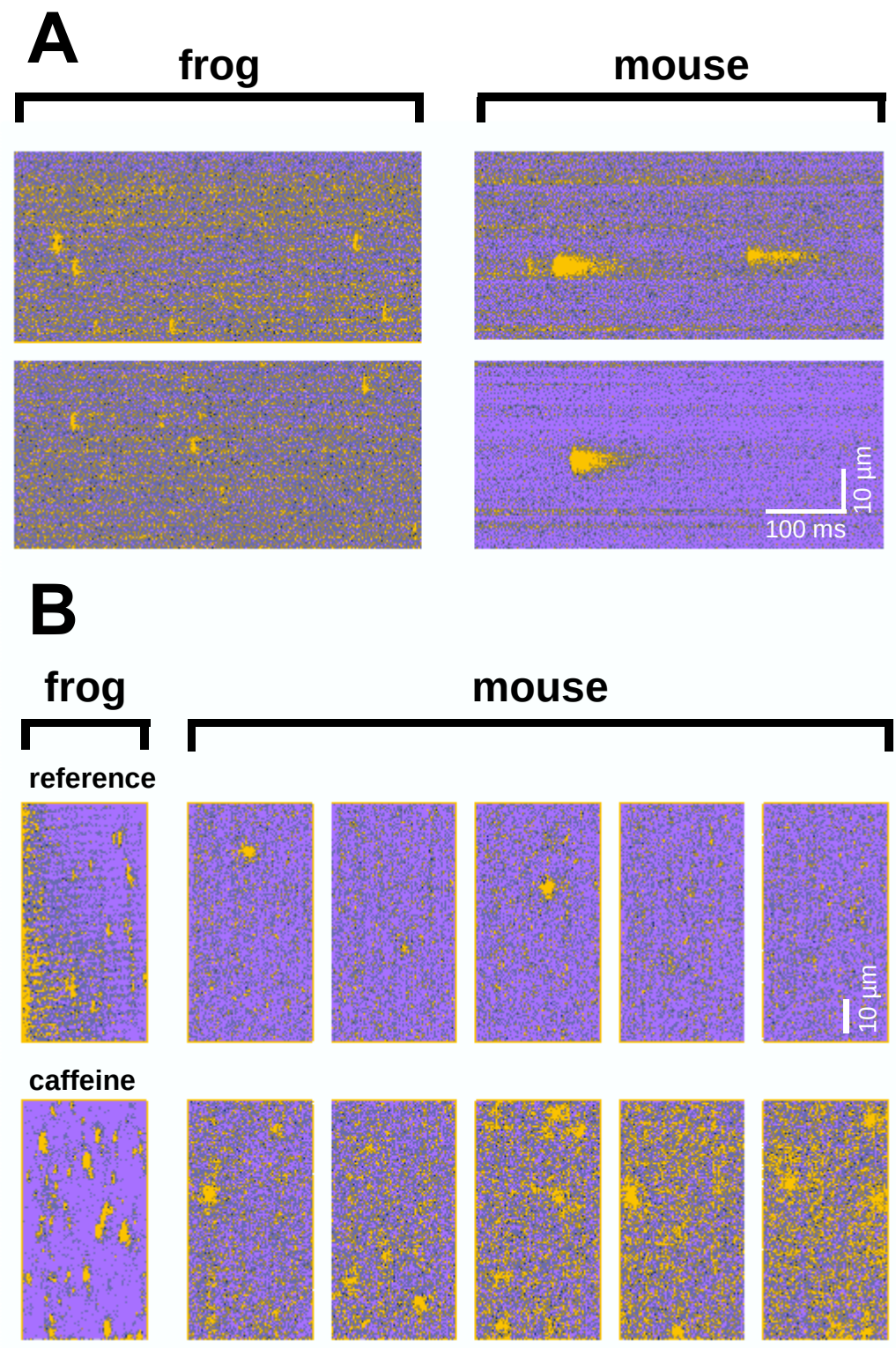

Fig. 5.13 **A** Typical line scan images (70 µm x 2 s) in amphibian and mammalian muscle. Amphibian Ca^{2+} sparks are more frequent and shorter in duration than events in adult mammalians. In addition, mammalian Ca^{2+} release events could exhibit much greater values for the FWHM. **B** The application of 0.5 mM caffeine caused an increase in event frequency in amphibians as well as in mammalians. The images shown are xy-scans and in case of the mouse are selected from a time series containing of 100 images acquired every 2 s.

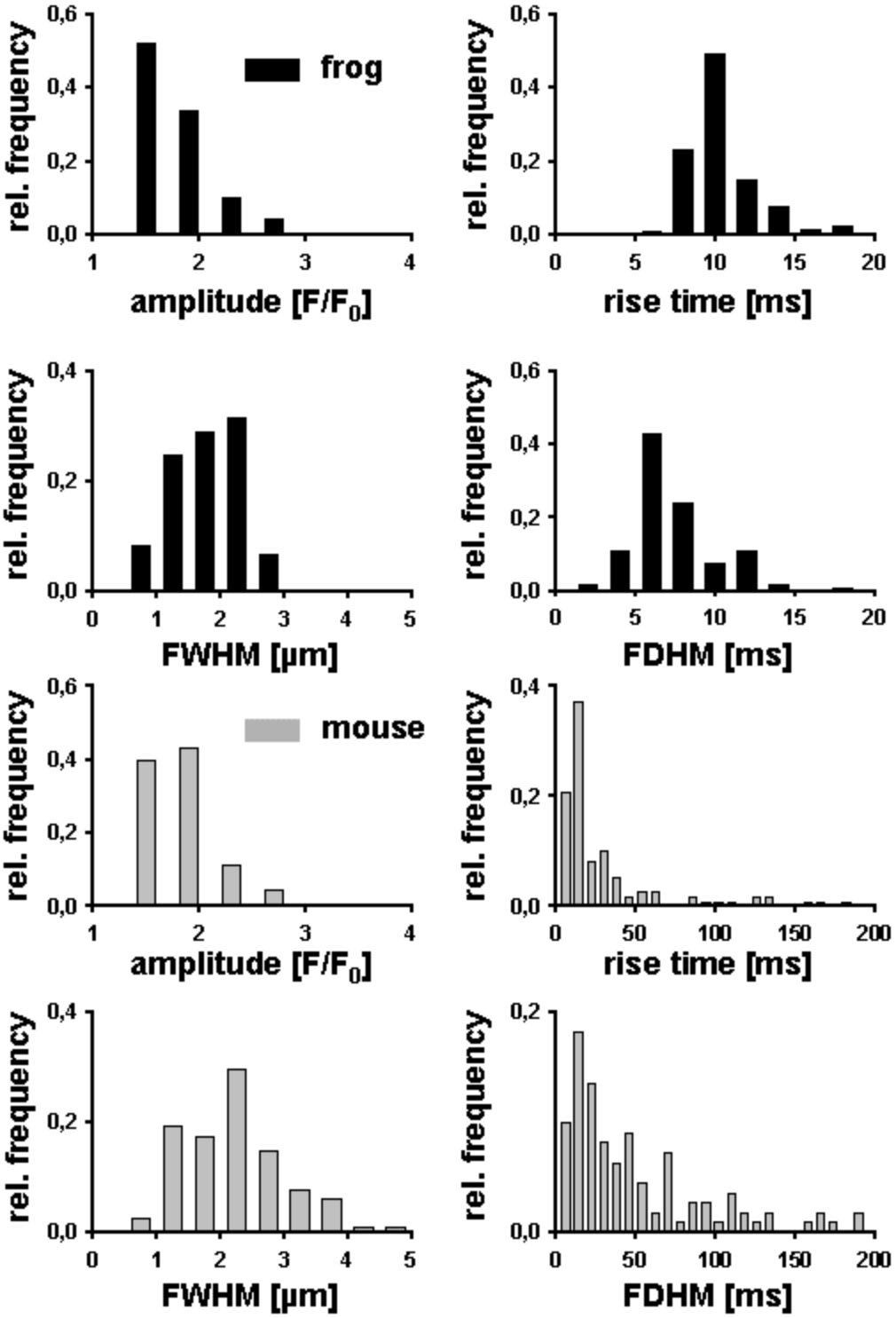

Fig. 5.14 Comparison of the morphological event parameters obtained in one mammalian fiber and one amphibian fiber. Adult mammalian Ca^{2+} release events had similar amplitudes, but greater values for the FWHM than amphibians. The most striking difference is in the rise time and the duration, were adult mammalian events could exhibit 10 fold higher values.

line scan images is shown in Fig. 5.13 A. In amphibians, there were always at least 3-4 events in a line scan (70 µm x 2 s). It was tested, if the frequency of events could be altered by the variation of intracellular [Mg^{2+}], but the results scattered so much, that no clear answer to this question was found, except that Ca^{2+} sparks are basically present in every mammalian muscle fiber. Another difference becomes clear by looking at the two line scans from each animal species in Fig 5.13 A. The elementary Ca^{2+} release events of mammalians in these images exhibit much longer durations and greater widths than the amphibian Ca^{2+} sparks.

Panel B of Fig. 5.13 shows the effect of 0.5 mM caffeine on the event frequency. Two xy-images for amphibian muscle are given on the left hand side for comparison, one under reference condition and one in caffeine, showing an obvious increase in spark frequency. The images for adult mouse muscle under both conditions are again selected from a time series of 100 xy-scans acquired every 2 s. Five representative images before and after the application of caffeine show the increase in event frequency. This was accompanied by an increase in resting fluorescence due to the channels opened by caffeine. Therefore, the increased number of events is the result from both, the increased affinity for the activation site on the RyR due to caffeine and the additional effect of a higher resting free calcium concentration that can more easily activate RyRs. Nevertheless, this result on the effect of caffeine shows that RyRs in mammalians are susceptible to CICR.

In Fig. 5.14 the morphological parameters of adult mammalians are compared to those of adult amphibians under similar conditions. Note that all the events in this figure were recorded from the same fiber, while similar data was obtained in 6 other fibers. The distribution of amplitudes is basically identical, but already the values for the FWHM show significant differences. Events in adult mammalians could show values of FWHM of up to 5 µm, a width that was never observed for an amphibian Ca^{2+} spark. The most striking difference is found in the parameters for rise time and FDHM. Elementary Ca^{2+} release events could exhibit rise times and durations of more than 150 ms. This time dependence reminds the recently defined ember event.

In Fig. 5.15 a number of adult mammalian elementary Ca^{2+} release events from one fiber are depicted to emphasize the broad spectrum in the observed morphology. In their time course the events are as non-stereotyped as they can be, ranging from typical spark-like shapes with a fast rise and a somewhat slower decay to very long and flat shapes that look more like the mainly voltage-operated release events in intracellular high [Mg^{2+}] already shown (see Fig. 5.11) and thus constitute a more ember-like form of elementary Ca^{2+} release. Also, event shapes that correspond to mixes of the two basic classes were observed, like the one marked with the white circle for which the time course of fluorescence definitely consists of two components. Thus ember-like and spark-like Ca^{2+} release can coexist within one event.

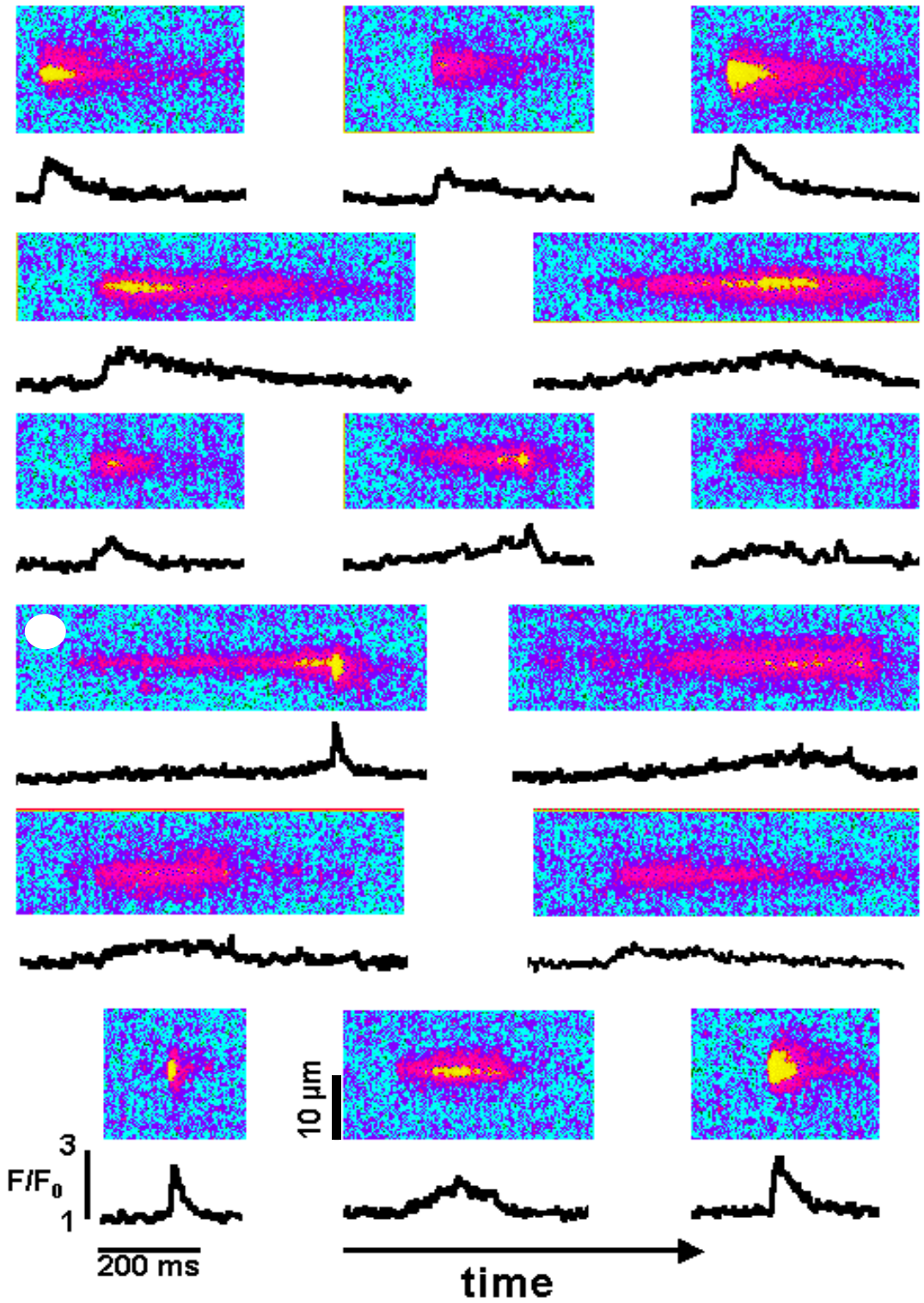

Fig. 5.15 Elementary Ca^{2+} release events in adult mammalian muscle show a great variety in morphology. The images shown correspond all to the same fiber and depict the normalized image areas of individual events computed with the IDL program FLASH (see section 4.4.3). Below the events are the respective time courses of fluorescence through the maximum of the elementary Ca^{2+} release event.

6 Discussion

The biophysical goal of this study was to establish and apply methods to measure and quantify the micro- and nanodomain Ca^{2+} release in skeletal muscle fibers. As the project was embedded in a physiological context, it was also possible with this work to answer questions of high interest in current medical research. In this section the obtained results will be summarized, interpreted and put into context.

The results on microdomain Ca^{2+} release show that the average free Ca^{2+} ion concentration rises to several µM at the peak and that the corresponding Ca^{2+} release from the SR could rise above 100 mMs^{-1} in reference. Similar values have been obtained by other scientists [Baylor et al., 1998; Garcia et al., 1993] and this was basically measured and calculated to have the reference points for the comparison with the measurements in high intracellular $[Mg^{2+}]$.

Ca^{2+} release from the SR in skeletal muscle fibers with intracellular free Mg^{2+} ion concentrations of up to 7.0 mM has never been measured before. The quantitative results on the peak rates of release and the steady values obtained from five fibers (table 5.1) scattered very much in absolute values as well as in the relative reduction by high intracellular $[Mg^{2+}]$. This could be on one hand attributed to the different quality of the fiber preparations, but on the other hand also on errors in the measurement of the necessary experimental constants, like the intrinsic absorption, the path length and the dye concentration. However, it became clear through these measurements that still a substantial amount of Ca^{2+} ions is released in such high values of intracellular $[Mg^{2+}]$. Other than the absolute number of the peak release rate, the relative magnitude of the ratio of peak over steady value was very stable in all experiments, showing that the principal time course of the calculated Ca^{2+} transients and Ca^{2+} release records was well conserved and not a great subject of error. This allows drawing of some interesting conclusions from the microdomain experiments. The experiments were designed to interfere with CICR during the release process, as the increased amount of free Mg^{2+} ions would basically occupy all Ca^{2+} activation sites on the RyRs. Therefore, the expected result would have been a complete elimination of the peak of release, which is thought to be generated by the transient opening of the RyRs that are not coupled to DHPRs. The obtained results show that there is a reduction of the peak of release at intermediate voltages. But even more interesting is that the ratio of peak over steady value was basically unaltered at depolarizations greater than 0 mV. The voltage dependence of the ratio of peak over steady value became monotonic and looked then very similar to that measured in mammalian muscle [Kirsch et al., 1999; Shirokova et al., 1996b]. This indicates, in general,

that there probably exists a different mechanism to generate part of the peak of release than pure CICR.

Using confocal laser scanning microscopy the measurement of elementary Ca^{2+} release events in amphibians, which have just recently been discovered [Tsugorka et al., 1995], was accomplished. Due to the brief nature of these events, lasting only around 10 ms, they could only be resolved in line scanning mode. As this field is still new and of high interest in biophysics and physiology, there are still very basic questions that are unresolved. One of the most important questions is, if these events are generated by the opening of a single RyR or rather by the combined opening of the whole or part of the cluster of RyRs [Shirokova et al. (Kirsch), 1999b] that is given by the structural setup of the triadic junction, which has been shown to constitute the primary release sites of Ca^{2+} release from the SR [Escobar et al., 1994].

Therefore, with the specific goal to find answers on the nature of the Ca^{2+} release mechanism two conditions that interfere with CICR, the possible mechanism for channel cluster activation, have been investigated. In experiments on nanodomain Ca^{2+} release from the SR in amphibian muscle, analogous to the microdomain experiments, a high intracellular [Mg^{2+}] was used to decrease the contribution of CICR to the generation of Ca^{2+} sparks and thereafter, a low dose of caffeine was applied, which is known to promote CICR.

The results show that a high intracellular [Mg^{2+}] decreased the frequency of Ca^{2+} sparks under voltage clamp. More remarkably, the average amplitude and FWHM of the Ca^{2+} spark were reduced, thus by antagonizing CICR the produced fluorescence signal could be decreased. Note here that this decrease in spark parameters was measured in a normalized fluorescence image, therefore any decrease in absolute fluorescence due to binding of Mg^{2+} ions to the dye (and thus less available dye to bind to Ca^{2+} ions) would have a similar effect on the resting fluorescence and would therefore be canceled out by the normalization. Hence, the results on high [Mg^{2+}] the contribution of CICR to the production of an elementary Ca^{2+} release event.

The application of 0.5 mM caffeine to the internal solution under reference condition in chemically skinned fibers yielded an increase in morphological spark parameters [Kirsch et al., 2000a]. Again any effect that alters the absolute fluorescence, like quenching of the dye, is canceled out by the normalization of the image to its baseline fluorescence. As caffeine is an agonist for the action of CICR, the increased morphological parameters show the contribution of CICR in the generation of Ca^{2+} sparks.

The changes in morphology alone yield strong arguments for the multi-channel character of Ca^{2+} sparks. Still, more has to be said on possible side effects. For example, Mg^{2+} ions could cause a so-called open channel block [Hille B., 1992], where the comparable divalent character to Ca^{2+} ions leads to the occupancy of the pore by Mg^{2+} ions and thus to a block of Ca^{2+} ion flux through the channel until the Mg^{2+} ions leave the pore again. Then an increased concentration of free Mg^{2+} ions would lead to a higher probability for open channel block. For this reason we have applied caffeine also under the high [Mg^{2+}] condition and the results

show a substantial reversibility, therefore at least a substantial part of the effect of high [Mg^{2+}] has to be due to CICR, otherwise it could not be reversed by caffeine.

The morphological shape of the fluorescence that is produced be elementary Ca^{2+} release form the SR is dependent on the diffusible buffers inside the cell. The elevated free Mg^{2+} ion concentration leads to higher occupancy of the Mg^{2+} ion dependent diffusible buffers, like ATP and parvalbumin. For instance, it has been shown that binding of Ca^{2+} ions to ATP is responsible for an increased spatial extension of Ca^{2+} sparks [Baylor et al., 1998]. Therefore, part of the narrowing of the FWHM in high [Mg^{2+}] could be attributed to an increased occupancy of diffusible buffers by Mg^{2+} ions. In the calculation of Ca^{2+} release flux from the SR this effect is taken into account, as the binding of Mg^{2+} to ATP and parvalbumin is included in the computation.

The calculation of the spatially and temporally resolved free Ca^{2+} ion concentration and the underlying Ca^{2+} release flux showed that the in- or decrease of the measured normalized fluorescence signals was in fact due to a true in- or decrease in the amount of Ca^{2+} ions released from the SR. This constitutes the quantitative confirmation of the previously discussed results. In addition, the volume integral of the region that showed the highest Ca^{2+} release flux density (usually a radius from the center of the source of around 0.7 µm) was calculated to estimate the current through a point source that would be necessary to produce the observed Ca^{2+} release flux. The values obtained were 9.3 pA and 3.9 pA under reference and high intracellular [Mg^{2+}] conditions in voltage-clamped cut fibers as well as 4 pA and 2.3 pA before and after application of caffeine under reference conditions in chemically skinned fibers. The obtained values are all by far greater than the maximum single channel current of 0.4 pA for a RyR, measured under comparable ionic compositions of the solutions by Mejia-Alvarez et al. [1999]. This again evidence for the involvement of multiple channels in the production of a Ca^{2+} spark. Therefore the elementary events in skeletal muscle correspond to the activation of the whole or part of the clusters of RyRs located at the triadic junctions.

The calculations of the spatially and temporally resolved free Ca^{2+} ion concentration and the underlying Ca^{2+} release flux were all performed with parameters that yield low estimates for [Ca^{2+}] and release. For instance, the ratio of maximal to minimal fluorescence for Fluo-3 and Fluo-4 were chosen to be 100 and 150 in the respective calculation, while in calibrations this value was around 64 for Fluo-3 and about 100 for Fluo-4. In addition, the dissociation constant for Fluo-3 in the cytoplasm was chosen to be more than twice as high as known from simple salt solutions [Harkins et al., 1993]. This supports the finding that a single RyR cannot generate an average Ca^{2+} spark.

In the experiments with caffeine in chemically skinned fibers given in section 5.2.2, the calculated $\left[Ca^{2+}\right](x,t)$ exhibits two spatial components, one being as sharp and tall as in the calculation for voltage-clamped cut fibers in section 5.2.1, the other looking broad and more flat. These two components can also be seen in the spatio-temporal 3D-representations of

Fig 5.8 and are therefore not a result of the calculation or deblurring algorithm. Rather, they are a result due to the averaging procedure, as individual events under these conditions seem to be more skewed into one of the two spatial directions. However, these two components have not appeared in the spatially and temporally resolved Ca^{2+} release flux. This means that the calculation procedure is dominated by the peak values at the center of the Ca^{2+} spark (only the center region was used for the determination of the point source current). It also shows that the spatial shape of the free calcium concentration needs not to be well correlated with the spatial shape of the source.

The studies under the conditions that were designed to interfere with CICR have led to the conclusion that clusters of RyRs are involved in Ca^{2+} sparks. This allowed the study of the release units under different contributions of CICR and hence under different contributions of RyRs that are directly activated by DHPRs through changes in voltage. This resulted in the discovery of a new Ca^{2+} release event form: the ember [González et al. (Kirsch), 2000b; Kirsch et al., 2000b]. Embers are best seen under high depolarization conditions, where CICR is greatly reduced due to high [Mg^{2+}] and they are less or not present, when CICR is the main contributor to local Ca^{2+} release due to caffeine or the inactivation of the voltage sensor in permeabilized fibers.

Therefore, the ember has been defined as the fluorescence signal produced only through Ca^{2+} release by voltage-operated RyRs. All the results on nanodomain Ca^{2+} release in amphibians presented in this work can than be explained by the combined action of two basic classes of release forms with very different kinetics: the ember and the spark, one being the result of directly voltage-operated release, the other being generated by the concerted opening of multiple channels via the feed-back mechanism CICR.

For the first time this work has shown that elementary Ca^{2+} release events can be measured in abundance in adult mammalian muscle fibers. The frequency of the events was lower than in amphibians, which is in agreement with the hypothesis - based on the voltage dependence of the ratio of peak of release over steady value [Shirokova et al., 1996b] - that Ca^{2+} release in mammalians is less based on CICR and more under voltage control. However, as the experiments were carried out in chemically skinned fibers, where the external membrane is depolarized and the DHPRs should be inactivated, there must be a contribution by CICR as elementary Ca^{2+} release events can be evoked under this condition. The increased frequency of events upon application of caffeine presented in this work and, in general, the possibility of caffeine induced Ca^{2+} release in skinned fiber preparations [Uttenweiler et al., 1998] and RISC experiments [Suda. et al, 1994] in voltage-clamped cells are further indications that the events are modulated by CICR.

In contrast to Ca^{2+} sparks in amphibian muscle, the elementary Ca^{2+} release events of adult mammalians exhibit a great variety in morphology. The most striking differences found were the greatly increased rise times and durations. Sometimes, the time course of elementary Ca^{2+} release had two distinguishable components. From these findings the descriptive picture emerged that all the morphological variety could just be based on the combined action of a

slow and a fast form of Ca^{2+} release. As the slow component reminded of the long lasting events in high intracellular [Mg^{2+}], which were found to correspond to embers, this slow Ca^{2+} release component was termed to be ember-like. Whether the long lasting events really are embers, needs further clarification, as embers are defined by their mechanism and not by their morphology. In a very strict sense, the long events in mammalian muscle must not be embers, as they are defined as voltage-operated release events and presumably there is no voltage as the external membrane is depolarized. Still, the long events could be influenced by the still in some way connected DHPRs, which could be a reason for the slowed kinetics.

After this series of successful experiments it should be mentioned that skinned fiber preparations are found to be a very good tool to study elementary Ca^{2+} release events and their dependence on ligands in the solution. The two main reasons for this are, firstly, the almost ideal control of the intracellular ionic composition and, secondly, the simple setup of the technique that saves valuable time compared to the voltage-clamped cut fiber preparations. The main disadvantage is the lack of voltage control and thus the lack of a defined state of the DHPRs.

7 Appendix

7.1 IDL source codes

7.1.1 The program FLASH

```
pro flash
;Program to determine the morphology of sparks (skinned mice,skinned frogs).
;Allows selecting a part of pulse region (xmin,xmax)
;Date of last modification :                    08.07.2000
;author Wolfgang Kirsch

pixelx=0.1365                                  ;spatial resolution in x direction

fnama=''                                       ;read variable
dummy=''                                       ;read variable
err=1                                                  ;file reading error flag
endprogram=0                                   ;flag for program termination
keepimage=0                                    ;flag for working on same image
sparkfile=fltarr(6,50)              ;will contain the spark parameters
timefile=fltarr(50,1000)            ;will contain time courses of fluorescence
fwhmfile=fltarr(50,1000)            ;will contain cut in x throgh maximum
sparkfile(*,*)=0                           ;initialization
timefile(*,*)=0
fwhmfile(*,*)=0

while (endprogram eq 0) do begin    ;main program loop

while (err ne 0) do begin                  ;loop for image file reading
  read, fnama, prompt='Enter input file,( no ext., default .tif): '
  fname='d:\991013\'+fnama+'.tif'
  ;fname='e:\991004\export\faser01\'+fnama+'.tif'
  openr,ur,fname,error=err,/get_lun ;actual strat of file reading
  if (err eq 0) then begin
    free_lun,ur
    ima=tiff_read(fname)
    close,ur
    keepimage=1                            ;keep this image for first analysis
  endif else begin
  print,'uncorrect filename'
  endelse
endwhile
err=1

loadct,0                                       ;load bw-colortable
tscan=2.0                                      ;time resolution
t=size(ima)&nx=t(1)&ny=t(2)         ;determin image size
```

```
y=float(ima)
print, 'sample time=', ny*tscan, ' milliseconds'
window,0,xs=ny,ys=nx,xpos=0,ypos=0

ynofilter=y                    ;this will be unfiltered image
y=median(y,3)                  ;no filtering (other than the median,3) >---
wset, 0                                ;---> only in visual image, not in processed image(ynofilter)
yyyy=y                                 ;rotated screen display routine
roty=rotate(y,3)
tvscl,roty
y=yyyy

;***selection of baseline regions for visual proof that spark is bigger than 3*sd***

print,'Select baseline region with cursor (no sparks in selection)'
cursor, x, wy, /device, /down   ;cursor points have to be selected first up/left then down/right
cursor, x1, wy1, /device, /down
xmin=512-wy
xmax=512-wy1
nbl=x
nnbl=x1
plots, [x1,x], [wy1,wy], /device;plots white line connecting the two selected points
print,'pulse region:',xmin,xmax,' pixel / ', nbl,nnbl,' ms '

;first normalization with averaged baseline fluorescence

yn=y                                           ;contains at the end the selected normalized region
ybl=yn(xmin:xmax,nbl:nnbl)             ;the selected region in image
ybln=yn(xmin:xmax,*)/rebin((rebin(ybl,xmax-xmin+1,1)),xmax-xmin+1,ny+1)       ;normalization
sd=stdev(ybln(0:xmax-xmin,nbl:nnbl),mean)      ;standard deviation
mask=ybln
dubb=where(mask(*,*) gt mean+3*sd)             ;gets all points gretaer than 3*sd
mask(dubb)=0                                   ;gives these points zero (will be displayed as black)
yn(xmin:xmax,*)=mask                   ;insert the part with normalized (F/F0) into yn

wset,0
yyyy=yn
roty=rotate((((yn-.7>0)*3500)<4096),3) ;enhancing the range for better display
tvscl,roty
yn=yyyy
read, prompt='everything bigger than 3*SD is black....(press return)  ', dummy

;***now real analysis***

count=0
while keepimage eq 1 do begin                  ;analyze within this image
window,0,xs=ny,ys=nx,xpos=0,ypos=0

yyyy=y
roty=rotate(y,3)                ;show original picture again
tvscl,roty
y=yyyy

print, 'select first baseline region before spark (up/left then dpwn/right)'
cursor, x, wy, /device, /down
;print, x, wy
cursor, x1, wy1, /device, /down
;print, x1, wy1
b1xmin=512-wy
b1xmax=512-wy1
b1ymin=x
b1ymax=x1
```

```
plots, [x1,x], [wy1,wy], /device

print, 'select second baseline region after spark (up/left then dpwn/right)'
cursor, x2, wy2, /device, /down
;print, x2, wy2
cursor, x3, wy3, /device, /down
;print, x3, wy3
b2xmin=512-wy2
b2xmax=512-wy3
b2ymin=x2
b2ymax=x3
plots, [x3,x2], [wy3,wy2], /device

ymax=min([wy2,wy])
ymin=max([wy3,wy1])
bxmax=512-ymin
bxmin=512-ymax


plots, [x3,x], [ymax,ymax], /device       ;plotslines around the baseline regions >--
plots, [x3,x], [ymin,ymin], /device                ;---> and the ROI in between
plots, [x3,x3], [ymax,ymin], /device
plots, [x1,x1], [ymax,ymin], /device
plots, [x2,x2], [ymax,ymin], /device
plots, [x,x], [ymax,ymin], /device

print,'spark region:',bxmin,bxmax,' pixel / ', b1ymax,b2ymin,' ms '

b1arr=y(bxmin:bxmax,b1ymin:b1ymax)                ;is baseline region 1 in original FILTERED image
b2arr=y(bxmin:bxmax,b2ymin:b2ymax)                ;is baseline region 2 in original FILTERED image
b1arrnf=ynofilter(bxmin:bxmax,b1ymin:b1ymax)      ;is baseline region 1 in original UNFILTERED image
b2arrnf=ynofilter(bxmin:bxmax,b2ymin:b2ymax)     ;is baseline region 2 in original UNFILTERED image

basel=((b1ymax-b1ymin+1)*rebin(b1arr,bxmax-bxmin+1,1)$  ;averages and compresses region 1 and 2
+(b2ymax-b2ymin+1)*rebin(b2arr,bxmax-bxmin+1,1))$       ;(FILTERED)
/((b1ymax-b1ymin+1)+(b2ymax-b2ymin+1))

baseline=rebin(basel,bxmax-bxmin+1,b2ymin-b1ymax+1)     ;decompression to size of sparkregion
sparknor=y(bxmin:bxmax,b1ymax:b2ymin)/baseline          ;normalize sparkregion (FILTERED)

baselnf=((b1ymax-b1ymin+1)*rebin(b1arrnf,bxmax-bxmin+1,1)$ ;averages and compresses r1 and r2
+(b2ymax-b2ymin+1)*rebin(b2arrnf,bxmax-bxmin+1,1))$        ; (UNFILTERED)
/((b1ymax-b1ymin+1)+(b2ymax-b2ymin+1))

baselinenf=rebin(baselnf,bxmax-bxmin+1,b2ymin-b1ymax+1)   ;decompression to size of sparkregion
sparknornf=y(bxmin:bxmax,b1ymax:b2ymin)/baselinenf        ;normalize sparkregion (UNFILTERED)

;***detection of spark maximum***

sparkmatrix=sparknor                                      ;renaming
sparkmatrixnf=sparknornf

for n=1,b2ymin-b1ymax-1 do begin                          ;routine to average 3 pixeks only in x direction
      for j=1,bxmax-bxmin-1 do begin
            result=0
            for xmat=-1,1 do begin
                  result=result+sparknor(j+xmat,n)
            endfor
            sparkmatrix(j,n)=result/3                     ;save this averaged pixels in sparkmatrix
      endfor
endfor
```

```
maxamp=max(sparkmatrix,k)                                   ;the amplitude of the (twice) filtered spark
kk=size(sparkmatrix)
maxposx= k mod kk(1)                                        ;the x position of the spark within sparkregion
maxposy= k/kk(1)                                            ;the y position of the spark within sparkregion

timec=sparknor(maxposx-1:maxposx+1,1:b2ymin-b1ymax-1)       ;take time course of 3 pixels
timecourse=rebin(timec,1,b2ymin-b1ymax-1)                   ;make it one-dimensional

timecnf=sparknornf(maxposx-1:maxposx+1,1:b2ymin-b1ymax-1)   ;same for UNFILTERED image
timecoursenf=rebin(timecnf,1,b2ymin-b1ymax-1)
maxamp2=max(timecoursenf)                                   ;amplitude of the only by rebin filtered spark

sparkfluotrace=sparkmatrix-0.5                              ;scaling for nice colorful traces for power point
sparkmatrix(maxposx-1:maxposx+1,maxposy-1:maxposy+1)=0      ;max of spark black in sparkregion
y(bxmin+maxposx-1:bxmin+maxposx+1,$                         ;mark spark in current image
b1ymax+maxposy-1:b1ymax+maxposy+1)=0

sparkposx=bxmin+maxposx
sparkposy=b1ymax+maxposy                                    ;spark positions in image
print,maxamp,maxamp2,sparkposx,sparkposy

window,0,xs=ny,ys=nx,xpos=0,ypos=0                          ;display image with all marked sparks
yyyy=y
roty=rotate(y,3)
tvscl,roty
y=yyyy

loadct,4                                                                ;load color table
u=size(sparkmatrix)

window,1,xs=u(2),ys=u(1),xpos=0,ypos=560      ;window for sparkregion
yyyy=sparkfluotrace                                                     ;coloful display of spark image
roty=rotate(yyyy,3)
roty=round(roty*102)
tv, roty
sparkfluotrace=yyyy

window,2,xs=250,ys=150,xpos=490,ypos=560, title='time course'  ;window for time course
plot,timecoursenf, background=255, color=0                              ;make normal xy-graph
l=size(timecoursenf)
print, l(2)
linie=fltarr(l(2)-9)

window,3,title='profile at FWHM',xs=250,ys=150,xpos=750,ypos=560 ;window for FWHM

;***get FWHM, FDHM and rise time***

fwhmlinie=sparknornf(*,maxposy)                             ;get cut in x through max
jj=size(fwhmlinie)
print, jj(2)
plot, fwhmlinie, background=255, color=0                                ;plot it as xy.graph
bla=where(sparknornf(*,maxposy) ge ((maxamp-1)/2)+1,number)
fwhm=number*pixelx
      ;this is FWHM

bla=where(sparknornf(maxposx,*) ge ((maxamp-1)/2)+1,number)
fdhm=number*2                                               ; this is FDHM at 2 ms resolution

tenpercent=((maxamp-1)/10.)+1
ii=0
while ((maxposy-ii) gt 0) and (abs(timecoursenf(maxposy-ii)) gt abs(tenpercent)) do ii=ii+1
risetime = (ii+1)*2                                         ; this rise time at 2 ms resolution
```

```
;***output of parameters***

print,'maximum amplitude :', maxamp2,'   FWHM :', fwhm,'   FDHM :', fdhm,'   rise time :',risetime

read, prompt='Should spark be saved   (y/n) ?   ', dummy
if dummy eq 'y' then begin                                        ;if yes then store all 6 parameters
  sparkfile(0,count)=sparkposx
  sparkfile(1,count)=sparkposy
  sparkfile(2,count)=maxamp
  sparkfile(3,count)=risetime
  sparkfile(4,count)=fwhm
  sparkfile(5,count)=fdhm
  timefile(count,0:l(2)-1)=timecoursenf                  ;store also the time course
  ;fwhmfile(count,0:jj(2)-1)=fwhmlinie                   ;change here to store cut in x through max
  count=count+1
  endif
read, prompt='press n for new image or s for program to stop   ', dummy
if dummy eq 'n' then keepimage=0
if dummy eq 's' then begin
  keepimage=0                                                     ;setting the flags
  endprogram=1
endif
endwhile                                          ;this loop ends if keepimage is set back to 0

if sparkfile(0,0) ne 0 then begin                 ;saving of parameters under image name
      zong=where(sparkfile(0,*) gt 0,number)
      sparksave=fltarr(6,number)
      sparksave(*,*)=sparkfile(*,0:number-1)
      outnamo=fnama+'par.asc'
      openw,un,outnamo,/get_lun
      printf,un,format='(f7.0,f7.0,f8.2,f6.0,f7.2,f6.0)',sparksave
      free_lun,un
endif
if timefile(0,1) ne 0 then begin                  ;saving of the time course under image name
      zong=where(timefile(*,0) gt 0,number)
      timesave=fltarr(number,1000)
      timesave(*,*)=timefile(0:number-1,*)
      fff='(f6.3'
      for rt=1,number-1 do begin
      fff=fff+',f6.3'
   endfor
   fff=fff+')'
      outnamo=fnama+'tc.asc'
      openw,ua,outnamo,/get_lun
      printf,ua,format=fff,timesave
      free_lun,ua
endif
sparkfile(*,*)=0                          ;prepare for next image
timefile(*,*)=0
fwhmfile(*,*)=0
endwhile      ;this loop ends if endprogram is 1
end           ;end of program
```

7.1.2 The program RELEASE

```
pro release
;deblurring and calculation of release
;Date of last modification of first version: 12.07.99
;Date of last modification : 05.08.00
;Author E. Rios.
;modified by Wolfgang Kirsch

;***definition of variables***

wdelete,1
wset,0
dummy=''
contout=''
outnamo=''
isim=''
isimp='c'
zoom=3.5
laser=1.
gain=1000.
kmax = 1.45
ca0=0.1
sm=0
smm=0
read,sm,smm,prompt='enter two smoothing numbers, 0 or ge 3, separated by comma:'
read,zoom,laser,gain,kmax,ca0,prompt='zoom?(3.5); laser(3); gain(1000), kmax(1.45), ca0(0.1): '
if zoom eq 0 then zoom = 3.5
if laser eq 0 then laser = 3.0
if gain eq 0 then gain = 1000.
if kmax eq 0 then kmax = 1.45
if ca0 eq 0 then ca0 = 0.1

nwi=44                                          ;define different sizes of arrays
nl=768
nwm=nwi-1
nmm=nwi-2
nmmm=nwi-3
nwp=nwi+1
nwb=nwi+16
np8=nwm+8
nwih=fix(nwi/2)
xpo=fltarr(2,48)
caimg=fltarr(nwi,nwp) &  casat=fltarr(nwi,nwp) & img=fltarr(nl,512)
a=fltarr(nl) & xd=findgen(nwi) & td=fltarr(nwi) &
ap=fltarr(4) & ax=fltarr(nwi) & axfit=fltarr(nwi)
atfit=fltarr(nwi) & at=fltarr(nwi) & bb=fltarr(nwi)
relx=fltarr(nwi) & ftot=fltarr(nl) & dyarr=fltarr(nwp,nwp)
dyrr=fltarr(nwi,nwp) & x=findgen(nwi) & z=fltarr(nwp,nwp)
ri=fltarr(nwi,nwp) & dzdt=fltarr(nwi,nwp) & dzdx=fltarr(nwi,nwp)
d2z=fltarr(nwi,nwp) & dcat=fltarr(nwi,nwp) & dcax=fltarr(nwi,nwp)
d2c=fltarr(nwi,nwp)
cae=fltarr(nwi,nwp)                             ;diffusible buffer, slow
cat=fltarr(nwi,nwp)                             ;nondiffusible buffer, fast (''troponin'')
cap=fltarr(nwi,nwp)                             ;ca:pump
capa=fltarr(nwi,nwp)                            ;ca:parvalbumin
mgpa=fltarr(nwi,nwp)                            ;mg:parvalbumin
caat=fltarr(nwi,nwp)                            ;ca:atp
mgat=fltarr(nwi,nwp)                            ;mgatp
rel=fltarr(nwi,nwp)
rem=fltarr(nwi,nwp) & array=fltarr(nwi,nwp) & arrayx=fltarr(2,nwi)
```

```
arrayt=fltarr(2,nwp) & avgarr=fltarr(nwi,nwp) & flav=fltarr(nwp,nwp)
dflav=fltarr(nwp,nwp) & dflave=fltarr(nwp+4,nwp+4)
dyav=fltarr(nwp) & xpos=fltarr(9,250) & dca=fltarr(nwi)
dcae=fltarr(nwi)                                        ;first and second derivatives
d2cae=fltarr(nwi) & dcapa=fltarr(nwi) & d2mgat=fltarr(nwi)
d2capa=fltarr(nwi) & dmgpa=fltarr(nwi) & d2mgpa=fltarr(nwi)
dcaat=fltarr(nwi) & d2caat=fltarr(nwi) & dmgat=fltarr(nwi)

caini=fltarr(nwi)
dbuf=fltarr(nwb) ;differentiation buffers
dbufpa=fltarr(nwb) & dbufmg=fltarr(nwb) & dbufat=fltarr(nwb)
dbufatmg=fltarr(nwb)
eximg=fltarr(124,124)
fdflav=fltarr(nwp)
kernely=fltarr(nwp)
dccd=fltarr(nwi,nwp)
window,0,xs=600,ys=500

; UNITS ARE MICROMOLAR, MILLISECOND, MICRON, PICOAMPERES

;***diffusion coefficients***

dcd=0.02        ;diff. coef. dye. lower estimate (in micron2/ms)
dcc=0.35        ;diff. coef. Ca   lower estimate
dce=0.036       ;diff. coef. eGTA lower estimate
dcatp=0.14      ;diff. coef. ATP,
dcpa=0.026  ;diff  coef. parvalbumin

;***concentrations***

egta=1000
parv=1000
trop=240
pump=200        ;pump sites
atp = 5000
MP = 9.8        ;max pump rate factor (micromolar/millisec)
Mg=610.         ;THIS VALUE IS IMPORTANT.

;***rate constants are in per micromolar per millisecond (multiply the usual /M/s by 10^-9)***

kpon=0.5 & kpof=0.5     ;pump rate constant
kdp=kpof/kpon   ;pump sites Kd (micromolar) use 1
fkd =1.03 & fkon=0.032
                ; faster dye, assuming Baylor numbers in the presence of aldolase (leads to lower Ca).
kde=1. & kone=0.002     ;EGTA dissociation constant and on rate constant
konpa=0.125   & kofpa=0.0005            ;Ca parvalbumin rate constants
konMg=0.00003 & kofMg=0.003             ;Mg parvalbumin rate constants
konat=0.150   & kofat=30.               ;Ca ATP rate constants
kofatMg=0.195 & konatMg=0.00195         ;Mg ATP
kdt=2.          &   kont=0.0057         ;dissoc. const. and kon troponin
fkof=fkon*fkd                           ;off rate const fluo
kofe=kone*kde                           ;off rate const egta
koft=kont*kdt                           ;off rate const troponin
kdpa=kofpa/konpa                        ;dissoc constant ca parv
kdmg=kofmg/konmg                        ;dissoc constant mg parv
kdat=kofat/konat                ;dissoc constant ca parv
kdatmg=kofatmg/konatmg                  ;dissoc constant mg parv
```

```
;***miscellaneous***

dff=[.03,0.0,-.05,-.01,.1,.03,-.24,-.31,0.0,.31,.24,-.03,-.1,.01,.05,0.0,-.03]          ;differentiation kernel
;dff=[0,0,0,0,0,0,0,0,-.5,0,.5,0,0,0,0,0,0,0,0]     ;simple differentiation kernel
factor=0.70                                        ;only 70% of the fiber volume are accessible for the dye
dt=2.0                                             ;time resolution of images
dx= 0.500/zoom                          ;x resolution of images
euler=100                                          ;number of euler steps
r = 100.0                                          ;Fmax/Fmin value (100 for lower estimate of Ca)
bg=0.0                                             ;bg
rm=r-1.

rin=float(nwi)/float(nwm)               ;below calc. for x and t increment
dx=dx*rin
x=findgen(nwp)
x=interpolate(x,rin*findgen(nwi))
x=x-nwi/2
x=rebin(x,nwi,nwp)*dx
xd=dx*xd                                           ;makes the x coordinate
td=dt*xd/dx                                        ;makes the t coordinate
                                                   ;td is interval number in euler procedure
c=1+(r*ca0/fkd)                                    ;constant to calculate Ca:Dye
jump7:
fnama=''                                ;initialization
flav=0
dyav=0

read, fnama, prompt='Enter average file,( no ext., default .avg): '
fname=fnama+'.avg'
fnama=STRMID(fnama,2,3)                                 ;shorter fnama

jump12:
counti=1
openu,u,fname,/get_lun & zu=assoc(u,fltarr(nwp,nwp+1))
avgarr=zu(counti-1)
free_lun,u
z=avgarr(*,1:nwp)                       ;contains average absolute fluorescence (is only for nice display yet)
effgain=exp((gain-1000.)*0.011)                    ;ratio of actual gain and reference gain (from calibrations)
tvlct,re,g,bl,/get                      ;below only display parameters
re(0)=255&g(0)=255&bl(0)=255
tvlct,re,g,bl
ah=-0.75
bh=0.25
ch=1.0
back=255
loadct, 0                       ;bw color table
anglex=45
anglez=45

jump07:
window, 0
shade_surf,z(*,0:42),ax=anglex,az=anglez,charsize=2,xstyle=4,ystyle =4,$       ;angleview plot
background = 255, color =2

loadct, 4                                          ;bgry color table
window, 1
shade_surf,z(*,0:42),ax=90,az=0,charsize=2,xstyle=4,ystyle =4,$                                 ;topview plot
background = 0, color =1 ,zrange=[0,200],zstyle=1, shade=bytscl(z(*,0:42))
read,dummy,prompt='any key, b to change background, angles:'
if dummy ne 'b' then goto,jump08
read,back,anglez,anglex,prompt='enter background level, anglez, anglex:'
goto,jump07
```

```
jump08:                          ;smoothing routine
if sm gt 0 then z=smooth(z,3)
for i=0,2 do z(i,*)=z(3,*)       ;flatten the edges of the array
for i=0,2 do z(nwi-i,*)=z(nwi-3,*)
for j=0,1 do z(*,j)=z(*,2)
for j=43,44 do z(*,j)=z(*,42)

jump01:
print,'maximum fluoresc. = ',max(z)
flav=avgarr(*,1:nwp)                    ;contains absolute fluorescence
avgarr(*,0)=avgarr(*,0)*0.1/ca0         ;scaling of baseline and dye to ca
dyav=avgarr(*,0)                 ;contains dye(x) from
fluo=total(avgarr(*,0))/n_elements(avgarr(*,0))    ;average total dye concentration
print,'avg. dye =',fluo,' central =',total(avgarr(nwih-2:nwih+2))/5
bb =laser*dyav*kmax*exp((gain-1000.)*0.011)*ca0/fkd    ;the baseline fluorescence will be recreated
bbl=rebin(flav(0:nwi,0:9),nwp,1)    ;local baseline recreated

;***DEBLURRING***
;***calculation of gaussian functions***

xk=(0.01+findgen(nwp)-floor(nwp/2))    ;x for kernel (almost integer centered at almost zero)
fwhm=0.4
fwh=0.4
jump25:
if fwhm eq 0 then fwhm=0.4
sigma=fwhm/2.3548                ;use for gaussian
y=xk*dx/sigma                    ;standard argument for gaussian
kernely=exp(-y^2/2)              ;kernely is now gaussian function for PSF in x and y
direction
kernely=kernely/total(kernely)   ;normalization to 1
uz=3                             ;ratio of sigmaz/sigmax
w=y/uz
kernelz=exp(-w^2/2)
kernelz=kernelz/total(kernelz)   ;kernelz is now gaussian function for PSF in z direction
read,fwhm,prompt='FWHM in x: (0 for OK, -1 for no deblur) '
if fwhm lt 0 then begin
 fwh=0
 goto, jump28
endif
if fwhm ne 0 then begin
 fwh=fwhm
 goto,jump25
endif

;***fourier transformations for deblurring****

ft=fft(kernely,/double)          ;fourier transform (corresponds to G~ )
flavs=flav-rebin(bbl,45,45)      ;subtracting baseline
for i=3,nwm-2 do begin
flavi=flavs(*,i)
sflavi=smooth(flavi,3)           ;smoothing
maxf=max(sflavi(19:25))>0        ;corresponds to F(0)
fflav=fft(flavi,/double)         ;corresponds to F~
temp=fflav/ft/Nwp                ;division by G~ fdflav=temp
flavi=shift(fft(fdflav,1,/double),floor(Nwp/2))    ;back transformation, unscaled g1
flavi(0:3)=flavs(0:3,i) & flavi(nwi-3:nwi)=flavs(nwi-3:nwi,i) ;no fourier for edges
flavi=float(flavi)
if sm ge 3 then sflavi=smooth(flavi,sm) else sflavi=flavi
maxfl=(max(sflavi(19:25)))>1     ;maximum of the deconvolved function
gflavi=flavi/maxfl               ;this is g(x) the deconvolved with max=1
```

```
corrz=(total(kernelz*gflavi)<1)>0.3                    ;this is integral L
corry=(total(kernely*gflavi)<1)>0.7                    ;this is integral J
cor=1./corry^2/corrz <3
flavi=gflavi*maxf*cor                                  ;this is f(x,0,0), the deblurred spark at time t_j
print,'i=',i,' L =',corrz,'  J = ',corry, '  correction = ',cor, ' max corr.f= ',cor*maxf
flav(*,i)=flavi+bbl
endfor
jump27:
jump28:                                                ;when no correction

print,'max deblurred fluoresc. = ',max(flav)

loadct,0                                               ;bw-color table
jump05:
set_shading,light=[ah,bh,ch]                           ;display routine for deblurred fluorescence
shade_surf,flav,ax=45,az=45,charsize=2,color=1, xstyle=4,ystyle =4, background = 255
jump06:
read,dummy,prompt='a , b, or c, any other to exit:'
if dummy eq 'a' then begin
read, ah, prompt= ' x vector, (-1 to 1):'
if ah lt -1 or ah gt 1 then goto,jump06
goto,jump05
endif
if dummy eq 'b' then begin
read, bh, prompt= ' y vector, (-1 to 1):'
if bh lt -1 or bh gt 1 then goto,jump06
goto,jump05
endif
if dummy eq 'c' then begin
read, ch, prompt= ' z vector, (-1 to 1):'
if ch lt -1 or ch gt 1 then goto,jump06
goto,jump05
endif
loadct,13
tvlct,re,g,bl,/get
re(0)=255&g(0)=255&bl(0)=255
tvlct,re,g,bl
;stop
jump8:
                                                       ;symmetrizing the spark
for i=0,nwi do flav(i,*)=(flav(i,*)+flav(nwi-i,*))/2
conrta='y'
anglez=40
conrot='y'

relx(*)=0                                              ;this part is to make a x-cut through the maximum
maxflu=max(rebin(flav(20:24,10:30),1,21))
whemax=where(rebin(flav(20:24,10:30),1,21) eq maxflu)+10
whe=whemax(0)
if isim eq 's' then relx=flav(0:nwm,whe) else relx=rebin(flav(0:nwm,whe-1:whe+1),nwi,1)
plot, relx                                                 ;plot the x-cut
dummy=''
read,dummy,prompt='fluoresc vs. x, any key to cont., b to go back, o to output: '
if dummy eq 'b' then goto,jump12
if dummy eq 'o' then begin
dummy=''
arrayx(0,*)=findgen(nwi)*dx
arrayx(1,*)=relx
outnamo=string(format='((A),(i2),"vsx.asc")',fnama,fix(100*fwh))  ;output x-cut in file
outnamo=strcompress(outnamo,/remove_all)
openw,un,outnamo,/get_lun
printf,un,format='(2f9.4)',arrayx                      ;output x-cut on screen
```

```
close,un
endif
relx=rebin(flav(20:23,1:nwi),1,nwi)                    ;makes t-cut through maximum
plot, relx
dummy=''
read,dummy,prompt='fluoresc vs. t, any key to cont., b to go back, o to output: '
if dummy eq 'b' then goto,jump12
if dummy eq 'o' then begin
dummy=''
arrayx(0,*)=findgen(nwi)*2.
arrayx(1,*)=relx
outnamo=string(format='((A),(i2),''vst.asc'')',fnama,fix(100*fwh))     ;output x-cut on file
outnamo=strcompress(outnamo,/remove_all)
openw,un,outnamo,/get_lun
printf,un,format='(f7.1, f9.4)',arrayx                                  ;output t-cut on screen
close,un
endif
dflav=flav
dum=''
read,dum,prompt='smooth? (y=yes; m= median):'  ;smoothing or median filter
if dum eq 'y' or dum eq 'm' then begin
dflave(0,2:nwp+1)=flav(0,*)                                 ;expand array before smoothing
dflave(1,2:nwp+1)=flav(0,*)
dflave(nwp+2,2:nwp+1)=flav(nwi,*)
dflave(nwp+3,2:nwp+1)=flav(nwi,*)
dflave(2:nwp+1,2:nwp+1)=flav
dflave(*,0)=dflave(*,2)
dflave(*,1)=dflave(*,2)
dflave(*,nwp+2)=dflave(*,nwp+1)
dflave(*,nwp+3)=dflave(*,nwp+1)
if sm gt 0 and dum eq 'y' then dflave=smooth(dflave,sm)        ;normal smoothing
if dum eq 'm' then dflave=median(dflave,3)                          ;median filter
dflav=dflave(2:nwp+1,2:nwp+1)    ;contract array after smoothing
dflav(*,0)=dflav(*,1)
loadct,0
set_shading,light=[ah,bh,ch]          ;display smoothed fluorescence
shade_surf,dflav(*,0:42),ax=45,az=45,color=1, xstyle=4,ystyle=4,charsize=2,background = 255
read,dummy,prompt='fluorescence, smoothed, b to go back to line plots: '
if dummy eq 'b' then begin
flav=dflav
goto,jump28
endif
endif

;***calculation of Ca bound to dye***

loadct,0
for j=0,nwi do dyav(j)=(dyav(j)+dyav(nwi-j))/2 ;symmetrize dyetotal(x), too
for j=0,nwi do dyarr(j,*)=dyav(j)   ;dyarr is an array of [dye total](x) which is constant in time
                                    ;first will regenerate the baseline fluorescence (F0)after eqn. 4.29
bb =laser*  dyav*kmax*exp((gain-1000.)*0.011)*ca0/fkd      ;baseline fluorescence
bbo=total(bb)/n_elements(bb)                                                ;average F0
fluo=total(dyav)/n_elements(dyav)                  ;average total dye concentration
dcd_x=dcd*total(bbl)/bbl/n_elements(bbl)           ;the local dye binding factor
                                                   ;that explains unequal dye distribution
dcd_x=rebin(dcd_x,45,45)
jump11:for i=0,nwi do begin          ;i is boxcar time
  for j=0,nwi do begin               ;j is x coordinate
     z(j,i)=dflav(j,i)-bg  ; z is fluorescence in boxcar
     z(j,i)=fluo*(c*z(j,i)-bb(j))/rm/bbo                ;z is Ca-bound dye (dye (cF-Fo)/((R-1)Foavg))
  endfor
```

```
endfor
;**********************
print, "max Ca:dye concentration ",max(z)
shade_surf,z,ax=45,az=45,color=1, xstyle=4,ystyle=4,charsize=2,background = 255
read,dummy,prompt='dye:Ca concentration, any key: '
for i=0,nwi do begin
ri(*,i)=interpolate(z(*,i),rin*findgen(nwi))
dyrr(*,i)=interpolate(dyarr(*,i),rin*findgen(nwi))
dccd(*,i)=interpolate(dcd_x(*,i),rin*findgen(nwi))
endfor
z=ri
dyarr=dyrr
dertb,z,dzdt,dt                 ;derivative in time of Cadye is dzdt
dzdt(*,[0,1,nmm,nwm])=0.0
dzdt([0,1,nmm,nwm],*)=0.0
if sm gt 0 then dzdt=smooth(dzdt,sm)

loadct,0
set_shading,light=[ah,bh,ch]    ;display time derivative
shade_surf,dzdt,ax=45,az=anglez,charsize=2,color=1, xstyle=4,ystyle =4, background = 255
read,dummy,prompt='any key:'

jump013:
maxrel=max(dzdt)
print,maxrel
whemax=min(where(dzdt eq maxrel))
ymax=floor(whemax/nwi);x coordinate of maximum
relx=dzdt(*,ymax)
plot,relx                       ;plot x-cut through maximum time derivative
dum=''
read,dum,prompt='max derivative, any key'

jump017:
derxb,z,dzdx,dx ;dzdt and dzdx now contain first time and space derivatives
dzdx(*,[0,1,nmm,nwm])=0.0
dzdx([0,1,nmm,nwm],*)=0.0
loadct,0
set_shading,light=[ah,bh,ch]    ;display space derivative
shade_surf,dzdx,ax=45,az=anglez,charsize=2,color=1, xstyle=4,ystyle =4, background = 255
read,sm,prompt='space derivative of dye:Ca, type 3 for smoothing:'
if sm gt 0 then dzdx=smooth(dzdx,sm)    ;DANGEROUS TO ELIMINATE THIS STEP

derxb,dzdx,d2z,dx               ;calculate second derivative with space
d2z(*,[0,1,nmm,nwm])=0.0
d2z([0,1,nmm,nwm],*)=0.0
shade_surf,d2z,ax=45,az=anglez,charsize=2,color=1, xstyle=4,ystyle =4, background = 255
read,sm,prompt='second derivative, type 3 for smoothing:'
if sm gt 0 then d2z=smooth(d2z,sm)

diff_term=-dccd*(d2z+2*dzdx/x)  ;only diffusional term
dye_term=diff_term+dzdt                 ;complete dye removal
loadct,0
set_shading,light=[ah,bh,ch]    ;display of dye removal
shade_surf,dye_term,ax=45,az=anglez,charsize=2,color=1, xstyle=4,ystyle =4, background = 255
read,dummy,prompt='total dye removal, any key:'
shade_surf,diff_term,ax=45,az=anglez,charsize=2,color=1, xstyle=4,ystyle =4, background = 255
read,dummy,prompt='diffusional dye term, any key:'



;***calculation of Ca(x,t)***
```

```
caimg=((dye_term+fkof*z)/fkon/(dyarr-z))>ca0        ;after eqn. 4.50
for i=0,nwm do begin
for j=0,nwi do begin
caimg(i,j)=(caimg(i,j)+caimg(nwm-i,j))/2    ;symmetrizing
endfor
endfor
caini(*)=0.0        ;initial Ca for spark
for i=0,nwm do begin
for j=0,9 do caini(i)=caini(i)+caimg(i,j)
caini(i)=caini(i)/10
endfor
cavini=total(caini)/nwi
                                              ;display Ca(x,t)
shade_surf,caimg,ax=45,az=45,color=1, xstyle=4,ystyle=4,charsize=2,background = 255, zrange=[0,10]
read,dummy,prompt='output Ca (x,t) ascii? y=yes: '
wait,2 & dummy = 'n'

if dummy eq 'y' then begin ;output Ca(x,t)
outnamo=fnama +'ca.asc'
openw,un,outnamo,/get_lun
printf,un,format='(44f8.2)',caimg
close,un
endif

dertb,caimg,dcat,dt          ;time derivative of Ca in dcat
dcat(*,[0,1,nmm,nwm])=0.0
dcat([0,1,nmm,nwm],*)=0.0
if sm gt 0 then dcat=smooth(dcat,sm)

derxb,caimg,dcax,dx                ;dcax is first space derivative
dcax(*,[0,1,nmm,nwm])=0.0
dcax([0,1,nmm,nwm],*)=0.0

derxb,dcax,d2c,dx                  ;d2c is second space derivative
d2c(*,[0,1,nmm,nwm])=0.0
d2c([0,1,nmm,nwm],*)=0.0
if sm gt 0 then d2c=smooth(d2c,sm)

;***Ca Removal calculations***

CaE(*,*)=egta*cavini/(cavini+kde)                          ;egta:ca set to initial value
CaPa(*,*)=parv*cavini/(cavini+kdpa+Mg*kdpa/kdmg)           ;Ca parvalbumin
MgPa(*,*)=parv*mg/(mg+kdmg+cavini*kdMg/kdpa)               ;Mg Parvalbumin
CaAt(*,*)=atp*cavini/(cavini+kdat+Mg*kdat/kdatmg)          ;Ca ATP
MgAt(*,*)=atp*mg/(mg+kdatmg+cavini*kdatMg/kdat)            ;Mg ATP
Cat(*,*)=trop*cavini/(cavini+kdt)                          ;trop:ca set to initial value
CaP(*,*)=pump*cavini/(cavini+kdp)                          ;pump:ca set to initial value

teuler=dt/euler

for i=1,nmm do begin                                       ;loop over time (i is time)
dca=(caimg(*,i+1)-caimg(*,i))/euler
for it=1,euler+1 do begin

;calculate  derv with space.  First extend buffer for convolution with Kaiser kernel

dbuf(8:np8)=cae(*,i-1)
dbufpa(8:np8)=capa(*,i-1)
dbufmg(8:np8)=mgpa(8,i-1)
dbufat(8:np8)=caat(*,i-1)
dbufatmg(8:np8)=mgat(8,i-1)
for j=0,7 do begin
```

```
        dbuf(j)=cae(0,i-1)
        dbufpa(j)  =capa(0,i-1)
        dbufatmg(j)=Mgat(0,i-1)
        dbufat(j)  =caat(0,i-1)
        dbufmg(j)  =Mgpa(0,i-1)
endfor
for j=nwi+8,nwi+15 do begin
        dbuf(j)  =cae(nwm,i-1)
        dbufpa(j)  =capa(nwm,i-1)
        dbufmg(j)=Mgpa(nwm,i-1)
        dbufat(j)  =caat(nwm,i-1)
        dbufatmg(j)  =Mgat(nwm,i-1)
endfor

if smm gt 0 then begin
dbuf=smooth(dbuf,smm)           ;& dbuf=smooth(dbuf,sm)
dbufpa=smooth(dbufpa,smm)       ;& dbufpa=smooth(dbufpa,sm)
dbufmg=smooth(dbufmg,smm)       ;& dbufmg=smooth(dbufmg,sm)
dbufat=smooth(dbufat,smm)       ;& dbufpa=smooth(dbufpa,sm)
bufatmg=smooth(dbufatmg,smm) ;& dbufmg=smooth(dbufmg,sm)
endif

for j=0,nwm do dcae(j)=total(dff*dbuf(j:j+16))/dx    ;actual differentiation!
for j=0,nwm do dcapa(j)=total(dff*dbufpa(j:j+16))/dx
for j=0,nwm do dmgpa(j)=total(dff*dbufmg(j:j+16))/dx
for j=0,nwm do dcaat(j)=total(dff*dbufat(j:j+16))/dx
for j=0,nwm do dmgat(j)=total(dff*dbufatmg(j:j+16))/dx

;***calculate 2nd. derv with space.  First extend buffer***

dbuf(8:np8)=dcae(*)
dbufpa(8:np8)=dcapa(*)
dbufmg(8:np8)=dmgpa(*)
dbufat(8:np8)=dcaat(*)
dbufatmg(8:np8)=dmgat(*)
for j=0,7 do   dbuf(j)  =dcae(0)
for j=0,7 do dbufpa(j)  =dcapa(0)
for j=0,7 do dbufmg(j)  =dmgpa(0)
for j=0,7 do dbufat(j)  =dcaat(0)
for j=0,7 do dbufatmg(j)  =dmgat(0)
for j=nwi+8,nwi+15 do dbuf(j)  =dcae(nwm)
for j=nwi+8,nwi+15 do dbufpa(j)  =dcapa(nwm)
for j=nwi+8,nwi+15 do dbufmg(j)  =dmgpa(nwm)
for j=nwi+8,nwi+15 do dbufat(j)  =dcaat(nwm)
for j=nwi+8,nwi+15 do dbufatmg(j)  =dmgat(nwm)
for j=0,nwm do d2cae(j)=total(dff*dbuf(j:j+16))/dx
for j=0,nwm do d2capa(j)=total(dff*dbufpa(j:j+16))/dx
for j=0,nwm do d2mgpa(j)=total(dff*dbufmg(j:j+16))/dx
for j=0,nwm do d2caat(j)=total(dff*dbufat(j:j+16))/dx
for j=0,nwm do d2mgat(j)=total(dff*dbufatmg(j:j+16))/dx
for j=1,nmm do begin     ;loop over space
                ;uses previous values
                ;dca=(caimg(j,i+1)-caimg(j,i))/euler          ;Ca increment in Euler time
ca=caimg(j,i) + (it-1.)*dca(j)          ;local [Ca] in prior time
caegta=CaE(j,i)
catrop=Cat(j,i) ;CaEGTA, will be updated
capump=cap(j,i) ;Capump
caparv=Capa(j,i);Ca:parvalbumin
mgparv=Mgpa(j,i)          ;mg:parvalbumin
caatp=Caat(j,i)    ;Ca:atp
mgatp=Mgat(j,i)  ;mg:atp
remegta=(Ca*(egta-caegta)*kone-caegta*kofe)*teuler          ;removal by EGTA
```

```
rempump=(Ca*(pump-capump)*kpon-capump*kpof)*teuler  ;remov by pump
remparv=(Ca*(parv-caparv-mgparv)*konpa-caparv*kofpa)*teuler ;removal by Parv
rmgparv=(Mg*(parv-caparv-mgparv)*konmg-mgparv*kofmg)*teuler ;removal of Mg by Parv
rematp=(Ca*(atp-caatp-mgatp)*konat-caatp*kofat)*teuler ;removal by Parv
rmgatp=(Mg*(atp-caatp-mgatp)*konatmg-mgatp*kofatmg)*teuler ;removal of Mg by Parv
remtrop=(Ca*(trop-catrop)*kont-catrop*koft)*teuler ;remov by troponin
dcaegta=remegta +dce*(d2cae(j)+2*dcae(j)/x(j,0))*teuler      ;change in caegta is removal +diffusion
dcaparv=remparv +dcpa*(d2capa(j)+2*dcapa(j)/x(j,0))*teuler;change in caparv is removal +diffusion
dMgparv=rmgparv +dcpa*(d2mgpa(j)+2*dmgpa(j)/x(j,0))*teuler       ;change in Mgparv is removal +diffusion
dMgatp=rmgatp +dcatp*(d2mgat(j)+2*dmgat(j)/x(j,0))*teuler        ;change in Mgatp is removal +diffusion
dcaatp=rematp +dcatp*(d2caat(j)+2*dcaat(j)/x(j,0))*teuler    ;change in caatp is removal +diffusion
dcatrop=remtrop ;change in catrop is just removal
dcapump=rempump
;update for next iteration
CaE(j,i)=0.5*(CaE(j-1,i)+CaE(j+1,i))+dcaegta         ;the LAX method!!
Capa(j,i)=0.5*(Capa(j-1,i)+Capa(j+1,i))+dcaparv
Mgpa(j,i)=0.5*(Mgpa(j-1,i)+Mgpa(j+1,i))+dmgparv
Caat(j,i)=0.5*(Caat(j-1,i)+Caat(j+1,i))+dcaatp
Mgat(j,i)=0.5*(Mgat(j-1,i)+Mgat(j+1,i))+dmgatp
Cat(j,i)=0.5*(cat(j-1,i)+Cat(J+1,i))+dcatrop
CaP(j,i)=0.5*(caP(j-1,i)+CaP(J+1,i))+dcapump
rem(j,i)=rem(j,i)+remegta+remtrop+remparv+rematp+rempump
                                    ;(removal into EGTA, ATP, parv, pump and troponin)

endfor      ;loop (j) over space ends
endfor                                          ;loop (it) over euler increments ends

cae(0,i)=cae(1,i)                               ;this is a reflective boundary
cae(nwm,i)=cae(nmm,i)
cae(*,i+1)=cae(*,i)                              ;updates cae for next iteration
capa(0,i)=capa(1,i)                             ;this is a reflective boundary
capa(nwm,i)=capa(nmm,i)
capa(*,i+1)=capa(*,i)                           ;updates capa for next iteration
Mgpa(0,i)=Mgpa(1,i)                             ;this is a reflective boundary
Mgpa(nwm,i)=Mgpa(nmm,i)
Mgpa(*,i+1)=Mgpa(*,i)                           ;updates Mgpa for next iteration
caat(0,i)=caat(1,i) & caat(nwm,i)=caat(nmm,i)   ;this is a reflective boundary
caat(*,i+1)=caat(*,i)                                   ;updates capa for next iteration
Mgat(0,i)=Mgat(1,i)       & Mgat(nwm,i)=Mgat(nmm,i)     ;this is a reflective boundary
Mgat(*,i+1)=Mgat(*,i)                           ;updates Mgat for next iteration
cat(*,i+1)=cat(*,i)                                     ;updates cat
cap(*,i+1)=cap(*,i)                                     ;updates cap
rem(1:nmm,i)=rem(1:nmm,i)/dt ;this converts to per millisecond
rem(1,i)=rem(2,i)
rem(0,i)=rem(1,i)
rem(nmm,i)=rem(nmmm,i)
rem(nwm,i)=rem(nmm,i)
endfor                      ;loop (i) over time ends
cae(*,nwi)=cae(*,nwm)
capa(*,nwi)=capa(*,nwm)
Mgpa(*,nwi)=mgpa(*,nwm)
caat(*,nwi)=caat(*,nwm)
Mgat(*,nwi)=mgat(*,nwm)

rem(*,1)=rem(*,2)
rem(*,0)=rem(*,1)
rem(*,nmm)=rem(*,nmmm)
rem(*,nwm)=rem(*,nmm)

                                    ;display results of release calculation
shade_surf,cat,ax=45,az=60,color=1, zcharsize=2,background = 255
read,dummy,prompt='[Ca:fast nondiffusible buffer], enter any key: '
```

```
shade_surf,capa,ax=45,az=80,zcharsize=2.0,background = 255
read,dummy,prompt='[Ca:Parvalbumin], enter any key: '
shade_surf,Mgpa,ax=45,az=80,zcharsize=2.0,background = 255
read,dummy,prompt='[Mg:Parvalbumin], enter any key: '
shade_surf,caat,ax=45,az=60,zcharsize=2.0,background = 255
read,dummy,prompt='[Ca:ATP], enter any key: '
shade_surf,Mgat,ax=45,az=60,zcharsize=2.0,background = 255
read,dummy,prompt='[Mg:ATP], enter any key: '
;*****************************
jump41:
casat=caimg/(caimg+kdp);calculate pump term
casat=mp*(casat^2)          ;pump term finished
rem=rem+casat               ;note all removal terms added
rems=rem(*,0:44)
shade_surf,rems,ax=45,az=60,color=1, xstyle=4,ystyle=4,zcharsize=2.0, background=255
read,dummy,prompt='removal by EGTA, Trop, Parv, Pump, ATP: '
;print,'release in mM*micron^3/s=',inte,' in pA=',inte*0.2;


d2c=-dcc*(d2c+2*dcax/x)
d2c=d2c+dcat     ;note all Ca terms added
shade_surf,d2c,ax=45,az=45,color=1, zcharsize=2,background = 255
read,dummy,prompt='Ca diffusion term,: '

rel=(d2c + dzdt +diff_term +rem)*factor     ;calculation of release(x,t)
relt=rebin(rel,1,45)                                    ;get x-cut of release
whemax=where(relt eq max(relt))
relx=rel(*,whemax)
plot, relx
dummy=''
read,dummy,prompt='release vs. x, any key to cont.: '
ta=findgen(44)                                  ;determin FWHM of release(x,t)
tx=findgen(881)/20.
atint=spline(ta,relx,tx)
maxat=max(atint)
halfw=n_elements(where(atint ge maxat/2))
print,'half width =',halfw*dx/20
;**********************
relx=(rel(21,*)+rel(22,*)+rel(20,*)+rel(23,*))/4        ;get t-cut of release
plot,relx
read,dummy,prompt='release vs. t, any key: '
atint=spline(ta,relx,tx)                ;determin FDHM of release(x,t)
maxat=max(atint)
tm=where(atint eq maxat) &tm=tm(0)
halfw=n_elements(where(atint(tm-70:tm+70) ge maxat/2))
print,'half dur =',halfw*dt/20.

jump011:anglez=45                       ;rotations here
loadct,0
set_shading,light=[ah,bh,ch]            ;display release(x,t)
shade_surf,rel(*,0:42),ax=45,az=anglez,charsize=2,color=1, xstyle=4,ystyle =4, background = 255,
zrange=[0,300]
read,dummy,prompt='output ascii? y=yes: ' ;output release(x,t)
if dummy eq 'y' then begin
        outnamo=fnama +'r.asc'
        openw,un,outnamo,/get_lun
        printf,un,format='(44f8.2)',rel
        close,un
endif
end     ;end of program
```

7.2 The preamplifier with voltage-clamp circuit

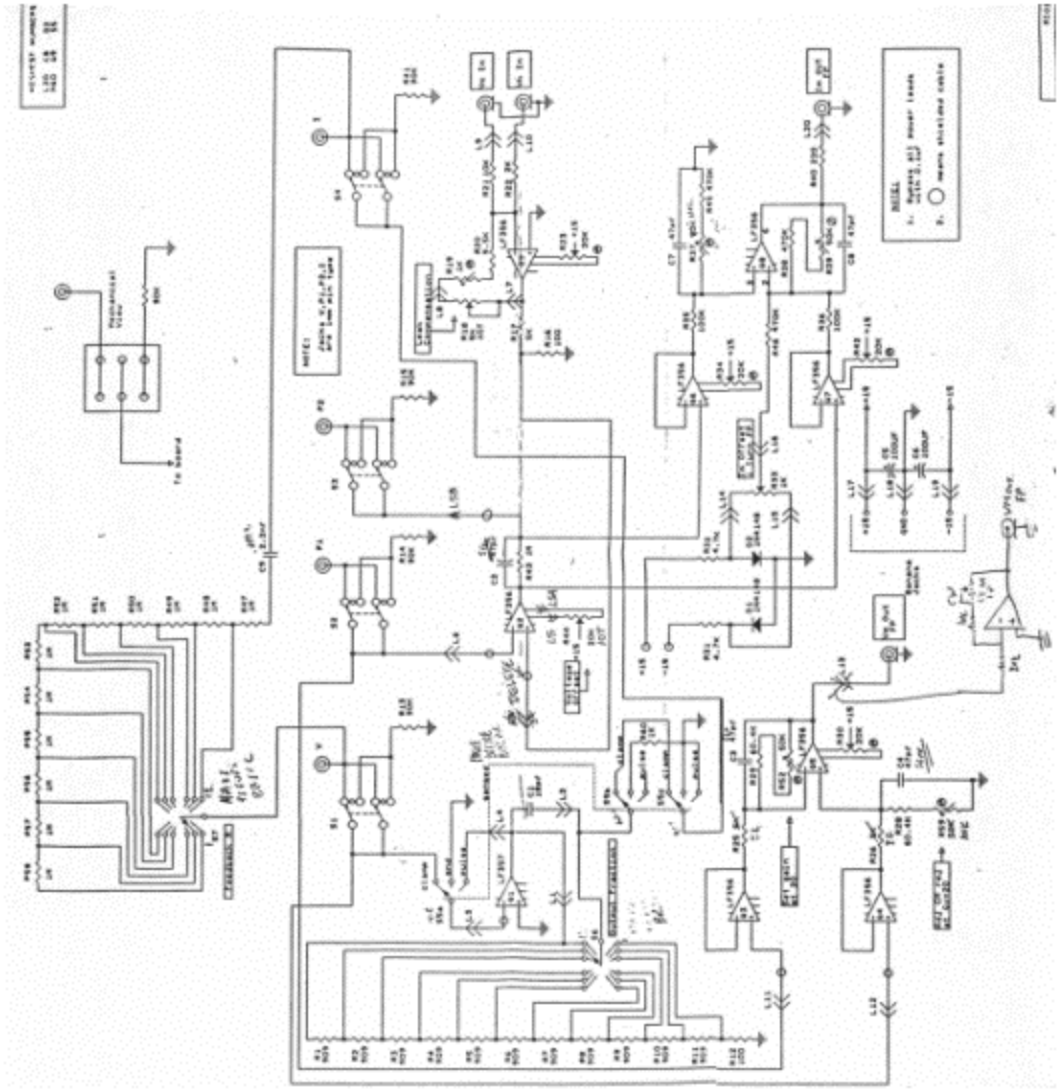

Publications

González A., Kirsch W.G., Shirokova N., Pizarro G., Brum G., Pessah I.N., Stern M.D., Cheng H., Ríos E. (2000a). Involvement of multiple intracellular release channels in calcium sparks of skeletal muscle. *Proc. Natl. Acad. Sc. (USA)*. 97(8), 4380-5

González A., Kirsch W.G., Shirokova N., Pizarro G., Stern M.D., Ríos E. (2000b). The Spark and Its Ember. Separately gated local components of Ca^{2+} release in skeletal muscle. *J Gen Physiol.* 115(2), 139-158.

Kirsch W.G., Uttenweiler D., Fink R.H.A. (2000a) Ca^{2+} sparks in saponin skinned amphibian skeletal muscle fibres. *Plügers Archiv.* 439(6), R410

Kirsch W.G., González A., Shirokova N., Pizarro G., Stern M.D., Ríos E. (2000b). The spark and the ember. Insights from interventions that interfere with CICR in skeletal muscle. *Biophys. J.* 78, A276

Shirokova N., Shirokov R., Rossi D., Gonzalez A., Kirsch W.G., Garcia J., Sorrentino V., Rios E. (1999a). Spatially segregated control of Ca^{2+} release in developing skeletal muscle of mice. *J. Physiol.* 521, 483-95

Shirokova N., González A., Kirsch W.G., Ríos E., Pizarro G., Stern M.D., Cheng H. (1999b). Calcium sparks: release packets of uncertain origin and fundamental role. *J Gen Physiol.* 113(3), 377-84. Review.

Kirsch W.G., González A., Pizarro G., Shirokova N., Ríos E. (1999). Rattifying the Frog: Effects of High Intracellular [Mg^{2+}] on Global Ca Release in Skeletal Muscle. *Biophys. J.* 76, A385

Kirsch W.G. (1997). Aufbau und Testen einer verbesserten ´Vaseline gap´-Apparatur für Voltage-Clamp-Messungen mit simultaner Fluoreszenzspektroskopie. *Diplomarbeit, Universität Heidelberg*

References

Agard D.A. (1984). Optical sectioning microscopy: cellular architecture in three dimensions. *Ann. Rev. Biophys. Bioeng*. 13, 191-219

Agard D.A., Hiraoka Y., Shaw P., Sedat J.W. (1989). Fluorescence microscopy in three dimensions. *Methods Cell Biol*. 30, 353-377

Almers W., Fink R., Palade P. T., (1980). Calcium Depletion in Frog Muscle Tubules: The Decline of Calcium Current under Maintained Depolarization. *J. Physiol.* 312,177-207

Almers W., McCleskey E. W., Palade P. T., (1984). A Non-Selective Cation Conductance In Frog Muscle Membrane Blocked by Micromolar External Calcium Ions. *J. Physiol*. 353, 565-583

Baylor S. M., Chandler W. K., Marshall M. W. (1983). Sarcoplasmic reticulum calcium release in frog skeletal muscle fibres estimated from Arsenazo III calcium transients. *J. Physiol*. 344, 625-666

Baylor S.M., Hollingworth S. (1998). The transient binding of calcium to ATP and diffusion of Ca-ATP help shape the amplitude and time course of the myoplasmic free Ca transient. *Biophys. J*. 74, A235

Birge R.R. (1979). A theoretical analysis of the two-photon properties of linear polyenes and the visual chromophores. *J.Chem. Phys*. 70, 165

Block B.A., Imagawa T., Campbell K.P., Franzini-Armstrong C. (1988). Structural evidence for direct interaction between the molecular components of the transverse tubule/sarcoplasmic reticulum junction in skeletal muscle. *J. Cell. Biol.* 107, 2587-600

Brum G., Ríos E. (1987). Intramembrane charge movement in frog skeletal muscle fibers. Properties of charge 2. J. Physiol. 387, 489-517

Brum G., Fitts R., Pizarro G., Ríos E. (1988a). Voltage Sensors of the Frog Skeletal Muscle Membrane Require Calcium to Function in Excitation-Contraction Coupling. *J. Physiol.* 398, 475-505

Brum G., Ríos E., Stéfani E. (1988b). Effects of extracellular calcium on calcium movements of excitation-contraction coupling in frog skeletal muscle fibers. *J. Physiol*. 398, 441-473

Cheng H., Lederer W.J., Cannell M.B. (1993). Calcium sparks: elementary events underlying excitation-contraction coupling in heart muscle. *Science* 262, 740-744

Cheng H., Song L.S., Shirokova N., González A., Lakatta E.G., Ríos E., Stern M.D. (1999). Amplitude distribution of calcium sparks in confocal images. Theory and studies with an automatic detection method. *Biophys. J*. 76, 606-617

Conklin M.W., Barone V., Sorrentino V., Coronado R. (1999). Contribution of ryanodine receptor type 3 to Ca($^{2+}$) sparks in embryonic mouse skeletal muscle. *Biophys. J.* 77(3), 1394-403

Coronado, R., J. Morrissette, M. Sukhareva, and D. M. Vaughan (1994). Structure and function of ryanodine receptors. *Am. J. Physiol.* 266, C1485-C1504

Curley P.F., Ferguson A.I., White J.G., Amos W.B. (1992). Application of a femtosecond self-sustaining mode-locked Ti:sapphire laser to the field of laser scanning confocal microscopy. *Opt. Quant. Electr*. 24, 851

Denk W., Strickler J.H., Webb W.W. (1990). Two-photon laser scanning microscopy. *Science* 248, 73

Denk W., Piston D.W., Webb W.W. (1995). Two-photon molecular excitation in laser-scanning microscopy. *In Pawley J.B.: Handbook of biological confocal microscopy. Plenum Press*

Deetjen P., Speckmann E. (1994). Physiologie, *Urban & Schwarzenberger.*

Deutsch N., Matsuoka S., Weiss J.N. (1994). Surface charge and properties of cardiac ATP-sensitive K+ channels. *J. Gen. Physiol.* 104, 773-800

El-Hayek R., Antoniu B., Wang J., Hamilton S.L., Ikemoto N. (1995). Identification of calcium release-triggering and blocking regions of the II-III loop of the skeletal muscle dihydropyridine receptor. *J. Biol. Chem*. 270, 22116-22118

Endo M. (1977). Calcium release from the sarcoplasmic reticulum. *Physiological reviews*. 57, 71-108

Escobar A.L., Monck J.R., Fernandez J.M., Vergara J.L. (1994). Localization of the site of Ca^{2+} release at the level of a single sarcomere in skeletal muscle fibres. *Nature* 367, 739-41

Fabiato A., Fabiato F., (1979). Calculator Programs for Computing the Composition of the Solutions Containing Multiple Metals and Ligands Used for Experiments in Skinned Muscle Cells. *J. Physiol. (Paris)* 75, 463-505

Feierabend M. (1999). Aufbau und Kalibrierung eines konfokalen Meßsystems mit UV-Laser-Einkopplung zur Herstellung von Myofibrillenpräparaten mittels Mikrogewebeablation. *Diplomarbeit, Universität Heidelberg*

Fink R. H. A., Stephenson D. G., (1984). Blocking of K+ Channels in SR-Membranes can increase net Ca^{2+}-Loading. *Biophys. J.* 45, 318a

Franzini-Armstrong C., Protasi F., Ramesh V. (1998). Comparative ultrastructure of Ca^{2+} release units in skeletal and cardiac muscle. *Ann. N Y Acad. Sci.* 853, 20-30

García J., Schneider M.F. (1993). Calcium transients and calcium release in rat fast-twitch skeletal muscle fibres. *J. Physiol*. 463, 709-728

Gerday C., Gillis J.M. (1976). The possible role of parvalbumins in the control of contraction. *J. Physiol*. 258, 96

Giannini G., Clementi E., Ceci R., Marziali G., Sorrentino V. (1992). *Science* 257, 91-94

Gonzalez A., Rios E. (1993). Perchlorate enhances transmission in skeletal muscle excitation-contraction coupling. *J. Gen. Physiol.* 102, 373-421

Grynkiewicz G., Poenie M., Tsien R.Y. (1985). A new generation of Ca^{2+} indicators with greatly improved fluorescence properties. *J. Biol. Chem*. 260, 3440-3450

Hamming R.W. (1989). Digital Filters. Third edition. *Prentice Hall, Englewood Cliffs, CA*, 189pp

Harkins A.B., Kurebayashi N., Baylor S.M. (1993). Resting myoplasmic free calcium in frog skeletal muscle fibres estimated with fluo-3. *Biophys. J*. 65, 865-881

Hell S., Stelzer E.H.K. (1992). Fundamental improvement of resolution with a 4-Pi-confocal fluorescence microscope using two-photon excitation. *Opt. Commun*. 93, 277

Hille B., Campbell D. T. (1976). An Improved Vaseline Gap Voltage-clamp for Skeletal Muscle Fibres. *J. Gen. Physiol.* 67, 265-293

Hille B., (1992). Ionic channels of excitable membranes. *Sinauer Assocciates Inc.*

Hodgkin A. L., Huxley A. F. (1952a). Currents carried by sodium and potassium ions through the membrane of the giant axon of Loligo. *J. Physiol. 116, 449-472*

Hodgkin A. L., Huxley A. F. (1952b). The components of membrane conductance in the giant axon of Loligo. *J. Physiol. 116, 473-496*

Hodgkin A. L., Huxley A. F. (1952c). The dual effect of membrane potential on sodium conductance in the giant axon of Loligo. *J. Physiol. 116, 497-506*

Hodgkin A. L., Huxley A. F. (1952d). A Quantitative Description of Membrane Current and its Application to Conduction and Excitation in Nerve. *J. Physiol.* 117, 500-544

Holmes K.C., D. Popp, W. Gebhard, W. Kabsch (1990). Atomic model of the actin filament , *Nature* 347, 44-49

Inesi G. (1985). Mechainism of calcium transport. *Ann. Rev. Physiol*. 47, 573-601

Klein M. G., Cheng H., Santana L. F., Jiang Y.-H., Lederer W. J., Schneider M. F. (1996). Two mechanisms of quantized calcium release in skeletal muscle. *Nature* 379(1), 455-458

Klein M.G., Lacampagne A., Schneider M.F. (1997). Voltage dependence of the pattern and frequency of discrete Ca^{2+} release events after brief repriming in frog skeletal muscle. *Proc. Natl. Acad. Sci. U S A* 94(20), 11061-6

Kovacs L., Ríos E., Schneider M. F. (1979). Calcium Transients and Intramembrane Charge Movement in Skeletal Muscle Fibres. *Nature* 279, 391-396

Kovacs L., Ríos E., Schneider M. F. (1983). Measurement and Modification of Free Calcium Transients in Frog Skeletal Muscle Fibres by a Metallochromic Indicator Dye. *J. Physiol*. 343, 161-196

Kushmerick M.J., Podolsky R.J. (1969). Ionic mobility in muscle cells. *Science* 166, 1297

Lacampagne A., Klein M.G., Schneider M.F. (1998). Modulation of the frequency of spontaneous sarcoplasmic reticulum Ca^{2+} release events (Ca^{2+} sparks) by myoplasmic [Mg^{2+}] in frog skeletal muscle. *J. Gen. Physiol.* 111(2), 207-24

Lacampagne A., Ward C.W., Klein M.G., Schneider M.F. (1999). Time course of individual Ca^{2+} sparks in frog skeletal muscle recorded at high time resolution. *J. Gen. Physiol.* 113(2), 187-98

Lakowicz J.R. (1983). Principles of fluorescence spectroscopy. *Plenum Press, NY*

Lamb G.D. (2000). Excitation-contraction coupling in skeletal muscle: comparisons with cardiac muscle. *Clin. Exp. Pharmacol. Physiol.* 27(3), 216-24

Lipp P., Niggli E. (1996). Submicroscopic calcium signals as fundamental events of excitation--contraction coupling in guinea-pig cardiac myocytes. *J. Physiol.* 492, 31-8

Liu W., Pasek D.A., Meissner G. (1997). Modulation of Ca^{2+}-gated cardiac muscle Ca^{2+}-release channel (ryanodine receptor) by mono- and divalent ions. *Am. J. Physiol.* 274, C120-8

Matsuo H., Ueda M., Hanaoka M., Hirose T., Numa S.(1989). *Nature* 339, 439-445

Meissner G., Conner G.E., Fleischer S. (1973). Isolation of sarcoplasmic reticulum by zonal centrifugation and purification of Ca2+-pump and Ca-binding proteins. *Biochimica et Biophysica Acta*. 298, 246-269

Meissner, G. (1994). Ryanodine receptor/Ca^{2+} release channels and their regulation by endogenous effectors. *Annu. Rev. Physiol*. 56, 485-508

Mejia-Alvarez R., Kettlun C., Rios E., Stern M.D., Fill M. (1999). *J. Gen.Physiol*.113, 177

Melzer W., Ríos E., Schneider M. F. (1984). Time course of calcium release and removal in skeletal muscle fibers. *Biophys. J.* 45, 637-641

Melzer W., Ríos E., Schneider M. F. (1986a). The Removal of Myoplasmic Free Calcium Following Calcium Release in Frog Skeletal Muscle. *J. Physiol.* 372, 261-292

Melzer W., Schneider M. F., Simon B. J., Szücs G. (1986b). Intramembrane Charge Movement and Calcium Release in Frog Skeletal Muscle. *J. Physiol.* 373, 481-511

Melzer W., Ríos E., Schneider M. F., (1987). A General Procedure for Determining the Rate of Calcium Release in Frog Skeletal Muscle. *J. Physiol.* 373, 481-511

Mikami A., Imoto K., Tanabe T., Niidome T., Mori Y., Takeshima H., Narumiya S., Numa S. (1989). *Nature* 340, 230-233

Monck J.R., Oberhauser A.F., Keating T.J., Fernandez J.M. (1992). Thin-section ratiometric Ca^{2+} images obtained by optical sectioning of Fura-2 loaded mast cells. *J. Cell. Biol.* 116(3), 745-759

Nakai J., Imagawa T., Hakamata Y., Shigekawa M., Takeshima H., Numa S. (1990). *FEBBS Lett*. 271, 169-177

Nakai J., Ogura T., Protasi F., Franzini-Armstrong C., Allen P.D., Beam K.G. (1997). Functional inequality of the cardiac and skeletal ryanodine receptors. *PNAS* 94, 1019-1022

Nakamura K. (1993). Three-dimensional imaging characteristics of laser scan fluorescence microscopy: Two-photon excitation vs. single photon excitation. *Optik* 93, 39

Neher E., Sakmann B., (1976). Single-channel currents recorded from membrane of denervated frog muscle fibres. *Nature* 260, 779-802

Nelson M.T., Cheng. H., Rubart M., Santana L.F., Bonev A.D., Knot H.J., Lederer W.J. (1995). Relaxation of arterial smooth muscle by calcium sparks. *Science* 270, 633-637

Pechère J.F., Capony J.P., Demaille J. (1973). Evolutionary aspects of the structure of muscular parvalbumins. *Syst. Zool*. 22, 533-548

Pizarro G., Fitts R., Uribe I., Ríos E. (1989). The Voltage Sensor of Excitation-Contraction Coupling in Skeletal Muscle: Ion Dependence and Selectivity. *J. Gen. Physiol.* 94, 405-428

Pizarro G., Csernoch L., Uribe I., Rodríguez M., Ríos E. (1991). The relationship between Q? and Ca release from the sarcopplasmic reticulum in skeletal muscle. *J. Gen. Physiol*. 97, 913-947

Pizarro G., Csernoch L., Uribe L., Ríos E. (1992). Differential effects of tetracaine on two kinetic components of calcium release in frog skeletal muscle fibres. *J. Physiol*. 457, 525-538

Pizarro G., Shirokova N., Tsugorka A., Ríos E. (1997). Quantal calcium release operated by membrane voltage in frog skeletal muscle. *J. Physiol*. 501, 289-303

Potter J.D., Gergely J. (1975). The calcium and magnesium binding sites of troponin and their role in the regulation of adenosine triphosphatase. *J. Biol. Chem*. 250, 4628-4633

Radermacher M., Rao V., Grassucci R., Frank J., Timerman A.P., Fleischer S., Wagenknecht T. (1994). *J. Cell Biol.* 127, 411-423

Rayment I., W.R. Rypniewski, K. Schmidt-Bäse, R. Smith, D.R. Tomchick, M.M. Benning, D.A. Winkelmann, G. Wesenberg, H.M. Holden (1993). Three-dimensional structure of myosin subfragment-1: a molecular motor. *Science* 261, 50-57

Ríos E., Schneider M.F. (1981). Stoichiometry of the reactions of calcium with the metallochromic indicator dyes Antipyrylazo III and Arsenazo III. *Biophys. J.* 36, 607-621

Ríos E., Brum G. (1987). Involvement of dihydropyridine receptors in excitation-contraction coupling in skeletal muscle. *Nature* 325, 717-720

Ríos E., Pizarro G. (1988). Voltage sensors and calcium channels of excitation-contraction coupling. *News of Physiological Sciences*. 3, 223-227

Ríos E., Stern M.D., González A., Pizarro G., Shirokova N. (1999). Calcium Release Flux Underlying Ca^{2+} Sparks of Frog Skeletal Muscle. *J. Gen . Physiol*. 114, 31-48

Rüegg J. C., (1992). Calcium in Muscle Contraction. *Springer-Verlag*

Scarpa A., Brinley F.J., Dubyak G. (1978). Antipyrylazo III, a “middle range” Ca^{2+} metallochromic indicator. *Biochemistry* 17, 1378-1386

Schmidt R.F., Thews G. (1993). Physiologie des Menschen. *Springer-Verlag*

Schneider M.F., Chandler W.K. (1973). Voltage dependent charge movement in skeletal muscle: a possible step in excitation-contraction coupling. *Nature* 242, 143-150

Sharma M.R., Jeyakumar L.H., Fleischer S., Wagenknecht T. (2000). Three-dimensional Structure of Ryanodine Receptor Isoform Three in Two Conformational States as Visualized by Cryo-Electron Microscopy. *J. Biol. Chem.* 275(13), 9485-9491

Shirokov R., Levis R., Shirokova N., Rios E. (1992). Two classes of gating current from L-type Ca channels in guinea pig ventricular myocytes. *J.Gen. Physiol.* 99(6), 863-95

Shirokova N., Ríos E. (1996a). Activation of Ca^{2+} release by caffeine and voltage in frog skeletal muscle. *J. Physiol*. 493, 317-339

Shirokova N., García J., Pizarro G., Ríos E. (1996b). Ca^{2+} release from the sarcoplasmic reticulum compared in amphibian and mammalian skeletal muscle. *J. Gen. Physiol*. 107, 1-18

Shirokova N., Ríos E., (1997). Small event Ca^{2+} release: a probable percursor of Ca^{2+} sparks in frog skeletal muscle. *J. Physiol*. 502, 3-11

Shirokova N., Garcia J., Rios E. (1998). Local calcium release in mammalian skeletal muscle. *J. Physiol.* 512, 377-84

Simon B.J., Klein M.G., Schneider M.F. (1991). Calcium dependence of inactivation of calcium release from the sarcoplasmic reticulum in skeletal muscle fibers. *J. Gen. Physiol.* 97(3), 437-71

Sheppard C.J.R., Gu M. (1990). Image formation in two-photon fluorescence microscopy. *Optik* 86, 104

Smith P.D., Liesegang G.W., Berger R.L., Czerlinski G., Podolsky R.J. (1984). A stopped-flow investigation of calcium ion binding by ethylene glycol bis(ß-aminoethylether)-N,N´-tetraacetic acid. *Anal. Biochem*. 143, 188-195

Smith G. L., Miller D. J., (1985). Potentiometric measurements of stochiometric and apparent affinity constants on EGTA for protons and divalent ions including calcium. *Biochem. Biophys. Acta* 839, 287-299

Stern M.D., Pizarro G., Ríos E. (1997). Local control model of excitation-contraction coupling in skeletal muscle. *J. Gen. Physiol.* 110(4), 415-40

Suda N., Penner R. (1994). Membrane repolarization stops caffeine-induced Ca^{2+} release in skeletal muscle cells. *Proc. Natl. Acad. Sci. U S A* 91(12), 5725-9

Takeshima H., Nishimura S., Matsumoto T., Ishida H., Kangawa K., Minamino N., Tanabe T., Mikami A., Numa S., Beam K.G. (1990). *Nature* 344, 451-453

Tanabe T., Takeshima H., Mikami A., Flockerzi V., Takahashi H., Kangawa K., Kojima M., Matsuo H., Hirose T., Numa S. (1987). *Nature* 328, 313-318

Thomas M.V. (1982). Techniques in calcium research, *Academic Press, London*

Timerman, A. P., H. Onoue, H. B. Xin, S. Barg, J. Copello, G. Wiederrecht, and S. Fleischer (1996). Selective binding of FKBP12.6 by the cardiac ryanodine receptor. *J. Biol. Chem.* 271, 20385-20391

Tsugorka A., Ríos E., Blatter L.A. (1995). Imaging elementary events of calcium release in skeletal muscle cells. *Science* 269, 1723-1726

Uttenweiler D. (1997). Ca^{2+} turnover in skinned muscle fibres: a new quantitative approach based on fluorescence imaging and numerical simulation.
Dissertation, Universität Heidelberg

Uttenweiler D., Weber C., Fink R.H.A. (1998). Mathematical modeling and fluorescence imaging to study the Ca^{2+} turnover in skinned muscle fibers. *Biophys. J* 74(4),1640-53

Uttenweiler D., Fink R.H.A. (1999). Dynamic Fluorescence Imaging. *in Jähne et al., 1999. Computer Vision and Applications, Academic Press.*, 323-346

Vergara J., Bezanilla F., Salzberg B.M. (1978). Nile blue fluorescence signals from cut single muscle fibers under voltage or current clamp conditions.
J. Gen. Physiol. 72, 775-800

Vogel H. (1995). Gerthsen Physik. *Springer*

Ward C.W., Schneider M.F., Castillo D., Protasi F., Wang Y., Chen S.R., Allen P.D. (2000). Expression of ryanodine receptor RyR3 produces Ca^{2+} sparks in dyspedic myotubes. *J. Physiol.* 525, 91-103

Williams M.E., Feldman D.H., McCue A.F., Brenner R., Velicelebi G., Ellis S.B., Harpold M.M. (1992). *Neuron* 8, 71-84

Wilson T. (1990). Confocal Microscopy. *Academic Press.*

Xu L., Mann G., Meissner G. (1996). Regulation of cardiac Ca^{2+} release channel (ryanodine receptor) by Ca^{2+}, H^{+}, Mg^{2+}, and adenine nucleotides under normal and simulated ischemic conditions. *Circ. Res.* 79(6), 1100-9

Acknowledgments

I am grateful for all the new input and all the experience that I have gained during the miraculous, exciting and enlightening, but also frustrating and stressful course of this work. It is time to lift up the people that have helped and supported me - I thank you very much!

Dear Prof. R.H.A. Fink, I thank you for your support, encouragement, help and the great research opportunities you provided as a supervisor for this project. Dear Rainer, I thank you for your humanity and your trust in me.

Dear Prof. J. Bille, I thank you very much for your flexibility that made this project come to be and your support of my work as a co-supervisor. I also thank you for the new insights into biomedical research that the integration into your group has provided.

Dear Eduardo, I thank you for your trust, never ending support and patience. I thank you for giving me so many chances to progress.

Dear Dietmar, I thank you for your help, mental support and constant encouragement. In addition, I thank you for lightning up countless hours in the fluorescence room.

Dear Adom, I thank you for your openness, your teaching and your constant help at any time of day. Foremost, I thank you wholeheartedly for some of the most insightful discussions in my life.

Thanks to the good old 'FINKEN' (Thomas , Oliver, Uwe, Conny, Romy and Claudia) and to the new team (the M&M´s Martin, Martin and Martin, Erich, Uwe, Simon, Christoph, Fredericke, Ruth)! Dear colleagues, thank you for all your help and the nice atmosphere you created. I enjoyed my time with you very much.

Dear Gonzalo, Gonzalo, Natalia and Roman, I thank you for mostly keeping me out of the black parts of history and for your help and advice while I was with you.

Dear Mom and Dad, I thank you for your love and believing in me.

Dear Annette and Roland, I thank you for your support and encouragement.

Dear Manami, I thank you for your support and understanding while I was far away.

Dear Peter, I thank you for your inspirations and good will.

Dearest Britta, I thank you from the bottom of my heart for being my big 'B' in my life and for being there when I needed you.